Università degli Studi di Napoli FEDERICO II

PhD Thesis in
Novel Technologies in Materials, Sensors and Imaging

XXVI cycle
Coordinator: Pr. Luciano Lanotte

FABRICATION AND CHARACTERIZATION OF THE NEW GENERATION OF SERS SUBSTRATES BASED ON BLOCK-COPOLYMERS FOR BIOLOGICAL AND ENVIRONMENTAL APPLICATIONS

PhD candidate
Dochshanov Alden

Advisors: Pr. Antonio Sasso   -   Univ. Federico II of Naples
         Dr.ssa Giulia Rusciano   -   Univ. Federico II of Naples

April 24, 2014

Contents

List of Figures

List of Tables

Introduction

The complexity of structural organization of biological macromolecules at different hierarchical levels determine their physiological functions. The sequences starting from the individual building blocks in biopolymeric chain (primary structure) up to the quaternary structure constituted by two or more biopolymeric chains are giving rise to highly complex three-dimensional structures, that were optimized through evolution. For instance, proteins possessing very similar primary, secondary and tertiary structures such as the bacterial retinal proteins bacteriprhodopsin, sensory rhodopsin, or halorhodopsin, can exert very different functions due to the subtle structural differences in critical parts of the proteins. And conversely, the same elementary chemical reaction can be catalyzed by structurally different enzymes [Siebert 2008].

Over the several decades the increasing demand for noninvasive and nondestructive structure analysis tools to identify and investigate tissues and cells has provoked an essential progress in the development of Raman spectroscopic methods. Basing on the new solutions for experiments and data evaluation, Raman spectroscopy-based approaches are transformed into robust, reliable techniques to investigate the chemical composition of complex biosamples, and to discover their molecular make-up in health and disease. Moreover, starting from more than decade ago it has systematically been shown that the finger-print information of Raman microspectra can significantly add to comprehension of the biochemical background of various regular, induced or pathological changes in eukaryotic cells, which is a major prerequisite for progress in areas such as molecular medicine and nanobiotechnology [Kneipp 2006]

Therefore, as one can deduce, the most challenging task in the contemporary molecular biophysics is the elucidation of the structure-function relationship of biological macromolecules. With taking into account the considerable list of techniques used in structural biology, i.e. X-ray crystallography, NMR spectrosopy, and cryogenic electron microscopy, that are providing detailed structures of macromolecules and considered as classical instruments, one might think about the current and future contributions of vibrational (Raman) spectroscopy to this field. There is no doubt, that the details of three-dimensional structure of a biopolymer is important in terms of understanding of the functional mechanism as it is the prerequisite for realistic hypothesis development. Nevertheless, a comprehensive clearing up of reaction mechanism on a molecular level, as a matter of fact, is based on the structural information usually beyond the resolution of the methods listed above. Generally, biological processes take place upon involving a series of structurally different states, such that a complete understanding of the reaction mechanism is based on the knowledge of the initial and final states and of the intermediate species. The intermediate states identification and the elucidating of their molecular properties are only possible on the basis of techniques providing the structural data as a function of time.

In all above mentioned considerations, Raman spectroscopy (RS) supplies a variety of advantages:

1. Firstly, being chemically sensitive technique, RS can contribute to the elucidation of details in the molecular structures and intermolecular interactions that go far beyond

the resolution of even highly resolved crystal structures.

2. Secondly, RS is in principle not restricted by the size of the sample and thus can offer valuable information for small biomolecules in addition to complex biological systems.

3. Thirdly, vibrational spectroscopic methods are applicable regardless of the state of the biomolecule, they are applicable to study the biomolecules in solutions, in the solid and crystalline state, or in monolayers, i.e. the technique accounts for the conditions that are closely related to the physiological reaction environment of the molecular event.

4. And the last, the universal character of the technique makes possible to combine RS with various time-resolved approaches.

Thus, minute information related to the dynamics of biological systems is obtainable, down to the femtosecond time scale. Apart from all the advantages presented, low inherent quantum yield of the RS, has been successfully overcome with the discovery and development of Surface-enhanced Raman scattering (SERS). The magnitude of the Raman scattering signal can be greatly amplified when the scatterer is placed in the very close vicinity of the surface, which enables this phenomenon to be a highly sensitive analytical technique [Kneipp 1998].

Providing molecular information due to high specificity of vibrational spectra from the target analyte in aqueous solution is the most important advantage of SERS, which until now has not been possible by any other technique [Xie 2011]. The great sensitivity and rich structural information provided by SERS promotes its use in study the secondary structure of macromolecules such as proteins and nucleic acids.

Interaction between different biomolecules, or between biomolecules and drugs, is usually accompanied with molecular structural changes. Due to its temporal resolution enhancement SERS can be employed to study the mechanisms of such interactions by providing real-time structural information. Moreover, SERS has been widely applied to single-molecule detection of cellular proteins due to high affinity of noble metals for different protein molecules [Sujith 2009]. It is also worth to note that SERS-active NPs also have advantages over use of fluorescent tags for detecting or tracking biomolecules. Use of such fluorescent tags suffers from overlapping of fluorescence spectra, which are broader than SERS spectra, and non-uniform photobleaching rates, thus leading to several potential complications [Cao 2002]. Thus, as it can be concluded, SERS has become a useful spectroscopic method in detection and analysis of biomolecules.

There were a number of attempts to develop many new technological innovations including high sensitivity chemical and biological detection systems, labeling schemes for authentication and tracking purposes, and dual scanning-probe/spectroscopic techniques that simultaneously provide topographical and spectroscopic information about an underlying surface or nanostructure. However, progress has been hampered by the inability of researchers to fabricate substrates with the high sensitivity, tunability, robustness, and reproducibility necessary for truly practical and successful SERS-based systems. These limitations have been due in part to a relative lack of control over the nanoscale features of Raman substrates that are responsible for the enhancement. With the advent of nanotechnology, new approaches are being developed to overcome these issues and produce substrates with higher sensitivity, stability, and reproducibility [Banholzer 2008].

Guided by the current diversity of the SERS substrates synthesis, that is conventionally could be subdivided into the couple of families (i.e. bottom-up and top-down), one is supposed to find a compromise solution representing the unified advantages of both. The

simplicity of synthesis, robustness, high enhancement factor and long range spatial order of plasmonic nanostructures (PNs) are the fundamentals for the receipt to be developed. And only simultaneous presence of all of these factors could be regarded as the sufficient proof of substrate's applicability to the objects of our interest, namely: Red-Blood Cell (RBC) membrane and pyrene.

Since the earliest times the red cell has been in a focus of scientific and medical investigation. Furthermore, since the early observers Swammerdam and Leeuwenhoek saw discrete corpuscles in samples of blood using the first microscopes, there has been a significant scientific interest in the structure and function of red blood cells. The later discovery about the real shape of red cells which is a biconcave disc introduced a scientific puzzle which is still not completely resolved today, and identified the need for a detailed knowledge of the plasma membrane composition and structure, and its interaction with cytoskeleton.

The non-nucleated red cell is unique among human cell type in which the plasma membrane, its only structural component, accounts for all of its diverse antigenic, transport, and mechanical characteristics. And the current concept of the red cell membrane envisions it as a composite structure in which a membrane envelope composed of cholesterol and phospholipids is secured to an elastic network of skeletal proteins via transmembrane proteins.

Structural and functional characterization of the many constituents of the red cell membrane, in conjunction with biophysical and physiologic studies, has led to detailed description of the way in which the remarkable mechanical properties and other important characteristics of the red cells arise, and of the manner in which they fail in disease states. Current studies in this very active and exciting field are continuing to produce new and unexpected revelations on the function of the red cell membrane and thus of the cell in health and disease, and shed new light on membrane function in other diverse cell types [Mohandas 2008]. Thus, all current and future studies related to the red blood cell still have a lot of enigmas to decrypt.

The second object of interest of the work is Polycyclic Aromatic Hydrocarbons (PAH), namely pyrene. The approach used to detect the presence of the pyrene in water solution is of great practical significance because of the environmental pollutant nature of PAH formed during the incomplete burning of coal, oil, and gas or other organic substances such as tobacco or carbroiled meat [Leyton 2004]. Furthermore, these compounds can be found as a mixture of different related molecular components in air, soil, and water due to both natural process and human activity. Because many of them have been reported to be strong carcinogens [Guo 2004] it is very important to find an effective and selective method to detect them. The main challenge in detection of the PAH by means of SERS is their electronic structure. Although coupling of π-electrons of PAH with the metal substrate should occur, this class of compounds does not present a specific functional group that could act as a strong anchor to the surface of the substrate that would intensify the SERS effect via a significant chemical mechanism. Moreover, in the presence of the substrates traditionally used in SERS analysis, the PAHs were observed to decompose [Costa 2006]. Despite of these natural constraints the approach used here is supposed to be based on three fundamental factors: physisorption, high enhancement factor, short signal exposition (integration) time and moderate laser power.

Thus, the novelty of the experimental work performed here includes the following:

- the SERS substrates obtained, represent a compromise between high enhancement factor ($\approx 10^6$), excellent spatial reproducibility of the SERS signal (with standard deviation around $\pm 5\%$ over a colossal scale (10×10 mm)) and ordered morphology represented as an ultra-high density array of silver nanoclusters of uniform size and

gap distance;

- for the first time (according to the current state in literature and to the best of our knowledge) the hyperspectral imaging of the single red blood cell membrane was performed;

- the detection of the minute concentrations of pyrene was obtained basing exclusively on the combination of physisorption and optimized experimental parameters of the measurement (power of the laser and integration time).

The authenticity of the work results is based on the thorough examination of the synthesized SERS substrates by means of different but closely inter-related experimental techniques, such as: dynamic light scattering (DLS), small-angle X-ray spectroscopy (SAXS), atomic force microscopy (AFM), UV-Vis spectroscopy, transmission electron microscopy (TEM), and SERS. Thereby, each technique involved into characterization, both separately and in connection with others contributed to the elucidation of the quality level of substrates. Therefore, the factors essential for synthesized substrates' applicability, such as spatial uniformity (assuming the reproducibility of signal), sensitivity (high enhancement factor) were ascertained.

Thus, the main objective of this work can be formulated as follows: to demonstrate the applicability of the surface-enhanced Raman spectroscopy in revealing of the chemical content of the red blood cell membrane, and to detect the minute concentrations of pyrene.

According to the objective stated, the work has been organized in the following way:

- first, a detailed overview of the state-of-the-art in the field of Surface-Enhaced Raman Spectroscopy (SERS) and, in particular, SERS-substrates synthesis;

- development of the optimal SERS-substrate production protocol;

- SERS substrates synthesis;

- SERS substrates characterization and further optimization in line with our application;

- application of the substrates: hyper-spectral imaging of the Red Blood Cell membrane (RBC membrane), Polycyclic Aromatic Hydrocarbon compound (pyrene) detection.

Structurally the thesis is composed of 5 Chapters:

Chapter 3 introduces the brief theoretical description of Raman scattering, in particular supplying also the additional information related to the Raman cross-section and Raman scattering intensity. After the example of Raman spectra with peaks assignment of biological tissues supports an idea of the structural and spectral complexity of the ones. Finally, the introduction to surface enhanced Raman spectroscopy is given, underlining the plasmonic origin of the phenomena and providing the explanation of electromagnetic and chemical enhancement mechanisms of SERS. At the end a short look onto the advantages of SERS application in cells studies can be found.

Chapter 4 supplies the brief overview of the SERS substrates synthesis, focusing on both advantages and drawbacks. The principle differences between "top-down" and "bottom-up" are outlined. The conclusion on the "ideal" SERS substrate is presented, which in short, can be reduced to the compromise between two major factors: reproducibility and high-enhancement factor. Thus, satisfying the "SERS uncertainty principle". At the end, results that the block-copolymer based self-assembled nanostructured substrates meet all expectations posed previously, therefore satisfying the complex of our needs regarding the

SERS substrate, being a perfect combination of the long-order spatial uniformity and high enhancement factors provided.

Chapter 5 contains the information related to the materials used and selected recipe of SERS substrate synthesis (including its optimization) with subsequent description of the testing techniques involved, providing both theoretical(general) and experimental details. After the illustration of the experimental results is given. At the end the conclusion on the quality and applicability of substrates is presented. The crucial criteria responsible for the reliable results upon application are underlined.

In chapter 6 the application results of the SERS substrates synthesized are supplied. The hyperspectral imaging of the single red blood cell is reliably provided. The comparison of the spectral information obtained by means of SERS-technique with respect to the ordinary Raman imaging if the red blood cell is done. The conclusion on the essential prevalence of the spectral information provided by SERS spectroscopy upon the confrontation with the Raman is given.

The results on the minute concentration of the pyrene are represented. As a result the deduction on the SERS-substrates applicability to pyrene detection, even despite of their extreme structural sensitivity to catalytically active surfaces (silver nanoclusters), is provided.

Finally, Chapter 6 provides the prospects of future developments of the results presented.

Chapter 7 contains the general conclusion in a form the synthesis of all the results obtained in their relation with the general aim (aforementioned as the main objective of the work) and the intermediate tasks (aforementioned as the points of the work organization) posed.

At the end the list of the references used is given.

Theoretical Background

2.1 Theoretical overview of Raman Scattering

The polarization induced in a molecule by an oscillating electric field describes the classical description of Raman scattering depicted in Figure 2.1. Depending on the quality of interaction (with or without exchanging energy with vibrations in the molecule) the induced dipole then radiates scattered light. The strength of the polarization induced, P, linearly depends on the polarizability, α, and the incident electric field, $\mathbf{E}$:

$$\mathbf{P} = \alpha\mathbf{E} \tag{2.1}$$
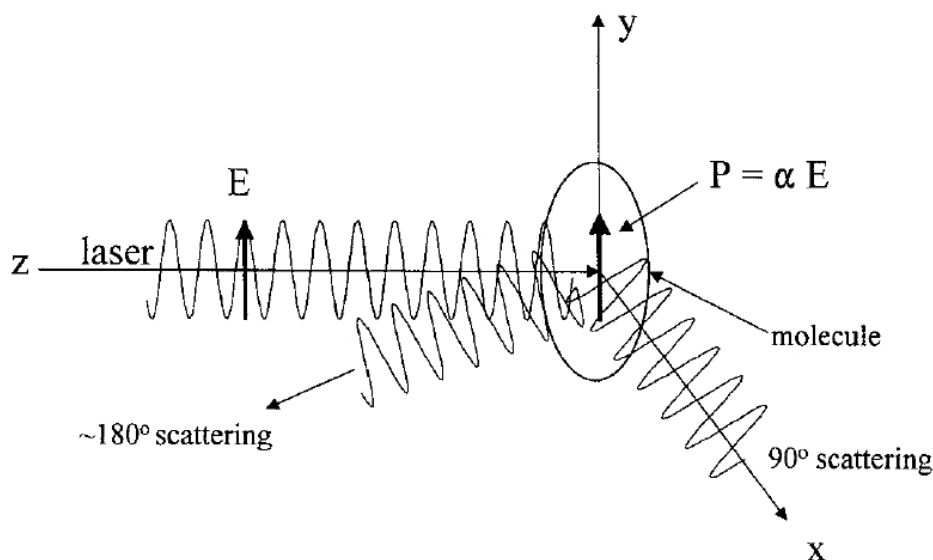
Figure 2.1: Polarization (P) induced in a molecule's electron cloud by an incident optical electric field E. Scattering may be in various directions, but 90° and 180° are shown.

Equation 2.1 is the base for both classical and quantum mechanical treatments of Raman scattering. Note, that such treatments are very valuable and demonstrative in understanding the effect and interpreting spectra. A classical treatment of the Raman scattering is based on molecular vibrations and the polarizability, α, Eq. 2.1. Consider the incident optical electric field to be governed by:

$$\mathbf{E} = \mathbf{E}_0 \cos 2\pi\nu_0 t \tag{2.2}$$

where ν_0 is the frequency of the laser light. The molecular vibrations are usually considered to be composed of normal modes, $\mathbf{Q}_j$, of which there are 3N-6 (or 3N-5 for a linear molecule)

in a molecule with $\mathbf{N}$ atoms:

$$\mathbf{Q}_j = \mathbf{Q}_j^\circ \cos 2\pi\nu_j t \tag{2.3}$$

where ν_j is the characteristic harmonic frequency of the jth normal mode. The polarizability of electrons is modulated by the molecular vibration, so that

$$\alpha = \alpha_0 + \left(\frac{\partial\alpha}{\partial Q_j}\right) Q_j + \ldots \tag{2.4}$$

Therefore, the polarization is obtained by inserting Eq. 2.3 and Eq. 2.4 into Eq. 2.1:

$$P = \alpha_0 E_0 \cos 2\pi\nu_0 t + E_0 Q_j^\circ \left(\frac{\delta\alpha}{\delta Q_j}\right) \frac{\cos 2\pi\left(\nu_0 + \nu_j\right) + \cos 2\pi\left(\nu_0 - \nu_j\right)}{2} \tag{2.5}$$

After assuming (classically) that the polarized electrons will radiate light at the frequency of their oscillations, Eq.2.5 demonstrates that light will be scattered at three frequencies. The first term is Rayleigh scattering, which is at the same frequency as the incoming light, and has a magnitude proportional to the inherent polarizability of the molecule. The second term is anti-Stokes Raman scattering, which occurs at $\nu_0 + \nu_j$, and the third term is Stokes Raman scattering at $\nu_0 - \nu_j$ (See Figure 2.2). Also it should be noted that ν_j is the same frequency that would be observed with infrared (IR) absorption for a given vibrational mode, if allowed by symmetry of molecule.
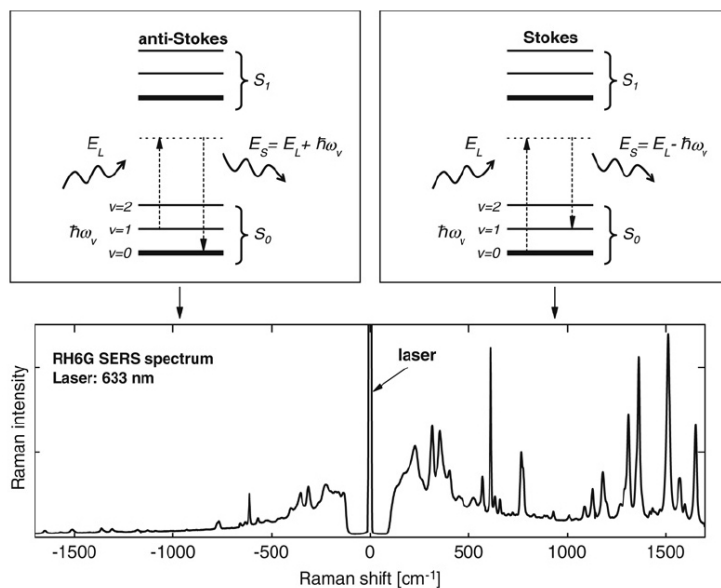
Figure 2.2: Simplified Jablonsky diagrams of the anti-Stokes (top-left) and Stokes (top-right) Raman processes. [Ru 2008]

Although Eq. 2.5 was derived classically and is incomplete it does provide some useful insights.

First, polarization and scattering (both Rayleigh and Raman) intensities are linear with the laser intensity. Nonlinear Raman scattering can occur at high values of E_0 but is generally not an issue in analytical applications.

Second, *only vibrations that change the polarizability* (and consequently $\delta\alpha/\delta Q \neq 0$) *yield Raman scattering* see Figure 2.3. The last statement is the basis of the primary

selection rule for Raman scattering and its effect is quite evident in the spectra of Figure 2.4. The polarizability of the C=C bond changes significantly with a vibration associated with the stretch of the C=C bond.
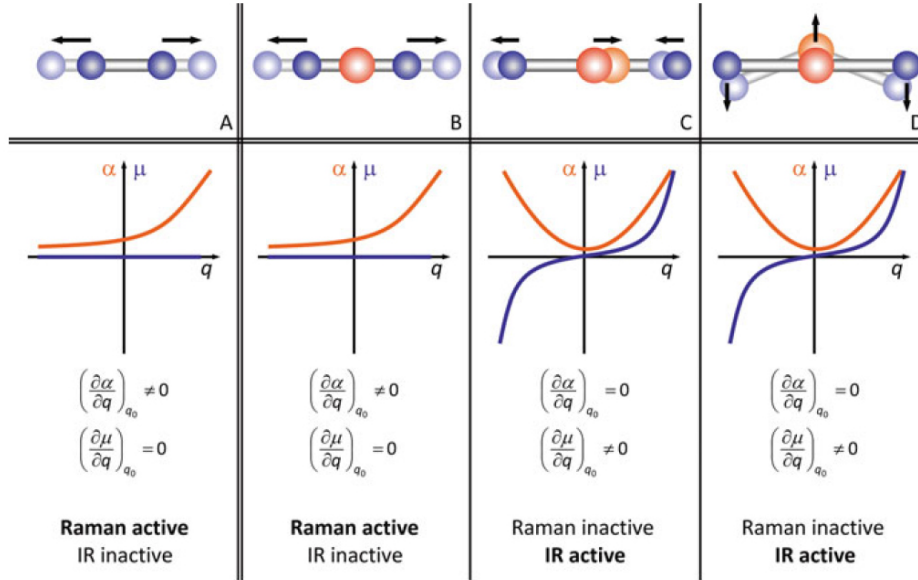
Figure 2.3: The derivatives of polarizability (red) and dipole moment (blue) are schematically depicted for the normal modes of a two (a) and a three atomic molecule (b-d). Based on these intuitive considerations, conclusions on the IR and Raman activity of the modes can be drawn.

On the contrary, the Raman scattering from a C=C bond is strong, while that of a C=O bond is relatively weak.

A third consequence of Eq. 2.5 is that Raman shifts may be both positive and negative. Since anti-Stokes Raman intensity depends on the population of the first vibrationally excited state, its intensity related to temperature by the Boltzmann distribution, given by Eq. 2.6 for the case of a nondegenerate vibration:

$$\frac{I_R(\nu_0 + \nu_j)}{I_R(\nu_0 - \nu_j)} = \frac{(\nu_0 + \nu_j)^4}{(\nu_0 - \nu_j)^4} exp\left(\frac{-h\nu_j}{kT}\right) \qquad (2.6)$$

Fourth, $\delta\alpha/\delta Q_j$, may vary essentially for different molecules and for different modes, in a given molecule, leading to wide variations in Raman scattering intensity. Fifth, although it is not apparent from 2.5, $\delta\alpha/\delta Q_j$ is generally much smaller that α_0, and Raman scattering is much weaker than Rayleigh scattering (about 10^6 Rayleigh photons correspond to only one Raman photon). The observed intensity of Raman scattering is proportional to the cross section, σ_j, with units of square centimeters per molecule. The magnitude of σ_j, is related to $\delta\alpha/\delta Q_j$. One consequence is the following Raman intensity I_R dependence on the frequency:

$$I_R = \mu(\nu_o \pm \nu_j)^4 \alpha_j^2 Q_j^2 \qquad (2.7)$$

where μ is a constant. Although Raman intensity is conventionally expressed in watts, in modern Raman spectroscopy it is usually measured in photons/second. Equation 2.7
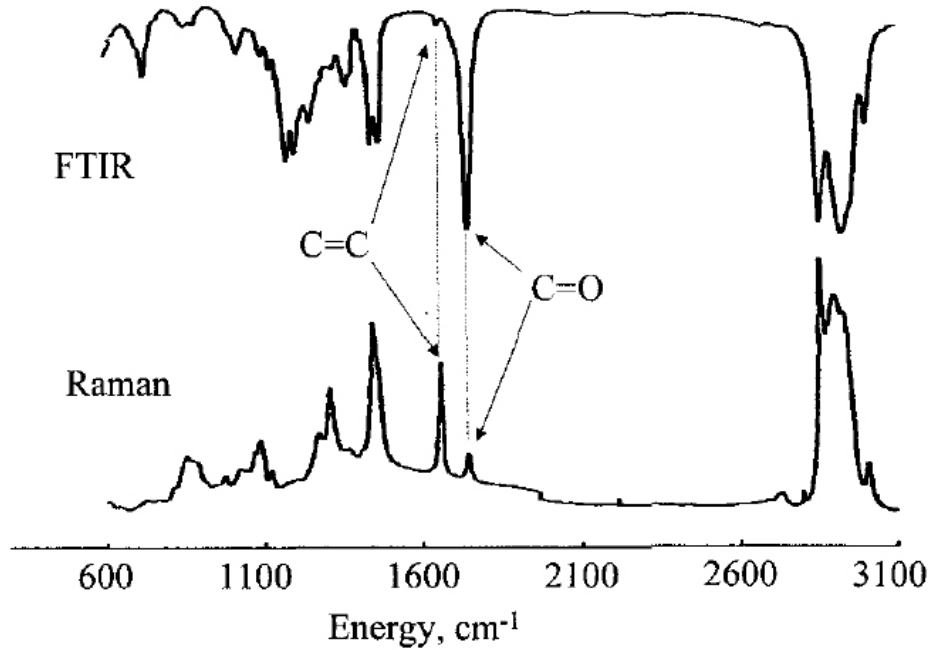
Figure 2.4: FTIR (upper) transmission and Raman scattering (lower) of oleic acid methyl ester.

indicates that Raman intensity varies with the fourth power of the observed frequency for normal Raman scattering, which, in turn, depends on laser frequency. The ν^4 (or equivalently $\frac{1}{\lambda^4}$)factor is derived from the classical treatment of scattering from an oscillating induced dipole, with the intensity expressed in watts. The expression of frequency in terms of wavenumbers (in reciprocal centimeters) is conventional with respect to hertz, using the symbol $\bar{\nu}(\bar{\nu} = \nu/c = \lambda^{-1}$ with c the speed of light and λ the wavelength. Accordingly, Eq. 2.7, becomes Eq. 2.8, with the factor of c^4 contained in the constant μ':

$$I_R = \mu'(\bar{\nu}_o \pm \bar{\nu}_j)^4 \alpha_j^2 Q_j^2 \tag{2.8}$$

The Raman shift $\bar{\nu}_j$ (in reciprocal centimeters) is sometimes labeled $\delta\bar{\nu}_j$ in the literature, while the scattered light occurs at an absolute frequency $\bar{\nu}_o \pm \bar{\nu}_j$.

2.1.1   Definition and magnitude of Raman cross-section

The number of factors, such as polarizability, laser wavelength, and empirical cross section for a given Raman band σ_j in each particular geometry pre-determine the Raman intensity observed, and this is adequate for signal strength estimating. Parameter σ_j *is proportional to the probability of an incident photon being scattered as a Raman-shifted photon with a particular Raman shift.* For a classical treatment, Eq. 2.9 relates the Raman scattering (in watts) to the cross section, with laser intensity (I_0) in watts:

$$I_R = I_0 \sigma_j D dz \tag{2.9}$$

where D is the number density of scatters (molecules per cubic centimeter) and dz is the path length of the laser in the sample (or the spectrometer depth of field). In this case, σ_j would

track $\bar{\nu}_j^4$, as stated in Eq. 2.8. The frequency dependence depicted in Eq.2.8 is sometimes used to determine a cross section that is independent of frequency [Schrötter 1979]. For a scatterer that is not resonant or preresonant, and follows the classical $\bar{\nu}^4$ dependence, a frequency independent cross section σ_j° may be defined by Eq. 2.10:

$$\sigma_j^\circ = \frac{\sigma_j}{(\bar{\nu}_0 - \bar{\nu}_j)^4} \tag{2.10}$$

where σ_j° has the units of centimeters to the sixth power per molecule when $\bar{\nu}_0$ and $\bar{\nu}_j$ are expressed in wavenumbers (in reciprocal centimeters). Note that ν_j is the vibrational frequency of the Raman mode, and $\bar{\nu}_0 - \bar{\nu}_j$ is the absolute frequency of the scattered light.

Upon the introduction of photon counting detectors into Raman instrumentation a complication to the frequency dependence of σ_j arose. Virtually all modern spectrometedsrkflrs are rather photon-counters than watts measures, and the two differ by a factor of $h\nu$. Numerical considerations based on photons/second and photon counting are more consistent with a quantum mechanical treatment where a cross section is effectively a statement of probability, meanwhile the classical treatment is based on induced dipoles. If Eq. 2.9 is rewritten for counting systems, Eq. 2.11 results:

$$P_R = P_0 \sigma_j' D dz \tag{2.11}$$

Now, P_0 and P_R have units of photons per second, and σ_j' has a different frequency dependence than that of 2.10. Substituting σ_j from 2.10 into 2.9 and taking into account that $I_R = P_R hc(\bar{\nu}_0 - \bar{\nu}_j)$ and $I_0 = P_0 hc\bar{\nu}_0$, one can derive:

$$\sigma_j' = \sigma_j^\circ \bar{\nu}_0 (\bar{\nu}_0 - \bar{\nu}_j)^3 \tag{2.12}$$

Introducing P_R parameter as the measure of photons per second and taking into account that σ_j is the integrated cross section for Raman scattering in two respects: over all directions from the sample, and over the wavelength range of an entire Raman band. But in practice, only a relatively small range of solid angle is observed, in one of several scattering directions from the sample. Thus, it is more useful to define the differential Raman cross section, $d\sigma_j/d\Omega$, where Ω represents the solid angle of collection. The symbol β will be used for this differential cross section, as in Eq. 2.13:

$$\beta(\text{cm}^2\text{molecule}^{-1}\text{sr}^{-1}) = \frac{d\sigma_j}{d\Omega} \tag{2.13}$$

The symbol β is used here rather than the more common $d\sigma_j/d\Omega$ to explicitly distinguish β from the integrated σ_j and from the cross section differentiated both with respect to observation angle and with respect to wavelength(β'). β° is analogous to σ_j° and denotes the differential cross section with units of centimeters to the sixth power per molecule per steradian.

It should be taken into account, that σ_j is also integrated over the Raman bandwidth, as is β. However, the usual representation of a spectrum is scattering signal vs. Raman shift, $\bar{\nu}_j$, and the signal depends of β at a particular Raman shift. β' will be defined to account for this fact (see also Figure 2.5), with:

$$\beta'(\text{cm}^2\text{molecule}^{-1}\text{sr}^{-1}\text{wavenumber}^{-1}) = \frac{\delta\sigma_j}{\delta\Omega\delta(\Delta\bar{\nu})} \tag{2.14}$$

Note, that β' depends both on observation direction and on Raman shift.

The generally accepted way for the Raman cross sections determination is the quantitative comparing the Raman signal for an unknown to that for a standard with known cross
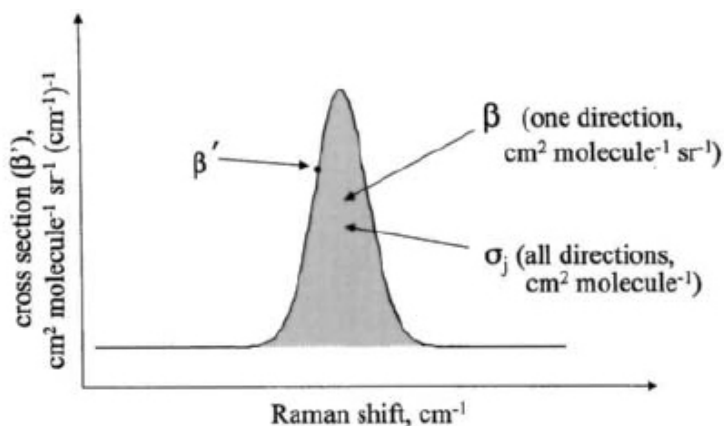
Figure 2.5: Definitions of β, β', and σ_R for to a generic Raman band. β' is the cross section at a particular Raman shift and direction; β is integrated over the bandwidth, and σ_j is integrated over both bandwidth and direction.

section. As to the standard cross sections, they were determined by comparison to some radiometric standard, with painstaking attention to collection variables and geometry. The general procedure for the Raman cross section is based on comparison of Raman intensity of an "unknown" to that from one of the standards. The ratio of the peak areas of two bands adjusted for relative number density will equal the ratio of cross sections, provided the measurement conditions are the same and the spectrometer response function is known. Despite the similarity of experimental conditions, cross sections from different labs often show significant (30 to 50 %) variations. Compared to competing processes of absorption and fluorescence, Raman cross sections are nearly always very small. *Normal Raman scattering cross sections are often 6 to 8 orders of magnitude smaller than fluorescence cross sections, leading to the common problem of fluorescence interference.* Thus, many aspects of experimental design are caused by the need to reduce fluorescence.

When the incidence light approaches an electronic absorption of the same molecule, the resonance effects appears providing the great increase of the cross section also. Preresonant scattering takes place when the laser wavelength approaches an absorption maximum but is not yet within the absorption band. A pragmatic definition of preresonant scattering is when the cross section begins to deviate from the ν^4 dependence expected for normal scattering [Asher 1985], [Schrötter 1979]. However, the boundaries between normal, pre-resonant, and resonance Raman are often blurred. The importance of resonance effect in analytical applications is the large β they generate, moreover, in some cases, resonance effects can be used to selectively observe a particular scatterer in a complex matrix.

2.1.2 Raman scattering intensity

Considering the expressions of Raman intensity and taking into account that it is often convenient to express the incident laser light in terms of power density (P_D, photons per square centimeter per second) rather than power (photons per second), in which case P_R is generated by a beam with a 1 cm^2 cross section and a path length of dz, 2.11 may be restarted in terms of β:

$$P_R(\text{photons sr}^{-1} \text{ cm}^{-2} \text{ sec}^{-1}) = P_D \beta D dz \qquad (2.15)$$

Should be noted that for a 1 cm^2 beam, Ddz equals the total number of illuminated molecules. There are many experiments where the total beam area cannot be observed, in which case P_R is more usually stated as specific intensity, L:

$$L(\text{photons sr}^{-1} \text{ cm}^{-2} \text{ sec}^{-1}) = P_D K \qquad (2.16)$$

If one considers a sample area that is evenly illuminated by some power density P_D, then L is the number of Raman photons scattered from 1 cm^2 of the sample, into 1 steradian of solid angle in 1 second; K is used to denote a geometric factor that depends on observations geometry. Its significance is illustrated in Figure 2.6:
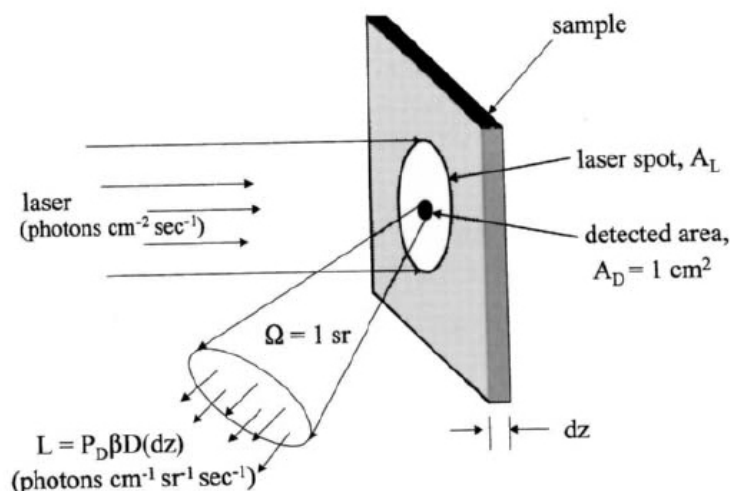
Figure 2.6: Schematic representation of the specific intensity, L, where L is the photon/sec scattered by a 1 cm^2 area (A_D) into a 1 steradian solid angle (Ω), assuming constant power density over the illuminated area.

For the case of 180° backscattering geometry with a thin sample, K is the sample depth observed by the spectrometer, in centimeters. Figure 2.6 demonstrates the specific intensity for a large beam impinging on a sample and Raman observation at 180°; where A_D and Ω_D are the sampled area and collection angle correspondingly.

The sample (β,D) and laser (P_D) variables are the main prerequisites that predetermine the specific intensity as an important quantity, but not spectrometer parameters such as collection angle, quantum efficiently, etc. Meanwhile L indicates "what the spectrometer has to work with" while collecting and detecting scattered light.

Obviously, β and D are characteristics of the sample and are not variable by the analyst. The laser power in its turn density can be increased, however, to a limit achievable by the available laser or by sample radiation damage. Provided the longer path length can be observed by the spectrometer a longer path length through the sample can increase scattering. The main point here is the limitations imposed in the Raman signal by the product $P_D \beta_D$. Ultimately, the upper limit on Raman signal, even for a 100 % efficient spectrometer, is governed by variables of the sample (β and D) and the maximum value of P_D allowed by sample damage.

Finally, it should be noted that even very weak scattering, such as that from a single molecular layer of benzene, generates about 10^6 photons cm^{-2}sr^{-1}sec^{-1}. Modern instru-

mentation permitting single photon counting, provides the acquisition of the signals much smaller than 10^6, even of only a fraction 0.1 % of the available specific intensity is collected and detected. For nowadays Raman measurements the size of the signal is a rare limitation, but noise and background are the main issues to consider for the strength of the signal. In the absence of background and noise, observation of very low light levels is straightforward with modern equipment. Success in acquiring Raman spectra is often more dependent on reducing noise (from the detector, laser, etc.) and background (from fluorescence, stray light, solvent, etc.) than it is on generating sufficient signal.

2.2 Biological application of Raman spectroscopy: keratins (wool, stratum corneum).

Raman studies of biomolecular polymers when compared to other spectroscopic methods have demonstrated a number of advantages including minimal or no damage of the sample and ease of sampling arrangements. Apart of the mentioned, such an important feature as spectral sensitivity to a range of parameters affecting biomolecular structures becomes an additional significant advantage for studies of environmental change, in particular, the consequences of pH changes on tissue degradation, temperature, degree of hydration, or bacterial or drug attack.

If the proteins are considered, first, it has to be underlined that Raman spectroscopy is not applicable in establishing the sequence of the amino acids of the *primary structure*, but it is useful in detection of certain types of amino acids, for example, the aromatic amino acids tyrosine, tryptophan, phenylalanine, and histidine.

In case of the secondary structure of a protein, which is characterized by the spatial arrangement of the amino acids in polypeptide chains of the protein, Raman spectroscopy is of use, permitting to reveal the type of secondary structures present within a protein, the geometry of certain bonds, and the environment of some side chains.

The peptide group (-CONH-) is the most characteristic functionality bond within a protein. The one is considered to be near planar, and this is attributed to bond resonance stabilization. The vibrations of the atoms give rise to a number of distinctive vibrational features, namely, the amide I, II, III, IV, V, VI, VII, A and B bands. Because of different selectron rules, the amide I, II, III, A and B are observed in the infrared spectra of proteins, whereas only the amide I, III, A and B bands are detectable by Raman spectroscopy. The vibrational modes of these bands are represented in Figure 2.7.
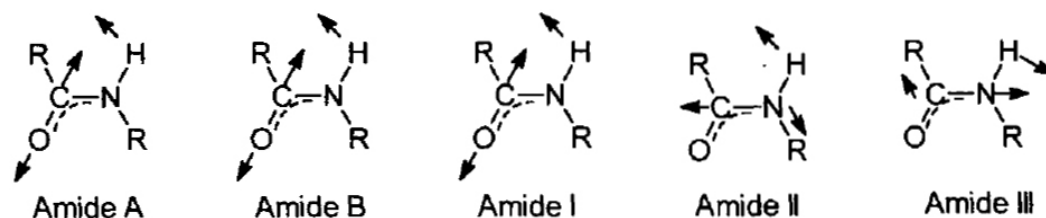
Figure 2.7: Vibrational modes of the peptide bond.

C=O stretching vibration of the peptide group with a small contribution from N-H in-plane bending is the origin of the amide I band. Meanwhile, the amide III band arises from a combined N-H bending and C-N stretching of the peptide group. Both the amide A

and B bands originate from Fermi resonance (a result of the interaction of the first excited state of the N-H stretching vibration and the overtone of the amide II vibration). The amide I, II and III bands are conformationally sensitive and are useful in identification of the secondary structure type present in a protein (See Table 2.1).

Vibrations arising from amino acids can be classified into two groups: originating from the CH_2/CH_3 groups of amino acids and the vibrations originating from the aromatic rings in phenylalanine, tyrosine, and tryptophan. The C-H vibrations of amino acids are observed in both IR (weak) and Raman spectra (strong).

Finally, cystine, being a very important amino acid, in which oxidation of the thiol groups results in disulphide bond formation, that ultimately leads to stabilization of the protein structure. The bond is homonuclear and is therefore Raman active and IR inactive. The disulphide bonds form crosslinks between adjacent protein chains or different part of the same protein. The frequency of the vibration is dependent upon the arrangement of the atoms, $-C_\alpha-C_\beta-S-S-C_{\beta'}-C_{\alpha'}-$, involved in these crosslinkages [Gremlich 2000].

Below the couple of biological Raman spectroscopy application examples will be given. Thus, direct interrelation between the sophisticated morphological structure and the complex Raman spectral information will be underlined. This concept is of crucial importance that will be discussed in the experimental part of the thesis.
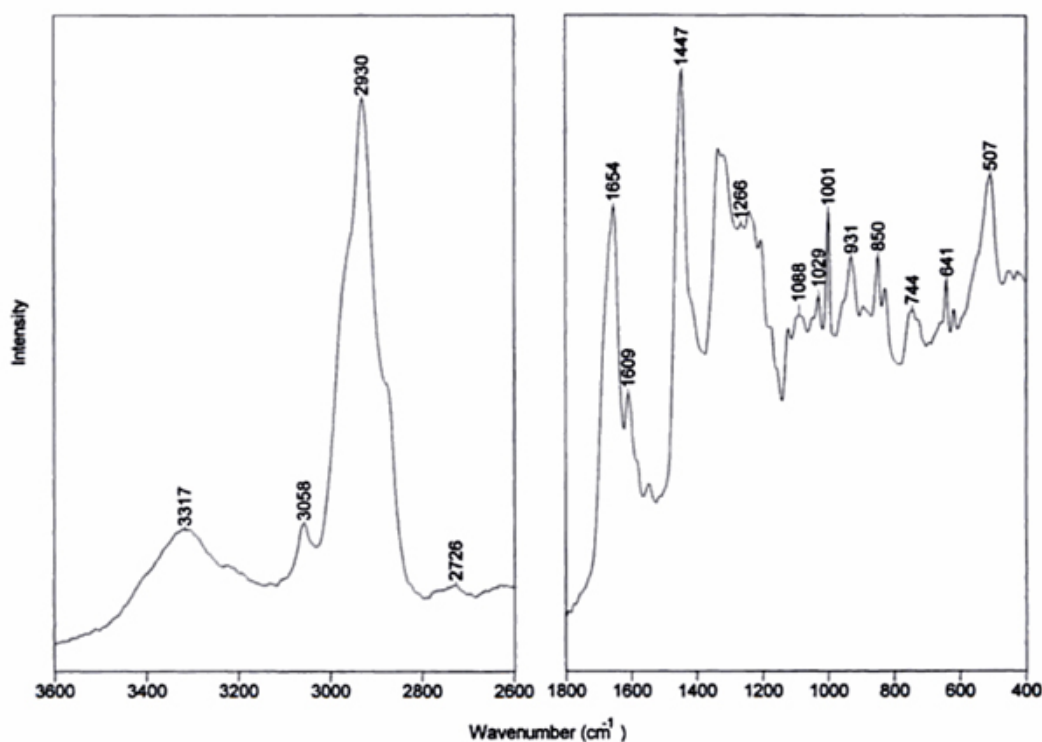
Figure 2.8: Raman spectrum of wool.

The first example is the *wool*. As it can be seen from see Figure 2.8 and Table 2.2, the predominant secondary structure present in the wool is the α-helix; however, there are a number of other protein conformations present, including the random coil, or amorphous form, and the β-pleated sheet. The position of the certain bands, such as amide bands, are characteristic of these various secondary structures, which are summarized in Table 2.1.

	α-Helix	β-Pleated sheet	Random coil
Amide I	1660-1645	1680-1665	1670-1660
Amide III	1310-1260	1240-1225	1260-1240
Skeletal C-C	950-885	1010-1000	960-950

Table 2.1: Characteristic Vibrations of Secondary Structures.

The positions of the amide I amide band, at 1654 cm^{-1}, and the C-C stretching vibration of the skeletal backbone, at 931 cm^{-1}, are indicative of an α-helical conformation. In accordance with characteristic literature values, the position of an amide III band of an α-helix would be expected within the region of 1310-1260 cm^{-1}. A number of weak features can be observed in the amide III region, and the feature at 1266 cm^{-1} is assigned to the α-helix structure.

The amide I vibration is a very complex region for most proteins, for a number of reasons. The functional groups of the aromatic amino acids phenylalanine, tyrosine, and tryptophan are observed within this region. The broadness and general asymmetry of the band can be attributed to the presence of a number of secondary structures within the protein. For instance, within one type of secondary structure the dihedral angles of the peptide backbone chain vary over a wide range, and this leads to band broadening. The secondary structures also have similar frequencies, which overlap - again resulting in band broadening.

The second example of Raman spectroscopy application to biological tissues provided here is the *skin*. Raman spectroscopy was first used to characterize human stratum corneum in 1992 [Barry 1992]. The barrier nature of the stratum corneum is derived from the unique morphology of its constituents, which are typically 75-80 % protein, 5-15 % lipids, and 5-10 % unidentified material on a dry weight basis; see Figure 2.9:
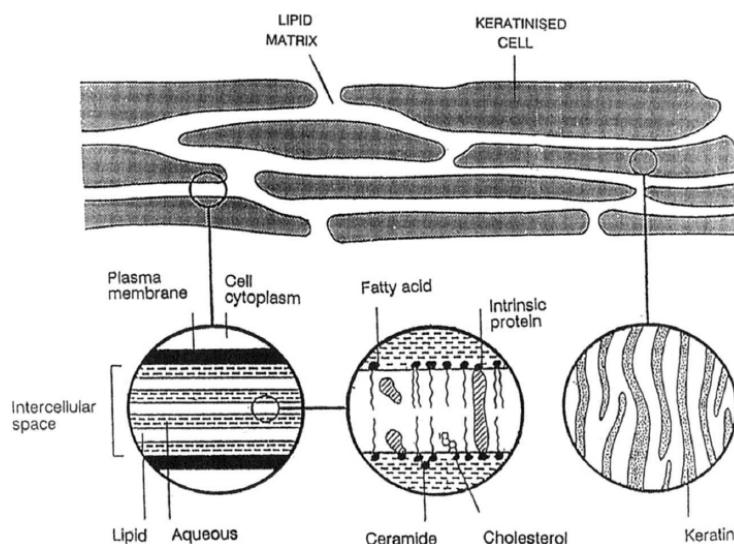
Figure 2.9: "Bricks and mortar" diagram of the human stratum corneum (thickness 6-30 μm) showing lipid matrix and keratinized cell construction ([Edwards 1995]).

The predominant secondary structure of the corneocytes protein fraction is that of an α-helix (approx. 70 %), with some β-keratin (approx. 10 %) and cell wall envelopes (approx.

5 %) [Elias 1983]. The high percentage of α-helical content is reflected in the position of the conformationally sensitive amide and C-C skeletal backbone vibrations in the Raman spectrum of human stratum corneum; see. Figure 2.10
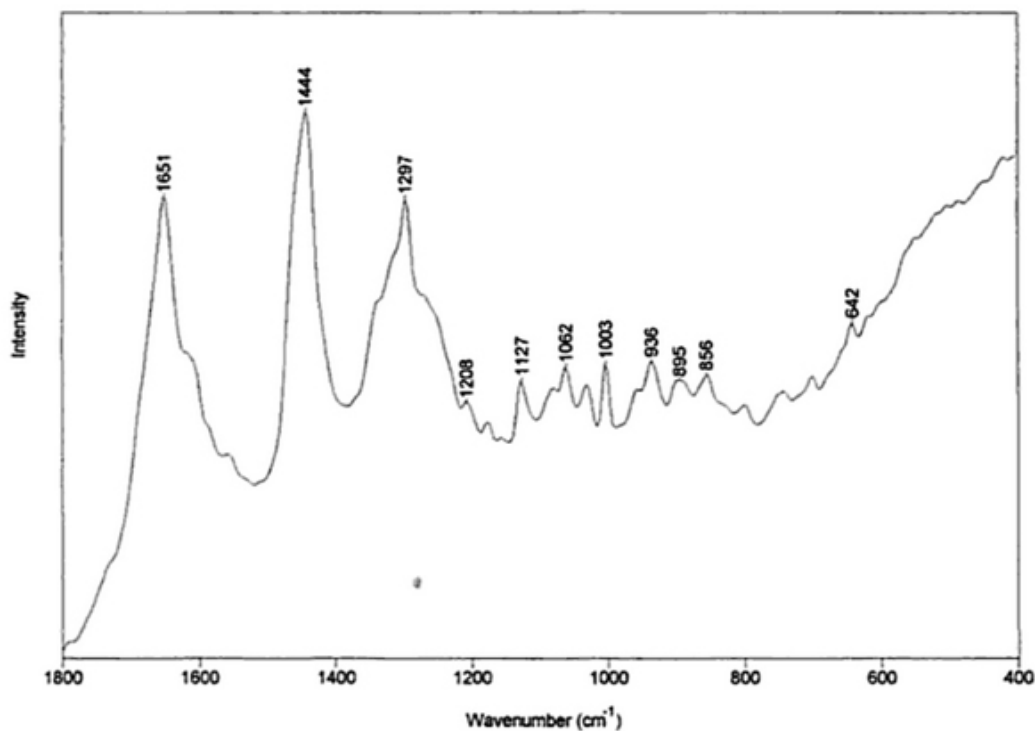
Figure 2.10: Raman spectrum of human stratum corneum.

A table of assignments for a couple of keratin proteins discussed, is given below Table 2.2, [Gremlich 2000]:

Thus, on the examples provided here, both the complexity of the morphological structure and, as a logical consequence, the richness of the Raman spectral information were demonstrated. The general aim of this part was to form a clear idea about the sophisticated nature of bio-molecules with the particular accent to their spectroscopic investigation by means of Raman spectroscopy.

2.3 Surface Enhanced Raman Scattering

2.3.1 Introduction to SERS, its plasmonic origin

The work by Fleischmann and coworkers in 1974 [Fleischmann 1974], who observed enormously strong and potential-dependent Raman signals from pyridine adsorbed on a silver electrode that had been electrochemically roughened in potassium chloride aqueous electrolyte, was interpreted as due to an increase in the effective surface area caused by the roughening of the electrodes. Subsequent experiments [Albrecht 1977, Jeanmaire 1977] provided the demonstration that the observed signal levels could not be accounted for by an increased surface area. In 1978 M. Moskovits [Moskovits 1978] proposed that the huge increase in Raman cross section was a result of the excitation of so-called surface plasmons,

Approximate assignment of vibrational mode	Wool	Stratum corneum
Amide A ν(NH)	3308	-
Amide B β(CNH)	3057	3070
(CH$_3$) asymmetric, ν(CH)	2971	-
ν(CH$_2$) asymmetric	2931	2935
ν(CH$_2$) symmetric	2877	2882
ν(CH$_3$) symmetric	2848	2854
ν(CH)	2732	2727
ν(C=O) lipid	-	1733
ν(C=O) Amide I; β-pleated sheet	1670	-
ν(C=O) Amide I; α-helix	1655	1651
Tyr, Trp ν(C=C)	1614	1617
Phe ν(C=C) in phase	1604	1606
Phe ν(C=C) symmetric	1585	1584
Trp	1553	1558
δ (CH$_2$)(CH$_3$)	1448	1443
Trp,	1420	-
(CH$_2$),Trp	1338	1338
ν(Cα-H)	1318	1316
Amide III ν(CN) δ(NH) α-helix	1266	1272
Amide III β-pleated sheet	1238	1253?
Tyr, Phe ν(C-C6H5)	1207	1208
Tyr, ν(CH) in phase	1176	1177
ν(CN)	1155	1158
ν(CN)	1125	1128
ν(CN)	1096	-
ν(CN)	1080	1080
ν(CC)	-	1062
Phe ν(CH) in phase	1032	1031
Phe ν(C=C) symmetric	1001	1003
(CH$_2$)	952	959
ν(CC) skeletal α-helix	934	937
ν(CC) skeletal α-helix	898	895
Trp skeletal and ν(NH) pyrrole	881	-
Tyr (ring breathing)	851	855
Tyr (out of plane ring breathing)	828	828
Trp	757	744?
ν(C-S) cysteine	661	-
Tyr (CC) ring twist	642	642
Phe (CC) ring twist	618	619
ν(S-S) cystine trans-trans	545	-
ν(S-S) cystine gauche-trans	532	-
ν(S-S) cystine gauche-trans	519	-
ν(S-S) cystine gauche-gauche	512	-

Table 2.2: Vibrational modes and assignments of wool and stratum corneum.

responsible for the surface enhancement in SERS.

Surface plasmon resonance is found in materials possessing the negative real and small positive imaginary dielectric constant (e.g. silver and gold). With the incidence of electromagnetic radiation on these materials a collective oscillation of surface conduction electrons is induced. When surface plasmons are confined to nanostructure much smaller than the wavelength of light, they are localized around the nanostructure with a specific frequency known as the LSPR (Localized Surface Plasmon Resonance) (see Figure 2.11). The plasmon resonant frequency is related to the metal dielectric dielectric constant that is measured as a function of wavelength for bulk material.

In general, there are two different origins of surface enhancement which are currently used [Moskovits 1985, Campion 1998, Otto 1992]. In one, the analyte is adsorbed onto or is held in close proximity to the metal surface, and the interaction occurs between the analyte and the plasmons (collective oscillations of free electron gas induced by external electromagnetic field). This is called electromagnetic enhancement. In the other, the adsorbate chemically bonds to the surface. Excitation is then through the transfer of electrons from the metal to the molecule and back to the metal again. This is called charge transfer or chemical enhancement. By definition it can only be possible from the first layer of the analyte attached to the surface whereas electromagnetic enhancement could occur from a second or subsequent layer.

2.3.1.1   Relationship between the dielectric function and resonance conditions

In order to understand the LSPR resonance condition, it is important to underline the physical meaning of the dielectric constant. It describes behavior of a material when it is immersed in an electric field and is therefore also related to the polarity of the material. The complex dielectric function demonstrates a way of how a material's optical properties are dependent in the incident wavelength of light and can be described by $\varepsilon_{in}=\varepsilon'+i\varepsilon''$, where ε' and ε'' are the real and imaginary dielectric functions. The Lorentz model [Bohren 1983] describing these parameters gives just the dependence of the dielectric function on the frequency of the incident field. But in case of the conductors possessing free electrons the Drude model is valid. Being similar to Lorentz model, in Drude model the electrons are supposed to move about freely, causing the absence of restoring force, such that ω_0 is zero. Thus, the equations for the real and imaginary dielectric functions are reduced to:

$$\varepsilon' = 1 - \frac{\omega_p^2}{\omega(\omega^2 + \gamma^2)} \tag{2.17}$$

$$\varepsilon'' = \frac{\omega_p^2\gamma}{\omega(\omega^2 + \gamma^2)} \tag{2.18}$$

here, the plasma frequency (ω_p) is described by

$$\omega_p^2 = \frac{Ne^2}{m\varepsilon_0} \tag{2.19}$$

where m is the electron mass, e is the electron charge, and N is the free electron density. In case $\omega \gg \gamma$, which is common for metals at room temperature, as could be seen from Eqs. 2.17 and 2.18, the real part of the dielectric function is negative when the plasmon frequency is higher than the frequency of incident light. Thus, metals have a negative real dielectric constant because of high density of free electrons leading to a high plasmon frequency.
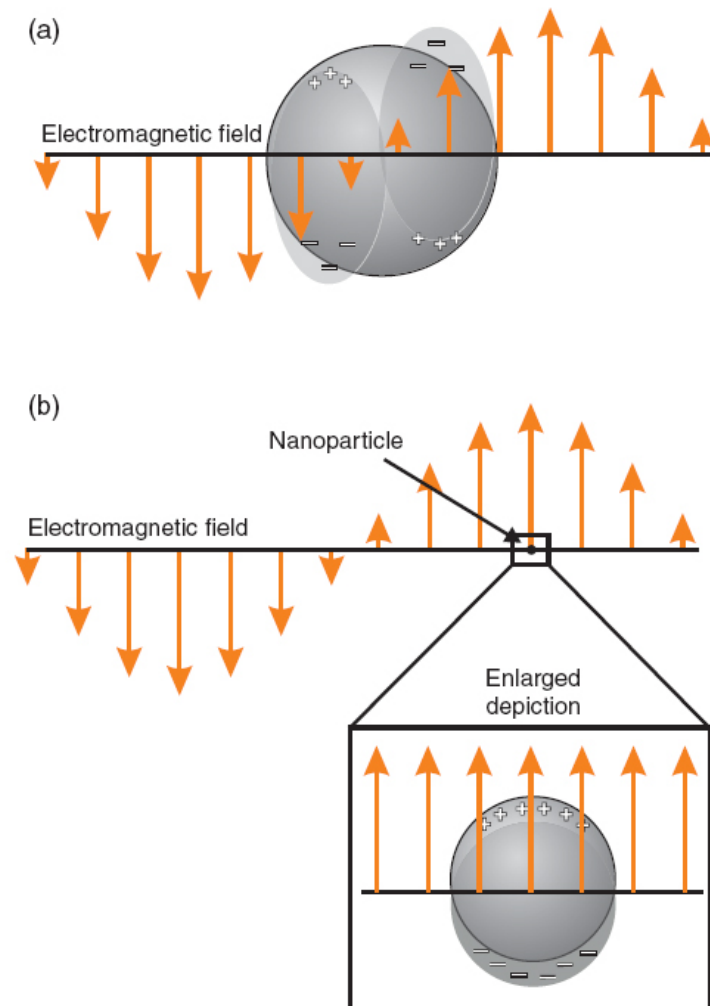
Figure 2.11: Sketch of an interaction of light with a spherical metal nanoparticle. (a) General case. The field distribution in the nanoparticle is inhomogeneous, which leads to a complex optical response. (b) Quasistatic regime. The upper part shows the proportion between the nanoparticle and the wavelength. The lower part is an enhanced view, It shows that, for sufficient small particles, the field distribution in the nanoparticle is, in a first approximation, homogeneous.

2.3.1.2 Quasistatic approximation

The quasistatic approximation allows an easy derivation of the optical properties of small metal nanoparticles embedded in a dielectric matrix, and although it holds only under strict limitations, it is essential for a fundamental understanding of the optical properties of metal nanoparticles.

The internal field of a nanoparticle can be written as [Maier 2007]:

$$E_{int} = E_0 \frac{3\varepsilon_m}{\varepsilon + 2\varepsilon_m} \tag{2.20}$$

and the external field

$$E_{ext} = E_0 \frac{3n(n \cdot p) - p}{4\pi\varepsilon_0\varepsilon_m} \frac{1}{r^3} \tag{2.21}$$

where r is the distance from the particle surface, p - is the dipole moment, and n the unit vector in the direction of the point of interest. The size of the nanoparticle must be smaller than the skin depth d_{skin} of the metal ($d_{skin} = \lambda/4\pi\sqrt{\varepsilon}$) because of exponential decaying of the electromagnetic field in metals. For larger nanoparticles, the field distribution inside the nanoparticle becomes inhomogeneous and the quasistatic approximation is no longer valid. The extinction, scattering and absorption cross section in quasistatic approximation are derived considering a nanoparticle illuminated with an oscillating electromagnetic field E(t)=E$_0$exp($-i\omega t$), which induces the time-dependent dipole moment p(t) (see Figure 2.11(b)). Analogously to the electrostatics, one finds:

$$p(t) = \varepsilon_0\varepsilon_m\alpha E(t) \tag{2.22}$$

Taking into account the Clausius-Mosotti relation $\alpha = 4\pi R^3 \frac{\varepsilon - \varepsilon_m}{\varepsilon + 2\varepsilon_m}$, where ε is the dielectric function of the nanoparticle material. Thus, the polarizability of a special nanoparticle as well as its internal and external field show a resonance behavior whenever

$$|\varepsilon + 2\varepsilon_m| = minimum \tag{2.23}$$

that is,

$$[\varepsilon_{Re}(\omega) + 2\varepsilon_m]^2 + [\varepsilon_{Im}(\omega)]^2 = minimum \tag{2.24}$$

where ε_{Re} and ε_{Im} are the real and imaginary parts of the dielectric function of the nanoparticle. With the linear limitations to the size of nanoparticle such as $R<0.06\lambda$, the induced excitation due to the electromagnetic field can be described as Hertzian dipole, that is, an antenna that effectively absorbs electromagnetic radiation. The absorption cross section of a nanoparticle is given by [Kreibig 1995]:

$$\sigma_{abs} = k \cdot Im\{(\omega)\} = 4\pi k R^3 Im\left\{\frac{\varepsilon - \varepsilon_m}{\varepsilon + 2\varepsilon_m}\right\} \tag{2.25}$$

and the scattering cross section by

$$\sigma_{sca} = \frac{k^4}{6\pi}|\alpha(\omega)|^2 = \frac{8\pi k R^6}{3}\left|\frac{\varepsilon - \varepsilon_m}{\varepsilon + 2\varepsilon_m}\right|^2 \tag{2.26}$$

with the wave number $k = (2\pi/\lambda)$. Equations 2.25 and 2.26 show that the absorption and scattering cross sections exhibit a resonance behavior whenever Re$\{\varepsilon(\omega)\} = -2\varepsilon_m$. The sum of absorption and scattering cross sections yields the extinction cross sections, which is usually determined in an experiment:

$$\sigma_{ext} = \sigma_{abs} + \sigma_{sca} = 12R^3\varepsilon_m^3\frac{\omega}{c}\frac{\varepsilon_2}{\left[\varepsilon_1 + 2\varepsilon_m\right]^2 + \varepsilon_2^2} \tag{2.27}$$

Because of proportionality of the polarizability of a nanoparticle to its volume (see Clausius-Mosotti relation), the absorption scales with the third power and the scattering with the sixth power of the nanoparticle radius in the extinction cross section. Moreover, in case $R < 0.06\lambda$, the scattering is very small compared to the absorption and it could be written:

$$\sigma_{ext} \cong \sigma_{abs} \tag{2.28}$$

Thus, the quasistatic regime is characterized by the dominance of absorption over scattering. The cross section of absorption of a spherical nanoparticle is given by Lorenz curve [Vartanyan 2001]:

$$\sigma_{abs}(\omega, \Omega) = \frac{\pi R^3 \gamma \omega_p^2}{3c} \cdot \frac{1}{(\omega - \Omega)^2 + (\gamma/2)^2} \tag{2.29}$$

Since $\Omega = \frac{\omega_p}{\sqrt{1+2\varepsilon_m}}$ the position of the LSPR depends on the dielectric environment. Figure 2.12 displays the calculated extinction spectra of silver nanoparticles with R=10 nm for different dielectric media. As can be seen the LSPR is clearly shifted to lower photon energy for increasing ε_m. Meanwhile, the increase of the extinction amplitude is due to the dependence of the dielectric function on the photon energy.
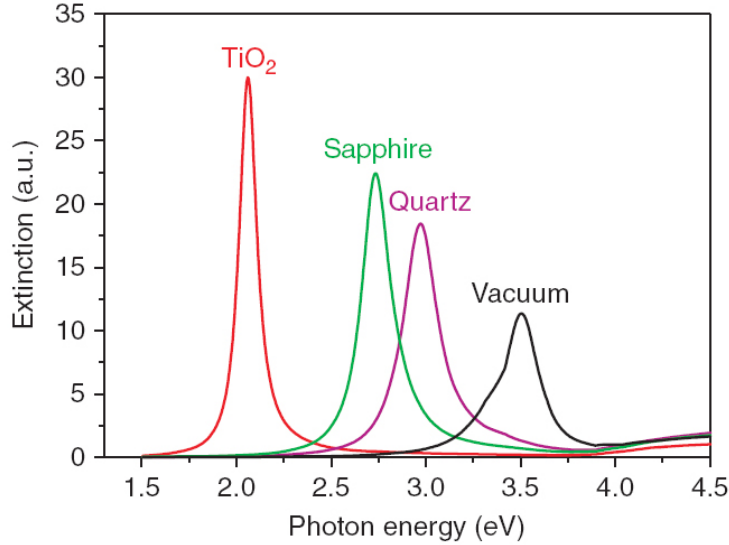
Figure 2.12: Optical spectra for spherical silver nanoparticles with a radius of R=10 nm in different media (vacuum: $\varepsilon_m = 1$, quartz: $\varepsilon_m = 2.311$, sapphire: $\varepsilon_m = 3.125$, TiO$_2$: $\varepsilon_m = 7.023$), calculated using the quasistatic approximation.

2.3.2   Electromagnetic enhancement

Due to the experimental discovering of the technique, many theories were proposed [Arunkumar 1983, Arya 1984, Rojas 1993]. But, the main problem is that our ability to

describe theoretically the bonding or adsorption of an organic molecule to a roughened, probably corroded and oxidized metal surface in water is very limited. Essentially, most authors now accept that there are two parts to the theory and that both have some validity. This promotes a working theory which enables experimental work to proceed with little controversy over the nature of the effect. However, the true nature of the theory is still a very active research field [Lombardi 2012].

As known, the effectiveness of Raman spectroscopy depends, among other factors, on the intensity of the local electric field "seen" by the molecule. Thus, due to its' inherent features, plasmon resonance can result in huge magnification of the local field at the metallic surface. Therefore, rough metallic surfaces or metal nanoparticles under plasmonic excitation are acting as antennae, as it had been demonstrated before, achieving scattering cross section enhancements of about eight orders of magnitude [Campion 1998].

The simplest description of electromagnetic SERS is based on models of a small metallic sphere. Consequently, the simple sphere could be regarded as a first approximation to a single colloidal particle even if it is known that aggregation of suspensions of these particles gives much increased SERS. However, the sphere model is used to explain the much of the basic process [Smith 2005]. When a small metal sphere is subjected to an applied electric field from the laser, the field at the surface is described by

$$E_R = E_0 \cos\theta + g\left(\frac{a^3}{r^3}\right) E_0 \cos\theta \tag{2.30}$$

- E_R is the total electric field at a distance r from the sphere surface,

- a is the radius of the sphere,

- θ is the angle relative to the direction of the electric field,

- g is a constant related to the dielectric constants such that,

$$g = \left(\frac{\varepsilon_1(\nu_L) - \varepsilon_0}{\varepsilon_1(\nu_L) + 2\varepsilon_0}\right) \tag{2.31}$$

ε_0 and ε_1 are the dielectric constants of the medium surrounding the sphere and of the metal sphere respectively, ν_L is the frequency of the incident radiation. From the last equation is obvious that when the denominator is at minimum, the value of g goes to maximum. ε_0 is usually close to 1 and consequently this maximum usually occurs when ε_1 is equal to -2. At this frequency, the plasmon resonance frequency, the excitation of the surface plasmon greatly increases the local field experienced by the molecule absorbed on the metal surface. In short, the molecule is bathed in a very freely moving electron cloud and that movement intensifies the polarization of the surface electrons. The electrons in the analyte molecule absorbed on the surface interact with this cloud causing greater polarization around the molecule.

At the metal surface the total electric field is averaged over the entire surface of a small sphere. At any point in the surface the electric field may be described by two components, the average field perpendicular to the surface and the average field parallel to the surface. Clearly, g is dependent on the dielectric constants of the metal and the surrounding medium and also the laser frequency. Since the dielectric constant of the metal is generally about 1, it can be seen by substituting this into 2.30 and 2.31, that the electric field is greater perpendicular to the surface than parallel to it. Thus, the greatest enhancement is observed for a molecule adsorbed on the surface and polarized perpendicular to it. Further, as it could be seen from the formula 2.31 the magnitude of SERS enhancement drops off rapidly with distance from the surface.

2.3.3   Charge transfer: chemical enhancement

Electromagnetic enhancement should be a nonselective amplifier for Raman scattering by all molecules absorbed on a particular surface. In order to tackle the interpretation of the observed SERS-spectra the effect of the electronic interactions between the metal and the adsorbate should also be considered. As Otto [Otto 2005] wrote, "...without the EM mechanism there would be no signal. But the chemical mechanism determines what is observed." This causes the fundamental fact that the observed SERS spectra contains the information about the adsorbate and its environment, in particular its interaction with the enhancing nanoparticle, its spatial orientation and the polarization properties of the local electric field [Aroca 2007].

Charge transfer or chemical enhancement [Otto 1992] associated with the overlap of the wave functions of the electron in the metal and the electron in the adsorbate molecule resulting in the tunneling of the electrons between the metal and the molecule. Thus, finally the formation of a bond between the analyte and the metal surface occurs. This bond is believed to produce a surface species which includes the analyte and some surface metal atoms. This provides the charge transfer (electrons or holes) from the metal surface into the analyte. The formation of this surface increases the molecular polarizability of the molecule considerably due to interaction with the metal electrons. Fundamentally, the enhancement is thought to originate from new electronic states which arise from the formation of the bond between analyte and metal surface. These new states are believed to be resonant intermediates in the Raman scattering. Thus, as opposed to the radiation being absorbed or scattered through the plasmons on the surface, the radiation is absorbed into the metal. A hole is transferred into the adsorbate metal atom cluster, the Raman process then occurs, excitation is transferred back into the metal and re-radiation occurs from the metal surface.

Different charge transfer mechanisms have been proposed. The mechanism proposed by Chang [Chang 1987] involves following four steps:

1. an incident photon with the energy ω created an electron-hole pair in the metal,

2. the electron of this pair transfers to the excited state electronic level of the absorbate via tunneling for physisorbed adsorbates or via hybridization for chemisorbed adsorbates,

3. the electron from the excited level of the adsorbate transfers back to the metal into a state with lower energy in comparison with the electron simultaneously created together with the hole, leaving the adsorbate in the higher vibrational level,

4. the recombination of the electron from this lower energy state with the hole resulting in the emission of a photon with lower energy $\omega' < \omega$.

Apart from the mechanism of Chang there are also other chemical effect mechanisms with the transfer of an electron between the adsorbed molecule and the metal:

- The incident photon excites an electron from the molecular ground state upward shifted and broadened due to the chemisorption (E_a) to an unoccupied metal state above the Fermi level by the intermediate of some excited molecular state (Figure 2.13a)

- The incident photon excites an electron in a partially filled molecular state (E_a) in the vicinity of the Fermi level E_F to a vacant metal state through the intermediate of the states in the occupied part of the initial partially filled molecular state (E_a), (Figure 2.13b).

- The incident photon excites an electron from the metal with the energy near the Fermi level E_F to an excited state of the negative electron-molecule complex (Figure 2.13c).
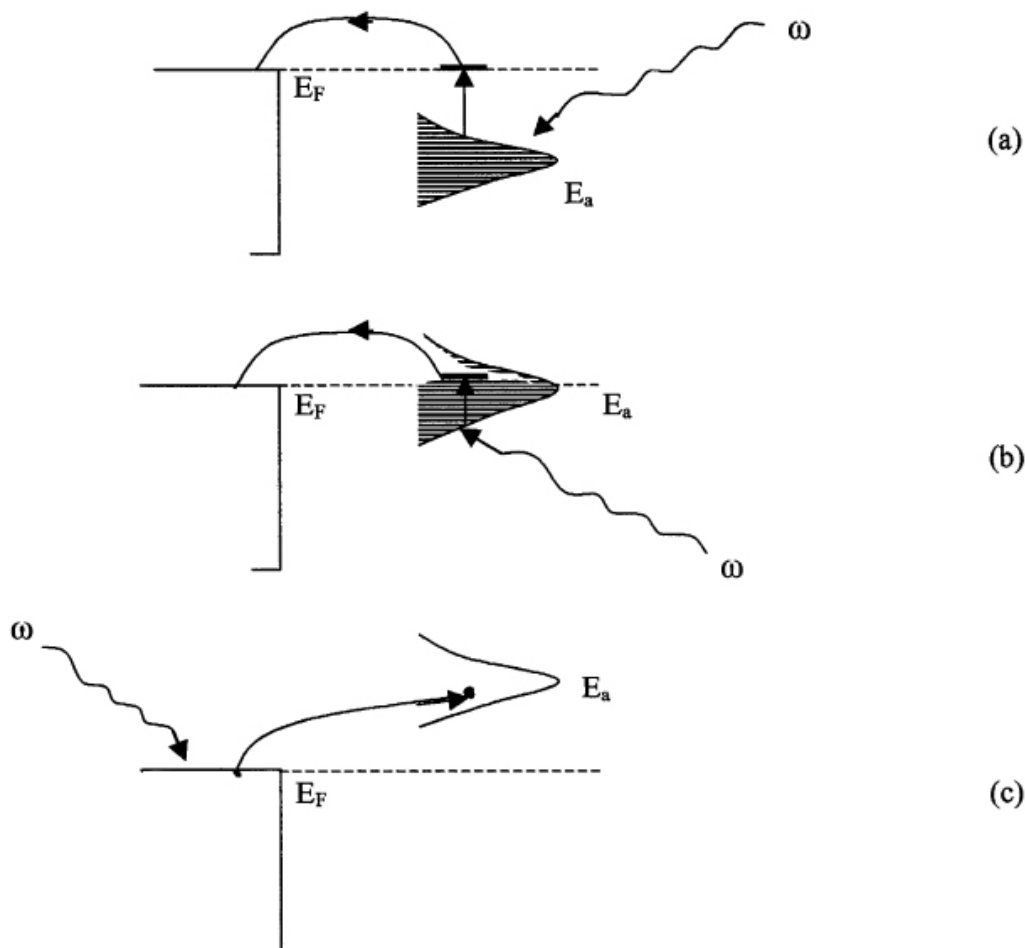
Figure 2.13: Schematic illustrations for possible charge transfer excitation between adsorbed molecule and metal.

In all the mentioned charge transfer processes the Raman polarizability is substantially enhanced when the frequency of the incident or scattered photon become in the resonance with the coupled molecule-metal system. Though of conceptual differences, an exact separation of two distinct enhancement processes is extremely challenging and experimentally very difficult, as any parameter easily changed in the experimental design results in influence on both mechanisms. A detailed understanding of the chemical enhancement and a reliable separation from purely electromagnetic enhancement is thus not only relevant for fundamental reasons but also crucial for the design of analytical tools. Taking into account that both enhancement mechanisms are multiplicative, unexpected chemical enhancements can easily lead to quantitatively and qualitatively wrong analytical conclusions. In order to simply increase the Raman scattering cross-section, surface-enhanced resonance Raman scattering (SERRS) can be used. In this case, the excitation wavelength is not only in

resonance with the surface plasmon absorption but more importantly also resonant to the electronic absorption of the adsorbed molecules. Thus, surface enhancement of the Raman signal appears combined with the adsorbate intrinsic enhancement of the scattering due to the dispersion of $\frac{\delta\alpha}{\delta q}$.

2.4   Advantages of SERS for studies in Cells

As it had been shown, the SERS-enhancement is restricted to the immediate vicinity of a metal nanostructure. Nevertheless, SERS techniques extremely attractive for efficient live-cell Raman approaches because of the independence from a specific laser wavelength for excitation of the Raman scattering and the ability to probe many different kinds of molecules.

Considering the development of such an approach, the local confinement of the SERS effect is worthwhile to be kept in mind in order to be managed and converted into oneâs advantage. In-vivo SERS studies are conducted with individual probes positioned at discrete locations in the cell. Thus, the nano-environment of these SERS probes becomes the only origin of the spectral information. This is the fundamental difference from the spectral information obtained in a "normal" Raman microspectroscopic experiment, where all positions in a whole cell are probed.

The very sensitive detection, together with the confinement of the spectral enhancement in SERS to the immediate vicinity of the nanoprobes makes SERS probes ideal tools for the investigation of small morphological structures in cells. The excitation wavelength is no longer a limit for the maximum lateral resolution, cause it is influenced by the metal nanostructure used to provide the enhancement.

Overview of the existing SERS substrates synthesis techniques

3.1 Short review on traditional and non-traditional methods of synthesis

Due to the large body of existing methods for the synthesis of nanoparticles (NPs), as the fundamental base of every SERS substrate, there are also slightly different classification of synthesis methods that can be met. For example, they can be subdivided into traditional and non-traditional [Evanoff 2005]; or top-down and bottom-up [Hubenthal 2011] (see Figure 3.1).
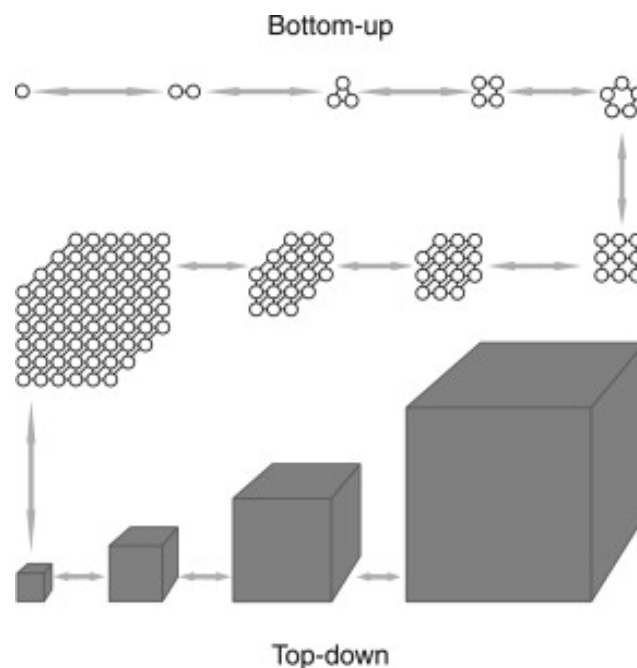
Figure 3.1: The principal routes to obtain nanostructures: top-down and bottom-up.

Traditional, the most widespread ones are those solution-phase synthesis techniques (i.e. related to the family of bottom-up techniques) that are based on various modifications of the Lee-Meisel [Lee 1982] or Creighton [Creighton 1979] methods (being the oldest method to synthesize metal NPs, now represent an extremely broad variety of synthesis routes and, as consequence, an extraordinary variety of NPs that can be generated, including core-shell, multi-shell NPs), i.e. are different variations of wet-chemical preparation techniques

(e.g. colloidal methods), and there are a lot of examples in which different salts and agents are used [Shirtcliffe 1999, Cason 2000, Li 2003, Sondi 2003]. Nanoparticle oxidation promoted by the large positive reduction potential of Ag, is thermodynamically unfavorable resulting in a quite stable aqueous and alcoholic suspensions without the aid of capping ligands. Aggregation can be hindered either by steric hindering or by electrostatic repulsion. The last one is usually obtained by the chemisorption of charged species (usually H^+ or OH^-) at the NP surfaces [Cushing 2004]. For high ionic strengths or organic-phase suspensions, capping agents such as self-assembled monolayers, [He 2001, Li 2003] surfactants [Cason 2000, Sondi 2003, Maillard 2003], polymers [Chen 2002a, Velikov 2003] and dendrimers [Esumi 2000, Crooks 2001] can be employed to protect the particles from aggregation. If the synthesis is carried out in the presence of capping agents, however, anisotropic particles may result due to the differing affinities of the ligands to the exposed crystal faces. This is sometimes a desired effect and several researches have shown that various shapes can be produced through judicious use of stabilizing agents [Chen 2002b, Maillard 2003]. Alternatively, NPs can be capped with desired molecules after the synthesis to facilitate their transfer into non-polar phases or to tailor their surface chemistry.

The final size and shape of the NPs synthesized is determined in a sufficient way by the amounts of the additives, concentration of reactants and the preparation conditions [Vlčková 1997, Si 2009]. For example, for golden NPs synthesized by Turkevich method [Turkevich 1951] the appearance of different shapes is avoided if instead of citric acid trisodium citrate is used, which in turn promotes the relatively small size distributions with widths of Gaussian size distribution of only $\sigma=10$ %. It is worth-noting that the reducing agent can be used both as the reducer and stabilizer simultaneously [Duff 1987a, Duff 1987b]. As to *characteristic advantages of wet chemical methods*, the most salient are:

1. no specialized equipment is necessary;

2. solution based processing and assembly can be readily implemented;

3. large quantities of NPs can be synthesized [Tao 2008].

Another valuable issue of the colloidal NPs application is their aggregation by addition of an adsorbate and/or of a pre-aggregating agent, thus promoting the controlled clustering of silver NPs, since the highest enhancement factors are expected in the nanosized gap between two aggregated metallic NPs. Unfortunately, the pure aggregated colloids in some cases show specific Raman modes assignable to citrate (reducing agent) or nitrate. Thus, the detection of the molecules of interest might be hindered by the strong SERS contribution of the aggregated metal colloids itself [Yaffe 2008]. Worth-noticing, that the parent chemically prepared colloids are usually very stable. And the last as well as the mechanism of their formation are influenced by several factors [Vlčková 1997]:

- the chemical nature of the adsorbate, which determines the type of adsorbate-surface interaction (physisorption, chemisorption),

- concentration of the adsorbate, affecting the actual surface coverage,

- concentration of residual ions stabilizing the parent colloid,

- temperature,

- during the SERS experiment, the Ag colloid/adsorbate system can further be affected by laser induced adsorption/desorption and aggregation/deaggregation processes.

- possible chemical competition with the analyte (e.g. Methyl Orange)

- moreover, silver colloidal aggregates containing more than ca. 100 particles were proved to be a fractal objects

Apart from the precautions listed, there are a number of works dedicated to the overcoming the constraints presented to a considerable extent [Tantra 2007, Tao 2008, Jarvis 2008, Zhang 2014]. At the same time solution chemistry methods typically consume a large amount of organic solvents and hazardous chemicals that are considered environmentally unfriendly. Therefore, addressing this issue, a number of the eco-friendly solutions has been proposed in current literature [Nanda 2009, Fayaz 2010, Xu 2013]. Besides of the numerous SERS advantages, unfortunately, it has had limited commercial success in routine trace analysis due to the 'basic reproducibility criteria' which have not been properly addressed [Natan 2006]. And this is particularly the situation when colloids are employed as the substrate. Despite such problems, the use of colloidal SERS is widespread as the substrates are easy to synthesize at low cost and are highly dispersible also [Tantra 2007].

Non-traditional, synthesis methods (which are also related to the family of bottom-up techniques) include Ag particle synthesis through high-temperature reduction in porous solid matrices [Plyuto 1999, Wang 2002], vapor-phase condensation of a metal onto a solid support [Jensen 2000, Zhao 2002, Malynych 2003], laser ablation of a metal target into a suspending liquid [Mafuné 2000], photoreduction of Ag ions [Huang 1996, Abid 2002], and electrolysis of an Ag salt solution [Kotov 1993, Zhu 2000].

Thus, all the methods listed, possess some inherent problems, and while each method have certain advantages and disadvantages, the selection of a proper synthetic procedure depends on the nature of the specific application. Considering **traditional methods**, the major problem is often a *limited flexibility in the size of particles* that can be produced and such methods are usually sold in their ability to make 10 nm particles. Again, depending on the application, small particles, e.g. are desirable in catalysis, where the main emphasis is on the surface-to-volume ration, but for optical applications, larger particles are often necessary. Small Ag NPs do not interact with light nearly as efficiently as particles that are in the 50-100 nm range and do not strictly through energy absorption. On the other hand, the plasmon resonances in larger Ag NPs have a significant light-scattering component that can be advantageously used in applications that require efficient optical labels, such as in chemical assays. The major problems for the **non-traditional** methods often are:

- a wide size distribution,

- lack or particle crystallinity,

- the cost and scalability of the production.

Thus, the optimum synthetic method should address all of the above problems and additionally yield particles with no extraneous chemicals that can potentially alter the particle's optical properties and surface chemistry. The above discussion, certainly, does not exhaust a complete listing of the available synthetic methods, but most likely a variant of a broad representation of what has been reported. Thus, further description of the synthesis techniques will be based on two routes for NPs production: top-down or bottom-up.

3.2 Top-down techniques

Top-down technique, is dealing with dividing or structuring a macroscopic piece of material in small parts (e.g. photolithography (see Figure 3.2) or particle beam lithography).

The major obvious advantages of these techniques is the synthesis of high ordered NPs with a narrow shape and size distribution on substrates. Also, it should be noted, that
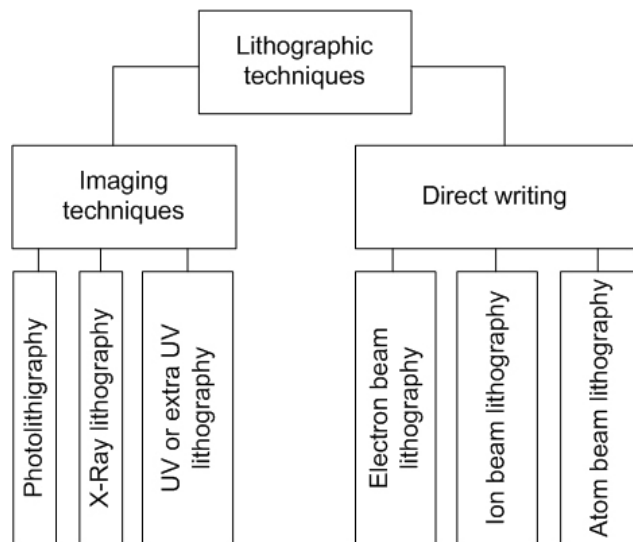
Figure 3.2: The variability of lithographic techniques.

laterally arbitrary shaped NPs also have been synthesized using lithographic techniques [Lamprecht 1999, Aeschlimann 2009, Berndt 2009]. As to the drawbacks, *photolithography is diffraction limited* and, in particular particle beam lithography (ions or electrons), is *extremely time-consuming and expensive*, requires clean rooms and special nanofabrication tools and often cannot be sufficiently up-scaled [Sánchez-Iglesias 2010]. Due to the free individual selection of the lateral shape as well as the height of the NPs, the LSPPR of the NPs generated can be easily tuned from the IR to the near-UV. This flexibility is the prerequisite for a number of fundamental and practical applications. The *main advantage of photolitography* is the *parallel process technique*, essential for mass production. However, it suffers from the fact that it is limited by the Abbe-Rayleigh criterion:

$$\mathbf{d}_{min} = 0.61 \frac{\lambda}{n sin\alpha} = 0.61 \frac{\lambda}{NA} \tag{3.1}$$

where d_{min} is the minimal size of a structure illuminated with the point light source with wavelength λ, n the refraction index of the environment, α the aperture angle, and NA the numerical aperture of the system. Therefore, *for small structures, high numerical apertures and short wavelengths have to be used*.

Another weak spot is that the side walls of the generated structures are usually perpendicular to the substrate surface. Thus, while laterally the shape can be chosen freely, the side walls cannot. Nice example of this problem overcoming was presented by [Kontio 2009] (see Figure 3.3). The solution based on the generation of the conical metallic nanostructures by applying a two-step lithographic process and exploiting the shadowing effect of the deposited metal. The second step of the process is schematically represented in Figure 3.3(a). After the patterning of the poly methyl methacrylate (PMMA) resist and the subsequent reactive ion etching to generate holes in it, the metal over the structure has been deposited. Notably, that the germanium acts as an adhesion promoter. The generated deep holes start to be overgrown by the metal during deposition. Thus, the clear cross section

becomes smaller and nanocones are generated. The last step is lift-off of the PMMA resist mask. As can bee seen from the Figure 3.3(b) the structures generated are highly ordered and reproducible.
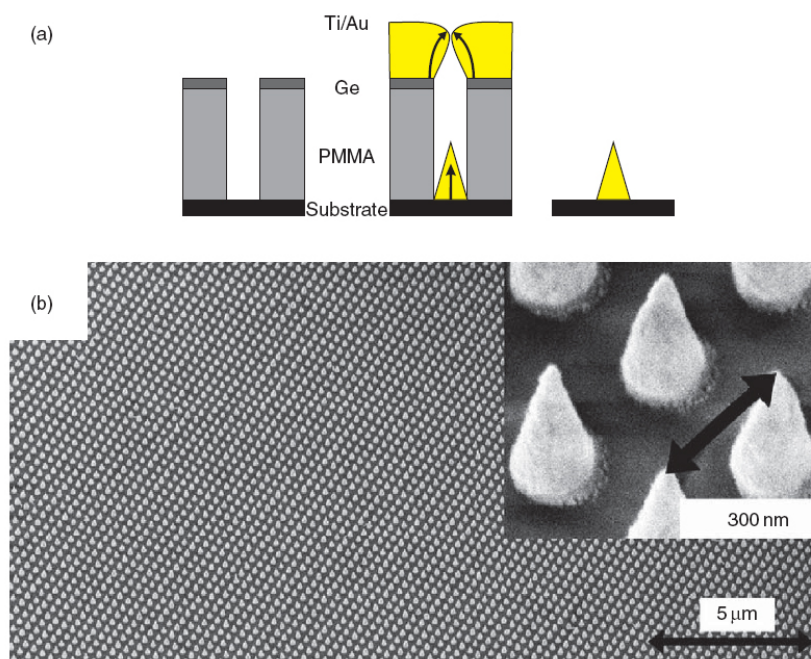
Figure 3.3: Metallic nanocones prepared by an advanced lithographic technique.

Electron beam lithography is a direct writing and differs significantly from the photolithography. It is a *time-consuming serial process* and an expensive technique. As to the main advantage of EBL is the fact that extremely small nanostructures can be achieved. Theoretically, nanostructures with lateral dimensions below 1 nm are possible due to the short de Broglie wavelength of electrons [Berger 1991]. In reality, the resolution is limited to approximately 10 nm because of the proximity effect, that is, the forward and backward scattering of the electrons in the resist. As illustrated in Figure 3.4, the scattered electrons penetrate in an area of the resist far away from the incoming electron beam. In the critical case, a strong widening of the focused electron beam may occur, which results in dramatic limitation of resolution. In the ideal case, EBL has a resolution of approximately 10 nm, which allows in practice a preparation of NPs with lateral sizes down to 20 nm.

The fact that the dose at a certain moment is the sum of the dose of the incoming and back-scattered electrons gives rise to another consequence of the proximity effect - large illuminated structures are exposed to a higher dose as small areas (see Figure 3.4). Therefore, when small and large structures are generated at the same time, the dose must be adjusted during the illumination of the resist, taking into account the structure size [Kratschmer 1981]. Thus, the dose must be predetermined in advance, on the base of the proximity function, which is composed of the Gaussian intensity distribution of the incoming and back-scattered electrons [Chang 1975]. Despite its limitations given above, EBL has a significant advantage: almost any lateral shape of the nanostructures can be achieved, e.g. nanostars [Aeschlimann 2009], heart-shaped NPs [Lamprecht 1999], cloverleaf-shaped particles [Berndt 2009] (see Figure 3.5) to name a few.
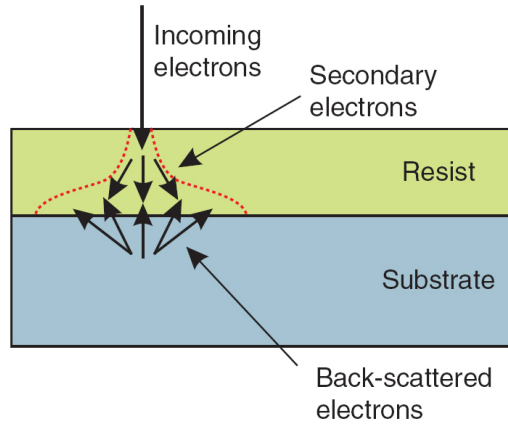
Figure 3.4: Influence of the scattered electrons on the illuminated area of the resist. The dashed line indicates the area, affected from the scattered electrons.
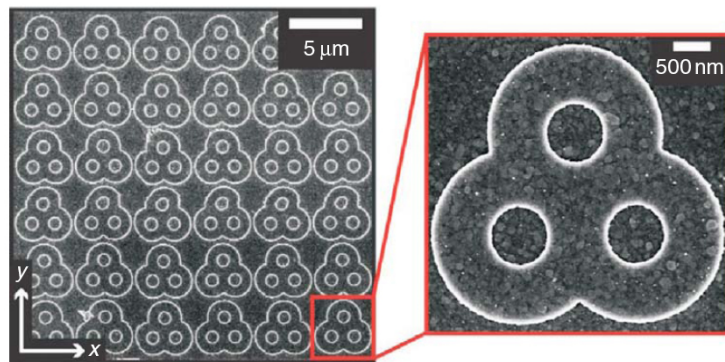
Figure 3.5: Silver-coated silicon cloverleaf-shaped structure prepared by means of electron beam lithography. [Berndt 2009]

Nanosphere lithography, NSL, which was invented in 1980s by U.Fischer [Fischer 1981], in contrast to the above-mentioned techniques, is inexpensive, allowing a high throughput, able to generate highly ordered NPs with lateral sizes between 30 nm and several micrometers. But in the same time, NSL has a serious drawback: the approach is constrained to triangular- or hexagonal-shaped NPs arranged in a defined order on the substrate (see Figure 3.6).
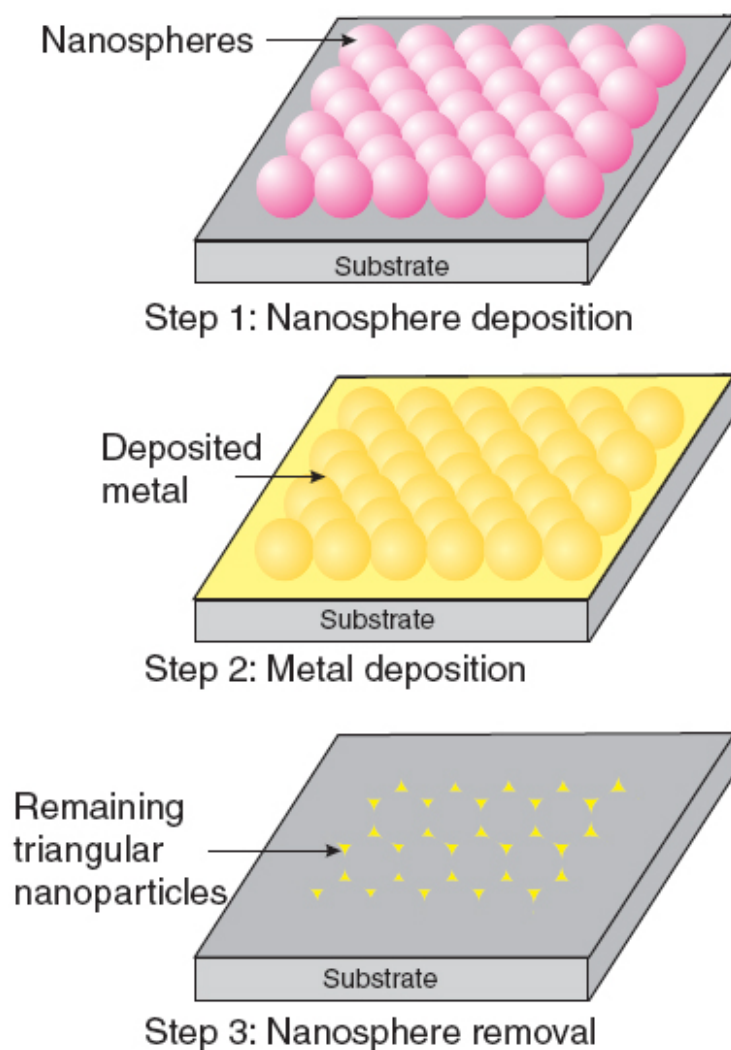
Figure 3.6: Schematic illustration of NSL.

Being one of the major step of the technique - self-assembly of the nanosphere mask, has blossomed in a variety of approaches that have been successfully applied [Dimitrov 1996, Matsushita 1997, Morarescu 2009]. Despite of this variability of preparation techniques for NSL, the principal preparation steps are the same in all cases. It consists of three major steps, as illustrated in Figure 3.6:

1. deposition of the nanospheres from a solution onto a carefully cleaned substrate. Thus, by self-assembly, a monolayer of hexagonally ordered nanospheres on the substrates is obtained.

2. highly ordered nanospheres act as the lithographic mask during the subsequent deposition of the metal (step 2).

3. the nanospheres are removed, leaving behind a highly ordered array of triangular NPs.

The driving forces behind the ordering of the nanospheres on a substrate are capillary forces. The details of two-dimensional crystallization of the nanosphere arrays under the direct influence of the capillary forces can be found in [Nagayama 1993, Kralchevsky 1994]

Spin coating, is a both an usual way to prepare a thin liquid layer on a substrate applied in NSL for the preparation of monolayers of closely packed nanosphere on different substrates [Hulteen 1995, Velev 2000, Wang 2004] and an independent technique used to obtain thin films, e.g. of block copolymer [Cho 2012]. The parameters modulating the final result are: the spin speed, the viscosity of the solution, and the solvent evaporation rate.

Tilt coating, (see Figure 3.7) which has been introduced by Micheletto et al. [Micheletto 1995] is rather simple and frequently used by many groups [Morarescu 2009, Hubenthal 2009a].
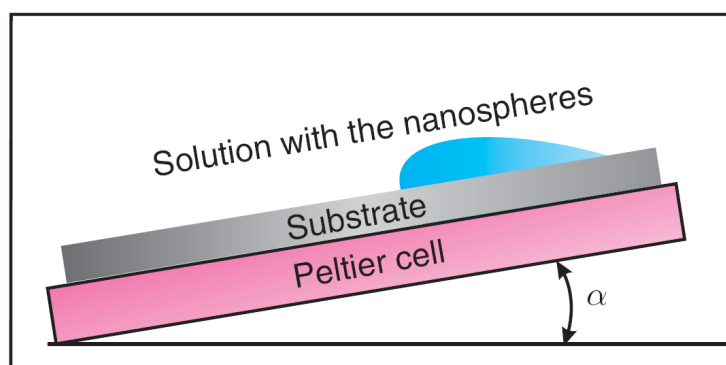
Figure 3.7: Principle of tilt coating.

The advantage of tilt coating, apart its simplicity, is that nanospheres with diameter down to 50 nm can be arranged on the substrates. The only limitation of the method is the necessity of very smooth and hydrophilic substrates, but this drawback has been successfully overcome by using floating technique [Burmeister 1997].

Dip coating is another preparation technique which has been described by Dimitrov and Nagayama [Dimitrov 1996]. In short, for the dip coating the substrate is immersed in a solution with the nanospheres and then extracted with the constant velocity under controlled humidity and temperature (see Figure 3.8). The formation of dense two-dimensional nanosphere arrays requires a certain extracting velocity of the substrate v_w, which is equal to the growth rate σ^k. It is given by ref. [Dimitrov 1996]:

$$v_w = \sigma^k = \frac{k}{0.605} \frac{j_e \phi}{kd(1 - \phi)} \tag{3.2}$$

The equation presented underlines one of the most crucial drawbacks of the method - a long time - from several hours to few days -required for the layer formation of small spheres due to the strong dependence of the growth rate on the inverse diameter of the nanospheres.

A general observation should be mentioned with respect to all coating methods. Since the evaporation rate strongly influences the nanosphere formation, the evaporation process has to be precisely controlled [Hubenthal 2011], by means of the temperature and humidity supervision. So long as low temperatures and high humidity strongly reduce the evaporation
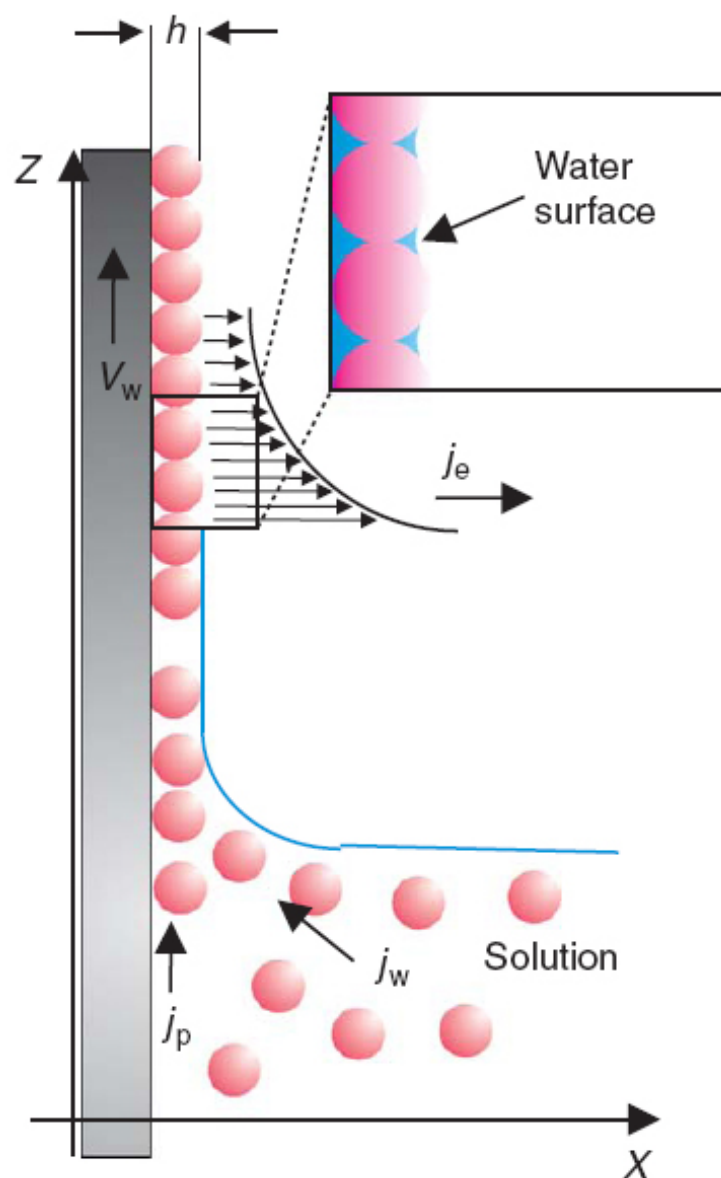
Figure 3.8: Monolayer formation by means of dip-coating. Ref. [Dimitrov 1996]

rate, the last in turn favors the formation of highly ordered nanospheres in a hexagonal array due to the avoiding of agglomeration and defect formation.

Summarizing, NSL is an inexpensive technique to generate highly ordered NP arrays, applicable to various materials and ready virtually for every smooth substrate. The optical properties of triangular NPs are tunable from the visible to near IR region, simply by changing the aspect ratio of the NPs. Moreover, NSL allows a high throughput and has proven to be extremely useful for many principle studies, e.g. in SERS [Haynes 2003b, Félidj 2004] or in biosensing [Haes 2002, Haes 2004]. Thus, NSL undoubtedly has a great potential, but also a limitation: the lateral NP size and the distance between the NPs cannot be chosen freely. Fortunately, modern literature provides the solution of this problem (angle resolved NSL and thermal annealing), the details of which can be found in [Haynes 2002, Haynes 2003a] and [Sun 2005, Tan 2005] correspondingly.

Focused ion beam technique. FIB is based on direct sputtering or milling of a thin metal layer. In principle, an FIB can also be used to deposit material. But, this approach is extremely time-consuming and thus practically not applied to generate NPs. Besides this, the main advantage of structuring by means of FIB is the direct writing ability, which does not need any lithographical or chemical processes. At the same time the major drawbacks are the extremely time-consuming process and the high cost. That is why it is very rarely applied to generate NPs.

3.3 Bottom-up synthesis techniques

The bottom-up synthesis of NPs is the central point of this thesis and in the recent past these approaches have received an increasing interest, cause fundamentally based on well established and universally recognized recipes [Turkevich 1951], [Lee 1982], [Creighton 1979], [Leopold 2003].

The *basis of bottom-up techniques is self-organizing processes of single atoms or molecules where NPs are generated gradually*. Using the techniques such as wet chemical synthesis, gas-phase production, or deposition of atoms on substrates, NPs consisting of a countable number of atoms (clusters), can be easily prepared. Moreover, laser evaporation techniques and wet chemical synthesis yield a *mass production* of small NPs. The last is physically unattainable by particle-beam lithography. As to the disadvantages of bottom-up techniques, generally NPs ensembles with a broad size and shape distribution are generated. Overcoming this drawback requires great effort [Ouacha 2005, Hubenthal 2009b]. The great advantage provided by bottom-up techniques is the fact that they can be applied in gas phase, in solution, on substrates and in matrices. During the past few years, mass production of metal NPs by means of bottom-up techniques has become feasible due to laser ablation and advanced wet chemical techniques.

Gas-phase synthesis One of the first secure bottom-up techniques of NPs preparing was gas-phase synthesis. In short, a gas of the desired material is created and expanded in a cooler atmosphere filled with an inert gas at reduced temperature. Because of adiabatic expansion and collisions with the inert gas atoms, the metal atoms thermalize and start to condensate. The vaporization of the required material is achieved typically by simple resistance heating, electron-beam evaporation, ion-beam sputtering, electric discharge or laser evaporation. Depending on the preparation technique, one distinguishes:

- adiabatic expansion of a supersonic jet,

- gas condensation due to evaporation in a cold gas atmosphere, and

- laser evaporation or erosion processes.

The size as well as the size distribution of the NPs in adiabatic expansion of a supersonic jet obtained can be determined by the preparation parameters. Several scaling laws can be found in [Hagena 1981]. In general, adiabatic expansion of a supersonic jet has two major limitations. First, it is suitable only for materials where the required high vapor pressure is achieved easily. Second, the metal gas itself acts as a heat bath, merging the binding energy. As a consequence, the size of NPs generated in supersonic jet is limited to radii typically below R=0.5 nm. The last limitation can be overcome by utilizing an inert seed gas that coexpands with the metal gas [Kappes 1982]. It has a typical pressure of 10^6 Pa, while the metal vapor pressure is reduced to an order of 10^4 Pa. Together with its role as a heat bath, the inert gas also influences the final size of the generated NPs. Generally, the heavier the seed atoms, the larger the metal NPs, because heavier atoms can take up more energy. For example the doubling of the size of the deposited NPs (from R=1 nm to R=2 nm) takes place when instead of argon as a seed gas xenon is used [Hilger 2001]. Meanwhile, the NPs size are still constrained to the lower nanometer range.

Gas condensation Aforementioned limit of the gas-phase synthesis can be successfully overcome by means of gas-condensation technique which dates back to the early 1950s [Kimoto 1953] and let the relatively large NPs with sizes in the several 10 nm range to be easily obtained [Pedersen 2007]. Apart of its simplest case which is based on an evaporation of a metal in a vacuum chamber, filled with a small amount of a stationery inert gas, this approach is less well understood due to a number of interdependent parameters, such as temperature, pressure, gas velocity, pump speed, etc. influencing the NP growth.

Laser vaporization and erosion processes Being other commonly used methods to generate NPs in the gas phase, both possess own obvious advantages with respect to other techniques. Laser vaporization (which is distinguished from the laser ablation) became extensively popular, because intensive beams of NPs of virtually all high-melting materials can be generated in a very controlled manner. By means of inert gas pressure in the evaporation chamber it is possible to tune the size of the NPs. So far as at high gas pressures the supersaturated vapor in the plume expands slowly and preserves the condition of supersaturation longer. As a result, larger NPs are generated. However, in the case of the slow expansion of the plume, fractal or web-like agglomerates (see Figure 3.9) may form [Li 1998].
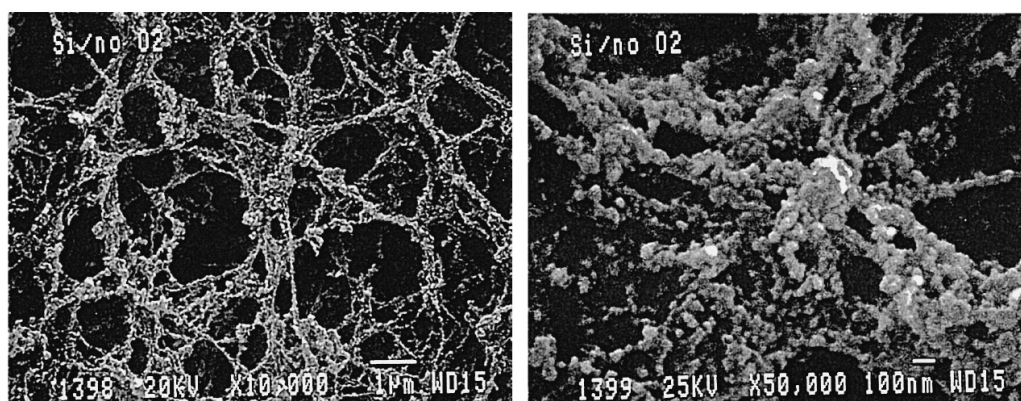
Figure 3.9: SEM micrographs of the weblike agglomeration of the silicon nanocrystals from ref. [Li 1998].

Production type	Used for	Nanoparticle generation by
Adiabatic expansion by a supersonic jet	Gases, liquids and solids with low melting point	Adiabatic expansion, partly with seed beam
Gas condensation	Materials that can be evaporated or sputtered	Streaming cold inert gas
Laser evaporation and e rosion techniques	All solid materials	Adiabatic expansion, partly combined with supersonic jet or gas condensation

Table 3.1: Characteristics of the three types of nanoparticle generation by gas-phase synthesis

On the contrary, at low inert gas pressures, the plume expands rapidly in the environment, got accompanied by a quick decrease of the density of the ablated atoms in the plume, with subsequent formation of smaller NPs. The last, being rather powerful process, creates very hot NPs, which in turn cool down by evaporation of surface atoms and collisions with the inert gas. Similar processes take place during surface erosion by means of heavy ion bombardment. The advantage of the ion-beam erosion is that it works with all solids and liquids [Magnera 1990]. Both laser vaporization and the erosion techniques can be combined with supersonic jet or gas condensation sources.

Obviously, that the main advantage of all gas-phase synthesis techniques is that the chemically pure NPs without any influences of eventually reactive environment can be obtained. However, for real-world applications, NPs on a support are desired. The easiest way to deposit NPs from the gas phase is placing a substrate in the NP beam. Unfortunately, the impact of the surface causes the deformation of NPs, thus revealing the drawback of the method. Computer simulations and experiments demonstrate that NPs generated by a supersonic jet, possessing typical velocities in the range of 10^4 m s^{-1} (corresponding to a kinetic energy of E_{kin}=1 eV per atom), as well as the substrate undergo an essential deformation. As works [Palomba 2008, Gracia-Pinilla 2009] demonstrate that the so-called soft landing with kinetic energies below E_{kin}=0.1 eV per atom is necessary to avoid a strong nanoparticle deformation and surface damages.

Another variant for soft landing is known - preadsorption of a liquid noble gas layer on a cooled substrate before NP deposition [Cheng 1994]. Gas layer, acting as an airbag, effectively dissipates the kinetic energy of the NPs without changing their morphology [Bromann 1997]. In this case the kinetic energy of high-energetic NP can be reduced below E_{kin}=0.01 eV per atom, which warranties a soft landing. But, it has to be taken into account that in the case of soft landing, the NPs will be deformed slightly because of the contact with the substrate, namely surface tension effects. Another noticeable advantage of gas-phase synthesis is that a stream of a reactive gas can also be added during the NP growth and oxides, fluorides and so on can be easily generated. But, due to the statistical growth process, a broad size distribution results. Separation techniques addressing the issue of the NP ensembles with a narrow size distribution in the beam are applied due to the hampering of determination of the properties of single NP sizes. So, being determined by NPs' size and its charge state, different methods available: mass separation techniques [Binns 2001], crossing the helium and cluster beams (thanks to the dependence of the scattering angle of the clusters on its size, but limited to small clusters), size-dependent velocity slip between the inert gas and inert NPs during the expansion [Broyer 1987].

Vapor deposition technique Vapor deposition techniques are applied to prepare NPs

on substrates under ultrahigh vacuum conditions. In general, three growth scenarios are possible:

- Volmer-Weber or island growth;

- Frank-van der Merwe or layer-by-layer growth, and

- Stranski-Krastanow or layer with subsequent island growth.

The Volmer-Weber growth is the usual growth mode for metal NPs on dielectric substrates [Henry 1998, Bäumer 1999], the further exposition will be concentrated solely to the first type of growth. As known, the nanoparticle growth on a substrate is a process far from thermodynamic equilibrium. The kinetics of growth is prevalent with respect to thermodynamics in terms of the final nanoparticle morphology. As a result of the growth kinetics in the Volmer-Weber growth, the shape of the NPs is strongly correlated to their size [Wenzel 1999, Ouacha 2005]. Starting from NPs with $R_{eq} = 1$ nm, which are nearly spherical, up to more oblate with increasing R_{eq} [Hubenthal 2009b]. Consequently, the LSPPR of NPs grown on substrates by deposition of atoms and subsequent nucleation is shifted to lower photon energies, if the NPs increase in size [Nilius 2001a, Gonzalo 2003]. This situation is depicted in Figure 3.10.
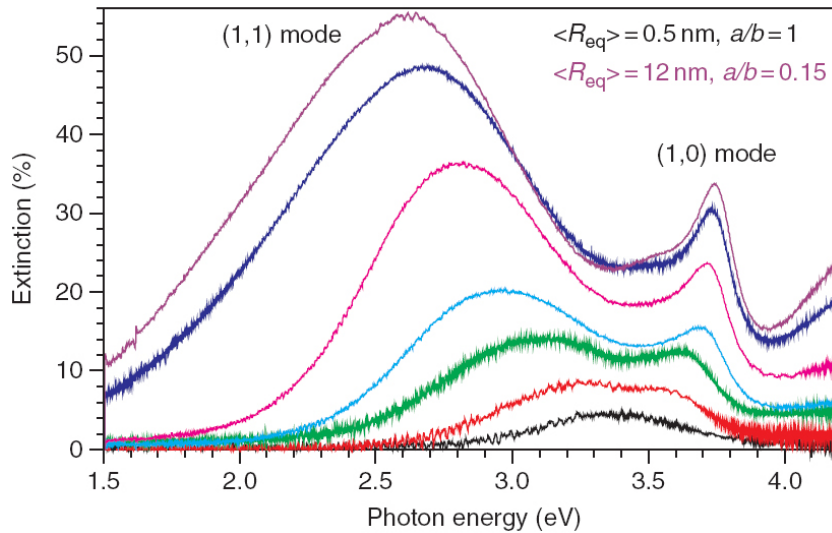
Figure 3.10: Optical spectra of silver NPs with different sizes on quartz substrate. A clear shift of both modes is observed. The shift and increase of the extinction of the (1,1) mode are less pronounced due to the influence of the interband transition, which damps the (1,1) mode.

It is worth-noting that in case of gold and silver atoms deposited at room temperature on ideal defect-free dielectric substrates, an essential redesorption rate is expected [Campbell 1997], and the sticking coefficient, defining the amount of nucleated atoms normalized to the amount of deposited atoms, is significantly smaller than unity. On the contrary, real dielectric substrates possess defect densities in the order of 10^{12} to 10^{14} defects cm^{-2} and the sticking coefficient is close to the unity [Henry 1998].

The issue of great importance for the Volmer-Weber growth that the impinging atoms have a low kinetic energy. Otherwise the implantation of the atoms or sputtering of the

substrate may occur [Gonzalo 2005]. Both are the obstacles for the Volmer-Weber growth, due do the prevention of the diffusion and subsequent nucleation of atoms at the surface. To guarantee a diffusion of the atoms on the substrate surface, usually thermal atoms from the gas phase are adsorbed in the surface [Nilius 2001b, Benten 2005].

Thus, there are several generation techniques for a low energetic atom beam are available [Seal 2003, Guo 2003, Drachev 2004, Ouacha 2005]. Due to the statistical growth behavior, the Volmer-Weber growth results in NP ensembles with a broad Gaussian size and shape distribution with typical widths between $\sigma=25\%$ and $\sigma=40\%$ [Ouacha 2005, Resta 2006], see Figure 3.11.
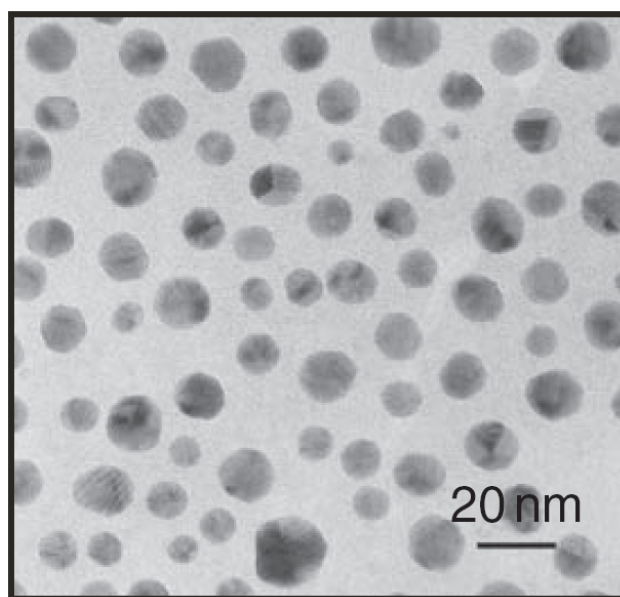
Figure 3.11: TEM image of gold NPs with a mean equivalent radius of $\langle R_{eq}\rangle=(4.7\pm1.3)$nm grown by the Volmer-Weber on a sapphire substrate. In the present case, the width of Gaussian size distribution amounts to $\sigma = 27\%$.

As for the above-mentioned techniques, a broad size and shape distribution is an obvious drawback for nearly all applications. Overcoming of this lack of order is based on selective laser tailoring processes. In brief, laser light with a given photon energy is absorbed only by NPs whose LSPPR coincides with this photon energy. After absorbed light is rapidly converted into heat, causing the diffusion and evaporation of surface atoms. This selective heating is exploited to tailor either the size or a shape of NPs [Stietz 2001, Ouacha 2005]. Whereas, size-tayloring of NPs on the substrates is based on a post-grown selective heating of certain (undesired) NPs in an ensemble via their LSPPR [Safonov 1998, Bosbach 1999] fulfilling the relation R≪λ; meanwhile shape-tayloring of supported NPs is achieved by irradiating the NPs during their growth (laser-assisted growth). The core of mechanism is the photon energy of the laser acting as a barrier for the LSPPR. The light adsorbed causes a temperature rise in the NPs and stimulates mainly self-diffusion but also desorption of atoms from the edges and perimeters of the particles. Both effects lead to a shape change of the NPs toward more spherical. Consequently, the heat-induced reshaping of the NPs toward more spherical competes with the decrease of the axial ratio due to the

frown kinetics. In case of appropriately chosen fluence, the two competing processes are balanced. Finally, by varying the photon energy of the laser light, different axial ratios can be stabilized [Ouacha 2005, Hubenthal 2009b].

The essential advantage of laser tailoring is that it is a self-regulating process. The interaction between the NP and the laser light proceeds only until the LSPPR of the NPs does not coincide with the photon energy of the laser light anymore [Hubenthal 2009b].

Photochemical synthesis Apart the above wet chemical preparation technique photoinduced processes have also represent the issue of increasing interest (see Figure 3.14). These processes can be either photochemical or photophysical. The last one is also known as laser ablation and will be discussed further. Photochemical synthesis is based on the formation of neutral atoms M^0 under conditions that are not suitable for their precipitation.
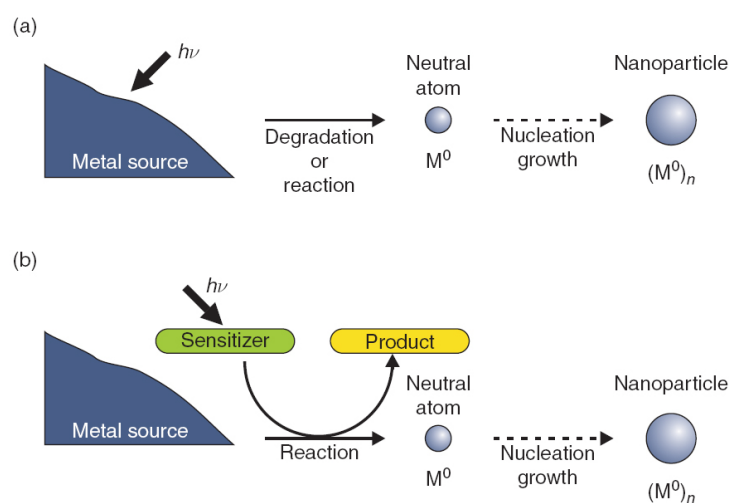
Figure 3.12: Sketch of the two routes for photochemical synthesis: a) direct photolysis and b)photosensitization.

Irradiation light, which can be used to initiate the precipitation, provides the couple of mechanisms, namely direct photosynthesis [Hada 1976, Huang 1996] and photosensitization [Kapoor 2003, Esumi 2005, Scaiano 2006]. While the first one uses the formation of neutral atoms directly from a metal salt or complex, thus being free of reducing agent and not limited to NPs in solution; the second is a faster and more efficient for a photochemical synthesis of metal NPs in solution due to a sensitizer used as the reduction process promoter.

Sol-gel technique The principle idea of this method is to generate NPs in a solution and add this solution to a gel that transforms after several synthesis steps in a solid state. Aging process, following the precursors mixing and gelation process, depending on the exact conditions may last several minutes up to several days [Cushing 2004, Scaiano 2006]. In addition, growth of the NPs in the gel is due to Oswald ripening[1]. The final step is the drying of the gel during which the reactive groups of touching gel particles condensate. Afterward, the gel has to be dehydrated and stabilized against rehydration. The advantage of the technique is that NPs in a matrix can be generated easily and that these NPs are well protected against the environment. The main limitation, concerning applications with

---

[1]In the gel, usually NPs with different sizes exist. Since larger particles are energetically more favored than smaller ones, a growth of the larger NPs takes place, drawing material from the smaller NPs which shrink can occur. This process is known as Oswald ripening

respect to surface-enhanced spectroscopies, is the broad size distribution, since not all NPs are in resonance with an exciting laser wavelength. Furthermore, only a small fraction of the NPs is close enough to the film surface, such that their field enhancement ranges outside the sample and can be used for surface-enhanced spectroscopies.

Pulsed laser ablation Pulsed laser ablation is a versatile method for a mass production of metal NPs in a size range between a few nanometers and 100 nm. The production rate is enormous and for NPs in solution is in the order of several micrograms per second. A particular advantage of the technique is that no chemical reactants are needed, although they can be added to control the size as well as the size distribution of NPs in solution [Amendola 2006, Barcikowski 2007, Zeng 2012]. Thus, the prepared material is free of toxic impurities, which contrasts with standard wet chemical processes, where usually toxic reactants are involved. Moreover, the synthesis in pure water promises the benefit for medical applications. The main drawback is the extremely broad size distribution of the NPs generated and, compared to gas-phase or vapor-deposition technique, the less well controlled synthesis of NPs.

Flame spraying

Flame spraying is another technique allowing a mass production of metal NPs without any toxic impurities. Production rates of several milligrams per second are usual [Keskinen 2007]. The base of this technique is an evaporation (T=3000 K) [Mäkelä 2004, Keskinen 2007]) and decomposition of a liquid precursor containing the metal species, usually a metal salt (see Figure 3.13).
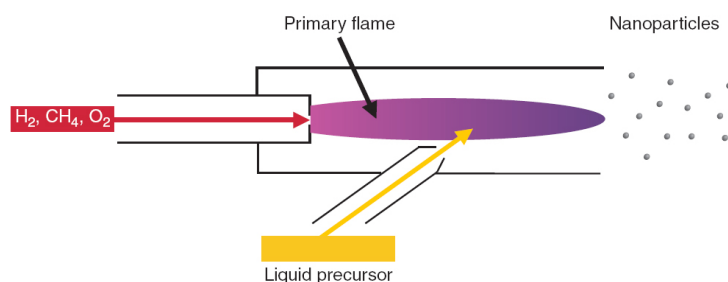
Figure 3.13: Principle of nanoparticle generation by means of flame spraying.

The most critical parameter in this process is the flame stability. Thus, only a stable burning flame warrants a controlled and reproducible generation of NPs. The size of the generated NPs is determined by a variety of parameters [Keskinen 2007]:

- metal salt concentration;

- the precursor flow rate;

- the flame temperature;

- the environment;

- the distance from the torch head at which NPs are collected;

The last is advantageous when a variety of extinction maxima are desired and colloids are easily aggregated using an electrolyte solution (e.g., NaCl). Ag colloid aggregation is an important technique used for SMSERS. Moreover, these methods often require NP surface stabilizing or functional ligands that are not always necessary or beneficial [Erin B. Dickerson 2008].

3.4 BCP-based SERS substrates

3.4.1 BCP self-organization as the key feature for use in SERS

On the base of the aforementioned synthesis techniques analysis a detailed overview of the state-of-the-art in the field of Surface-Enhanced Raman Spectroscopy (SERS) and, in particular, SERS-substrates synthesis. Due to the specificity of the object of our interest it has been decided to concentrate on the recepies for SERS-substrates production, that combine both the simplicity and high-yield of bottom-up techniques with the spatial ordering of the top-down techniques. Thus, finally the optimal solution developed was based on block-copolymers self-assembly nanostructures. And there's further optimization in correspondence to our application, became the key component that lead to a successful application of the SERS-substrates (as it will be demonstrated in Experimental section).

In the coarse of development of high-performance plasmonic substrates for imaging and bio(chemical) sensing applications, it is equally important to provide strong signal enhancement and reproducibility. In particular in SERS, insufficient reproducibility has long been a major obstacle for the application of this analytical method in critical sensing applications [Yan 2011].

As it has been shown before, when the reproducibility and the spatial ordering of the SERS-substrate is of primary importance high resolution electron beam or focused ion beam are not well-suited for large areas, thus, alternative strategies are required. In this sense self-assembly techniques are attractive because of their highly parallel nature and enabling of large-scale patterning rapidly and at very low costs. The flexibility of the technique extends the use from highly-ordered nanostructures over large surface areas [Park 2008b, Park 2008a] to generation metal NPs [Zhang 2006] and structured metal surfaces [Lu 2006, Wang 2009].

Self-organization is a powerful route to the "bottom-up" fabrication of nanostructures. The ability of soft materials such as block copolymers to form a rich variety of nanoscale periodic patterns offers the potential to fabricate high-density arrays for use in different applications [Hamley 2003, Segalman 2005]. The formed self-assembled patterns are considered both as nanolithographic masks and templates for the further synthesis of inorganic or organic structures. Novel applications in fuel cells [Guo 2011], batteries [Young 2014] and optoelectronic devices [Segalman 2009, Botiz 2010] rely on the inherent properties of the blocks. All of these appliances depend on the extremely regular self-assembly of block copolymers over macroscopic distances.

Block copolymers have received significant attention over the last few decades because of their ability to self-assembly in the nanometer length scale [Hamley 1998, Hamley 2003]. This self-assembly is caused by both the incompatibility of the two polymer blocks and their covalent connectivity.

Block-copolymers are generally defined as macromolecules containing two or more polymer chains that are bound together through covalent bonds. The simplest block copolymer is the diblock copolymer, which consist of two different polymer chains covalently attached at their ends. In the melt, they are undergo segregation into a variety of ordered structures due to repulsion of the immiscible blocks, much as in the case of a blend of immiscible homopolymers. More sophisticated compositions include triblock copolymers and mixed arm block copolymers, where more than three polymer chains are covalently attached at a common branching point. In the case of a blend of two homopolymers, A and B, phase behavior may be controlled by three experimental parameters: the degree of polymerization (N), the composition (f), and the A-B Flory-Huggins interaction parameter (χ). The Flory-Huggins equation describes approximately how these parameters affect the free energy of a blend:

$$\frac{\Delta G_{mix}}{k_b T} = \frac{1}{N_A}ln(f_A) + \frac{1}{N_B}ln(f_B) + f_A f_B \chi \tag{3.3}$$

the first two terms correspond to the configurational entropy of the system, and can be regulated via polymerization chemistry to change the relative lengths of the chains and fractions of A versus B polymer. In the third therm of Eq: FH, χ is associated with the non-ideal penalty of A-B monomer contacts and is a function of both the chemistry of the molecules and temperature. In general,

$$\chi = \frac{a}{T} + b \tag{3.4}$$

Experimentally, χ can be controlled through temperature. Unlike macro-phase separation in blends, the connectivity of the blocks in block copolymers prevents complete separation and instead the diblock copolymer chains organize to put the A and B portions on opposite sides of an interface. The equilibrium nanodomain structure must minimize unfavorable A-B contact without over-stretching the blocks [Bates 1990]. The strength of segregation of the two blocks is proportional to χN. A symmetric diblock copolymer is predicted to disorder (or pass through its order-disorder temperature (ODT)) when $\chi N < 10$. Below the ODT and when the volume fraction of block A (f_A) is quite small, it forms sphere in a body-centered cubic (BCC) lattice surrounded by a matrix of B. As f_A is increased towards 0.5, the minority nanodomains will form first cylinders in a hexagonal lattice, then bicontinuous double gyroid structure, and finally lamellae.

The size and periodicity of the nanodomains are also functions of the polymer size (N) and the segmental interactions (χ). Block copolymers with $\chi N \gg 10$ microphase separate above their glass transition temperature, The resulting morphology depends largely on the relative volume fraction of the components. Some of the more commonly seen morphologies are lamellae, cylinders and spheres:

The length of the polymer chain is the determinative for the length scale of microdomains. The thermodynamics of the structures have been extensively examined in bulk, and more recently, in thin films [Harrison 2004]. Establishing the relationships between different block copolymer phase diagrams and facilitating the comparison with theory, requires to specify parameters in addition to χN and f.

First, asymmetry of the copolymer conformation breaks the symmetry of the phase diagram about f=0.5. In case of AB diblocks, conformational asymmetry is quantified using the "asymmetry parameter" $\varepsilon = (b^2{}_A/\nu_A)/b^2_B/\nu_B$ [Helfand 1975b, Bates 1994], where b_J is the segment length for block J and ν_J is the segment volume. The phase diagram is influenced by composition fluctuations also, and this has been taken into account for theoretically via the Ginzburg parameter $\bar{N}=Nb^6\rho^2$, where ρ is the number density of chains [Helfand 1975a, Fredrickson 1989]. The extent of segregation of block copolymers depends on the magnitude of χN. For small χN, close to the order-disorder transition (up to χN=12 for symmetric diblocks for which χN_{ODT})=10.495), the composition profile (density of either component) is approximately sinusoidal. This case is named the weak-segregation limit. At much larger values of $\chi N (\chi N > \tilde{} 100)$, the components are strongly segregated and each domain is almost pure, with a narrow interphase between them. This is the strong-segregation limit.

Block copolymer thin films are of particular interest due to the possibility of obtaining two-dimensional patterns with very high registry and regularity [Segalman 2005]. In particular, they provide access to a length scale that is not available to traditional lithographic techniques.

In general, the applications of block copolymers in analogy to plasmon structure synthesis can be divided into two categories: top-down and bottom-up techniques. Where the
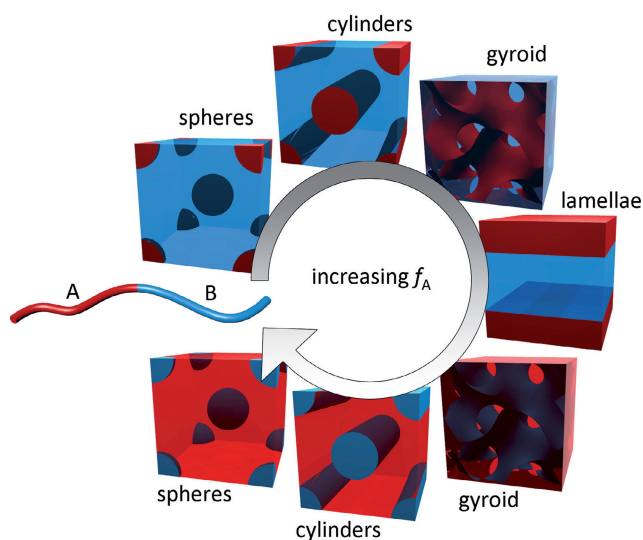
Figure 3.14: Different phases formed by self-assembly of coil-coil diblock copolymers in the bulk (when the intermolecular interaction is sufficiently large) as a function of the volume fraction of one of the blocks (f_A). Other phases have also been reported for diblocks, and the phase diagrams of BCPs containing more than two blocks are considerably more complex. Switching out one or both coil blocks with a conjugated block that adopts a semi-flexible or rigid rod structure will also qualitatively change this phase diagram.

first kind refers to the traditional methods of the semiconductor industry in which pattern transfer from the block copolymer is used to pattern an underlying substrate. In bottom-up techniques, the active components are directly self-assembled.

sIntroducing the work [Lee 2011] authors specify, that each fabrication method for SERS substrates is a compromise between enhancement factor, cost, active area, reproducibility, and service life [Dick 2002, Natan 2006]. Being guided by these considerations it was underlined that the method based on the block-copolymer self-assembly satisfy all the requirements listed. In particular, essential attention was paid to the tunability of the plasmon resonance, thus permitting maximizing of the enhancement factor in terms of specificity of the Raman instrument (laser wavelength) and analyte. In addition, the substrates are providing the reproducible EF over macroscopic sampling areas. The attributes taken together promoting the fabrication process to appeal for mass production. Therefore, the self-assembly of block copolymes promotes complex surface structures with nanoscale features whose patterning depends on the tunable enthalpic and steric interactions between polymers, as well as with the solid interface [Morkved 1996, Park 1997, Rockford 1999]. One of the most efficient chemical strategies for the assembly of well-spaced and ordered nanoparticle arrays on solid surfaces has been developed by Spatz and colleagues [Glass 2003] and has been called "Block Copolymer Micelle Nanolithography" (BCML). Detalizing the synthesis procedure [Spatz 1996, Spatz 2002], authors specify, that the accuracy of the position of the dot in the center of the micelle may be as precise as the size of the particle itself [Spatz 2002], fairly naming this method as "A Combined Top-Down/Bottom-Up Approach" to the Microscopic Localization of Metallic Nanodots", hence, addressing the issue of the appropriate valuable scales for SERS, namely down to sub-10 nm [Tseng 2005, Abu Hatab 2008].

3.5 Conclusion

Finally, as it has been demonstrated, the block-copolymer self-assembly based SERS-substrates represents an optimal solution both in terms of sufficient enhancement provided and long-range order. Combination of both factors let us to pick out this approach and use it as the base one.

Experimental part

In the Chapter the details of the chemical protocol followed for our SERS-substrates synthesis will be discussed. Moreover, all the techniques employed for their characterization will be briefly described both in terms of theoretical and experimental aspects.

4.1 SERS-substrates synthesis

4.1.1 Materials

Polysterene-*block*-poly-4-vinylpyridine (PS-b-P4VP) copolymer (Polymer Source Inc., Dorval, Canada) with molecular weights of PS M_n=10.400 g· mol^{-1} and P4VP M_n=19.200 g· mol^{-1} correspondingly, with polydispersity index 1.27 without further purification. Tris(4-(dimethylamino)phenyl) methylium chloride (Crystal Violet dye), and dye rhodamine 6G (R6G) were purchased from Sigma Aldrich as well as toluene, tetrahydrofuran (THF), silver nitrate (AgNO$_3$) and sodium borohydride (NaBH$_4$).

4.1.2 Substrate synthesis

The fabrication of SERS substrates was based on partially modified procedure described in [Cho 2012] for silicon-based and glass-based ones aiming to improve the nano-coating spatial uniformity in accordance with our applications. With particular attention towards the glass-based ones due to the back-scattering configuration used in all measurements. The synthesis of the substrates consists of the following steps (see also Figure 4.1):

1. the formation of the PS-b-P4VP crew-cut micelles solution;

2. the incorporation of the silver precursor (silver ions) into the P4VP micelle core;

3. the reduction of the coordinated silver ions to silver NPs;

4. centrifugation and phase separation of the solution (original step);

5. spin-coating of the solution on the silicon and glass substrates;

6. polymer removing by UV-light exposure.

Further the detailed description of the synthesis procedure is provided. Due to the fact that the recipe used in the work based on the use of crew-cut micelles, which are known as hardly obtainable, the specific solution needed to be used. Namely, the combined use of toluene and THF as the last is the selective solvent of PS block and favors to facilitate the easy and stable formation of the P4VP micelles. Thus, crew-cut micelles solution was based on the a mixture of THF (7.0g) and toluene (10.5g) (i.e. ratio 0.67 w/w), with a total volume of 20 ml and PS-b-P4VP (94.5mg) in relative concentration of 0.54% w/w under stirring at 700 rpm for 3h at 25°C, then for 2h at 67°C, before slowly cooling down the solution at room temperature. After the micelles were loaded via coordination complex
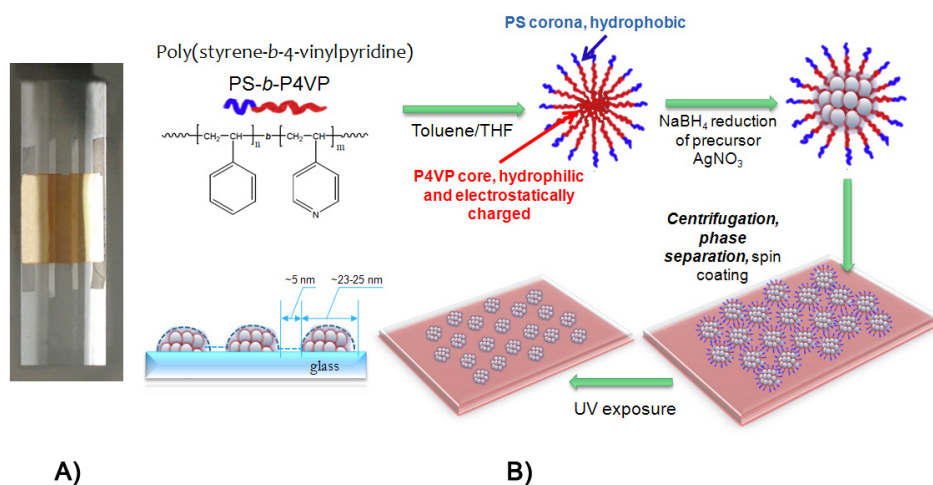
Figure 4.1: A) Plasmonic substrate, on-glass-coated, showed a green glow in backscattering at ambient light; B) General scheme for substrate synthesis.

of the P4VP core with Ag^+ starting from 198 mg of $AgNO_3$, in molar ratio 2 : 1 with the former, upon stirring (700 rpm) for 24 hours. Note, that the excess of material was filtered with 200-nm PTFE syringe filters before the reduction procedure.

Experiment shown, that the amount of the reduction agent $NaBH_4$ affected dramatically the quality of the metal-micelle nanocomposite suspension. The silver in micelles, as was determined experimentally, is best reduced by 30 mg of fine dry powder of $NaBH_4$ (dissolved in controlled atmosphere with low humidity) by stirring for 24 h. The matter of crucial importance was the filtering of the reduced black solution (precipitated non-coordinated silver ions) finally reached with 200-nm PTFE syringe filters to restore a large aggregates-free solution. The final, perfectly limpid, solution was centrifuged at 11 krpm for 20 min to separate the possible unloaded supernatant micelles. In a 1-ml eppendorf, the volume of supernatant removed came to 300 μl. This leaved more concentrated solution of nanocomposite micelles (equivalent to an initial copolymer of 0.77% w/w). The remaining solution was sonicated for 22 min.

Before the spin-coating process synthesis, microscope coverslips and silicon wafers were previously pretreated according the following procedure: soaking into ultrasonic bath (UB) for 22 min at $60°C$ in acetone and then in milli-Q water solution with sonic bath soap (3 w/w), then rinsing first with milli-Q water in UB, and then again with isopropanol (same procedure); finally they were dried with nitrogen pump.

A volume of 100 μl was left over the supporting glass for 30s before starting the spin-coating at 1.0 krpm speed for 60s, in controlled ambient atmosphere. This allowed to achieve an extremely uniform film coating with nanodomain gap < 5 nm (as will be shown later). The film, thanks to the self-assembly, consisted of a spatially invariant high density lattice of nanodomains characterized, because of micelle nucleation, by silver NPs' (Ag-NPs) clusters limited in size-dispersion.

Finally, UV exposure at 254 nm (Hg lamp Sankyo Denki G15T8) at a sample distance of 6 cm with energy density of 1.7 mJ/cm^2 (for the details see Figure 4.2), for 24h, removed the copolymer. The achieved reddish plasmonic film on glass appeared as a transparent optical coating with a green backscattering glow. Note, that the film homogeneity and

adhesion resulted unaffected when soaking into solutions of water, methanol, ethanol and acetone, thus demonstrating the high quality of the adhesion between silver nanoclusters and substrate surface.
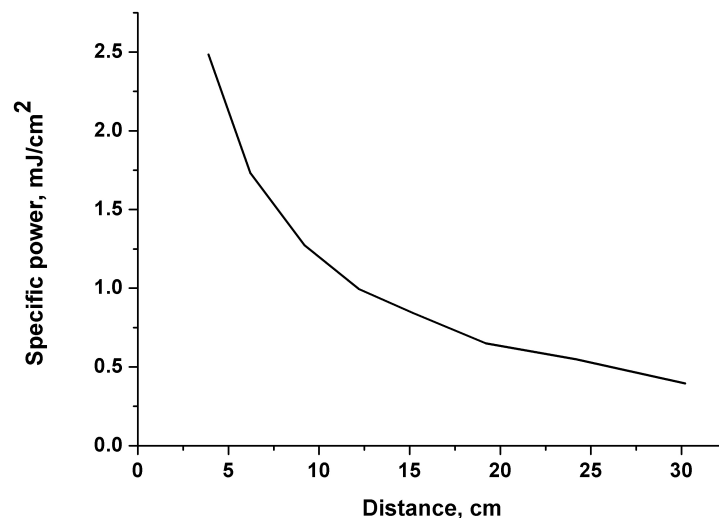
Figure 4.2: Specific power/distance dependence of Hg lamp Sankyo Denki G15T8.

4.2 Experimental techniques and instruments

4.2.1 Raman spectrometer

In this work the Witec alpha300 system has been used (see Figure 4.3). The system characterized by combination of its Raman capability and a highly efficient Raman spectrometer with a high resolution confocal optical microscope. This complex provides not only a Raman spectrum acquisition but also to combine this chemical information with a lateral resolution in the sub-micrometer regime. Using green excitation light, resolution down to 220 nm is possible. The microscope, as well as the spectrometer and the detectors are optimized for the highest throughput and efficiency which gives to the instrument an unrivalled sensitivity. In the system, the laser light is delivered through a single-mode optical fiber. This type of fiber supports only a single transversal mode (LP_{01}, Gaussian beam) which can be focused to a diffraction-limited spot. The reflected (Raman scattered) light is collected with the same objective and is focused into a multi-mode fiber, which directs the beam to a spectrometer equipped with a CCD camera (see Figure 4.3).

Using the Witec alpha300 system with its Raman capability, a variety of Raman modes are possible:

- **Collection of Raman spectra at selected sample areas (Single spectrum)**: Single Raman spectra can be collected at user-selectable sample areas with integration times ranging from a few ms to hours. The position of the collected spectrum can be fully controlled in 3D. The microscope Z stage (the focusing stage) has a step size of 10 nm, while the capacitively controlled piezo-stage has a positioning accuracy of only 3 nm in the lateral directions. This ensures that the point of interest will remain fixed under the excitation focus. This issue is of crucial importance especially when
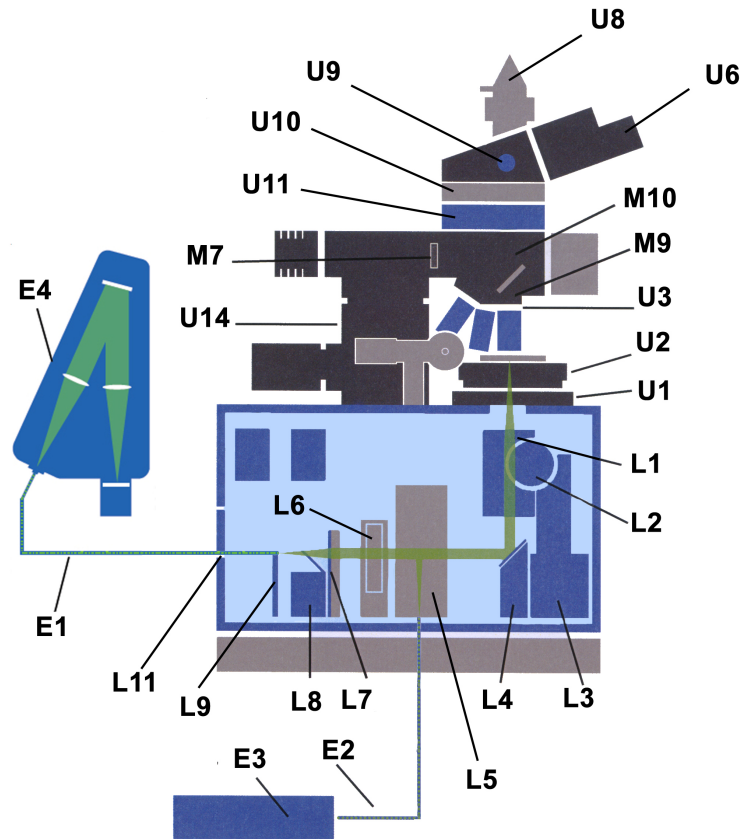
Figure 4.3: Schematic illustration of the beam path for confocal Raman microscopy. U1-XY positioner; U2-Scan stage; U3-objective tarret with objectives; U6-Binocular tube with ocular camera; U8-Fiber coupling unit optical output; U9-Pushrod; U10-Filter slider unit; U11-Laser coupling unit optical unit; U14-Microscope Z-stage with stepper motor; M9-objective turret; M10-reflector slider; E1-Multi-mode optical fiber; E2-Single-mode optical fiber; E3-Laser; E4-Spectrometer; L1-collection objective of the inverted microscope; L2-manual adjustment knob for the L Position of the inverted microscope; L3 - Motorized X,Y,Z positioning unit of the inverted microscope; L4 - Deflection mirror; L5 - Laser coupling unit optical input for Raman or confocal measurements with excitation from below; L6 - Filter wheel; L7 - Tube lens (position adjustable version optional); L8 - Flip mirror; L9 -SMA fiber connector; L11 - FC fiber feedthough for Raman or confocal measurements with excitation from below.

spectra with longer integration times for the best quality and signal to noise ratio are to be obtained from extremely small sample volumes.

- **Collection of time series of Raman spectra at selected sample areas:** Time series of Raman spectra can be obtained to analyze dynamic sample properties. Time series of thousands of spectra can be obtained and analyzed with integration times ranging from a few ms to tens of seconds.

- **Raman spectral imaging:** This is the most versatile mode of the alpha300 system with its Raman capability. In this mode, complete spectra are obtained at every image pixel. Images with a size of 512×512(=262144 spectra) or even more (limited only by the computer memory) can be acquired. During data acquisition, images can be calculated from the spectra by applying a large number of analyzing modes, such as integrating over certain areas, calculating the peak position or determining the peak width etc. in the spectra. As each spectrum is a fingerprint of the chemical species at a specific image point, the distribution of different materials or local properties of the same material (like crystallinity, and local stress) can be analyzed in 3D and with a spatial resolution down to 200 nm.

- **Collection of Raman spectra along a selected line (Line Spectrum):** If only the distribution along a certain line in a sample is of interest (cross section, depth profile etc.), Raman spectra can be obtained along a user selected line in three dimensional space. This sufficiently reduces the number of spectra compared to the spectral imaging mode and allows longer integration times per spectrum.

Confocal Raman microscopy Confocal microscopy uses a point source (usually laser), focused onto the sample. The reflected light (Raman, fluorescence) is collected with the same objective and focused through a pinhole at the front of the detector (see Figure 4.4. This guarantees that only light from the image focal plane can reach the detector, which greatly increases image contrast and with the proper selection of pinhole size, slightly increases resolution (maximum gain in resolution: factor $\sqrt{2}$).

The enhancement of image contrast and depth resolution for Raman microscopy is extremely important. Meanwhile an enhancement of the lateral resolution in confocal microscopy requires extremely small pinhole diameters and will therefore decrease the detection efficiency to a level usually unacceptable in most experiments (see Figure 4.5).

Pinhole size The size of the pinhole, in optical coordinates, should not exceed v_{Pmax}=2.5. This will avoid the loss in depth resolution. To obtain the highest lateral resolution, the pinhole size should be below v_{Pmax}=0.5.

In practice, the pinhole size can be up to v_{Pmax}=4 without significantly changing depth resolution and up to v_{Pmax}=2 without significantly changing lateral resolution. In case v_{Pmax}>4 at least the resolution of a conventional microscope remains. This is due to the fact that for a large detector the resolution is always determined by the diameter of the exciting laser spot. Only the depth resolution (and therefore contrast for a thick sample) is lost in this case.

For the experiment, the relation

$$\frac{M}{NA} \geq \frac{\pi d_0}{v_{Pmax}\lambda} \tag{4.1}$$

must be fulfilled, where M is the magnification, d_0 the diameter of the pinhole and NA the numerical aperture of the objective. The left side of this equation is defined by the objective and the beam path. In Table 4.1, the parameter $\frac{M}{NA}$ is calculated for several typical objectives.
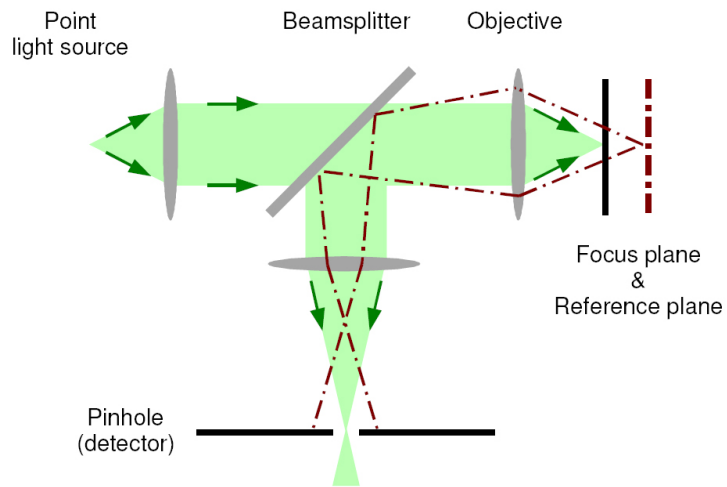
Figure 4.4: Principle setup of a confocal microscope.
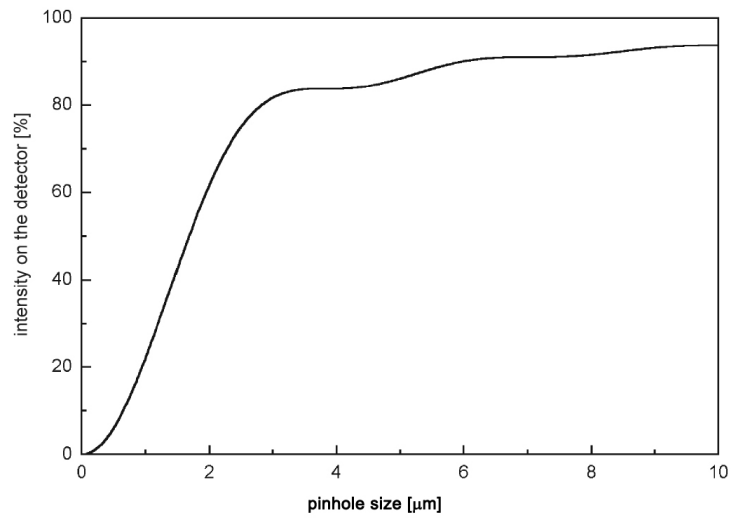
Figure 4.5: Collection efficiency as a function of pinhole size normalized to the total power in the image plane.

objective	10/0.25	20/0.4	40/0.6	60/0.8	100/0.9	100/1.25	100/1.4
M/NA	53	50	67	75	111	80	71

Table 4.1: M/NA for different objectives.

wavelength (nm)	440	488	532	633	785
d_0=10μm	29	26	24	20	16
d_0=25μm	71	64	59	50	40
d_0=50μm	142	129	118	99	80
d_0=100μm	286	258	236	199	160
d_0=200μm	571	515	472	397	320

Table 4.2: $\frac{\pi d_0}{2.5\alpha}$ for typical wavelengths and pinhole sizes.

The right side of Equation 4.1 is defined by the wavelength and the pinhole size itself Table 4.2.

In actual experiments, as the matter of fact, it is necessary to find a compromise between the highest resolution and collection efficiency. This fact acquires additional importance in case of Raman microscopy due to the extreme weakness of the effect.

4.2.2 Description of characterization techniques

4.2.2.1 Dynamic light scattering

(DLS) is also known as photon correlation spectroscopy (PCS) or quasi-elastic light scattering (QELS). The nutshell of the technique is the measurement of the temporal fluctuations of the intensity of scattered light. The numbers of photons entering a detector are recorded and analyzed by a digital correlator. The separation in time between photon countings is the correlation time, t. The autocorrelation function of the intensity at an angle θ, I_θ is computed as

$$g(t) = \lim_{S \to 0} \left[\frac{1}{s} \int_0^S I_\theta(S) I_\theta(s+t) ds \right]. \tag{4.2}$$

Laplace transformation of Equation 4.2 yields the distribution of relaxation times, $A(\tau)$. The decay rates of the relaxation modes provide translational diffusion coefficients.

In polymer solutions, DLS is used to determine the hydrodynamic radius of the constituent particles using the Stokes-Einstein equation:

$$R_H = k_B T / 6\pi\eta D, \tag{4.3}$$

where k_B is the Boltzmann constant, T is the absolute temperature, η is the solvent viscosity and D is the diffusion coefficient. DLS has largely been exploited to study diffusion in polymer solutions. DLS also has been used to investigate relaxation modes in block-copolymer melts, and the effects of the entanglements on diffusion. Because the intensity of scattered light is z-weighted ($z \propto c M_w$ where c=mass concentration and M_w=mass-average molar mass), DLS in sensitive to low levels of high-molar-mass solutes.

4.2.2.2 Small-angle X-ray scattering

The technique is ideal for the investigation of morphology or ordered phases in block-copolymer melts, solids and gels because length-scales are probed which are typical of those of block-copolymer microstructures, i.e. 1-100 nm. In contrast to transmission electron microscopy (TEM), the structure of the sample averaged over the macroscopic size of the beam is probed. Scattering data are presented as a function of the scattering vector q or its magnitude, where

$$q = |q| = \frac{4\pi \sin \theta}{\lambda}. \tag{4.4}$$

The relative positions of a sufficient number of reflections arising from microstructural periodicities enable unambiguous identification of morphology. Further information is obtainable by means of preparing oriented specimens, and obtaining diffraction patterns fro different orientations. For example, in an oriented lamellar phase with the beam incident parallel to the layers, Bragg reflections at q^*, $2q^*$, $3q^*$,..., where q^* is the position of the first-order reflection, are observed along a direction parallel to the layer normal.

Small-angle X-ray scattering (SAXS) is appropriate where the electron density contrast between blocks is sufficient for the polymer to diffract X-rays [Baltá-Calleja 1989]. This is often possible with an intense source of X-rays, such a rotating anode generator or a synchrotron source. The radius of gyration of block copolymer micelles in dilute solution can be obtained from SAXS measurements using the Guinier approximation [Guinier 2013]:

$$I(q) = I(0) \exp\left(-q^2 R_g^2 / 3\right) \tag{4.5}$$

This is valid for small scattering angles, $qR_g \ll 1$. Small-angle scattering intensity in the high angle (q) region can be analyzed to provide information on interface thickness (e.g. the lamellar interface thickness block in copolymer melts or core-corona interface widths in micelles). For a perfectly sharp interface, the scattered intensity in the Porod regime falls as q^{-4}[Svergun 2013]. For an interface of finite width this is modified to

$$I(q) \propto (S/V)q^{-4} \exp\left(-\sigma^2 q^2\right) \tag{4.6}$$

where S/V is the interfacial area per unit volume and σ is an interfacial width.

4.2.2.3 Atomic Force Microscopy

Atomic force microscopy (AFM) has been demonstrated to be an invaluable technique for characterization of nanoscale structures at the surface of block copolymer films. In this method, the deflection of a cantilever due to repulsive electronic interactions of an attached sharp tip with the surface is measured. The microscopic movement of the tip creates a force which is measured to provide an image of the surface structure. Both contact and tapping mode AFM have been employed for the investigation of surface topography, the latter avoiding contact of the tip with the surface. The morphology measured by means of AFM is a function of copolymer composition, temperature, film thickness and surface tension of the blocks.

Pioneering contact mode AFM studies by Meiners et al. [Meiners 1995] show that chemical sensitivity at the surface of thin polymer films can be achieved by measuring the microscopic friction and stiffness for glassy block copolymers. This provides invaluable information to complement topography on the nature of the block at the surface. Fundamentally the operation of an AFM is described by Lennard-Jones interaction between a microscopic particle and surface (see Figure 4.6).

The force, $F(z)$, depends on the potential, $U(z)$, by the relationship:

$$F(z) = -\nabla U(z) = -\frac{dU(z)}{dz} \tag{4.7}$$

Therefore in Fig. 4.6 can be distinguished two different regimes, separated by z_0, the distance corresponding to a stationary point of the potential, $U(z)$, and hence to $F(z_0) = 0$. For z values larger than z_0, the force will be repulsive. As the force is the derivative of the potential, it can be deduced that, due to the difference in the potential slope of the two
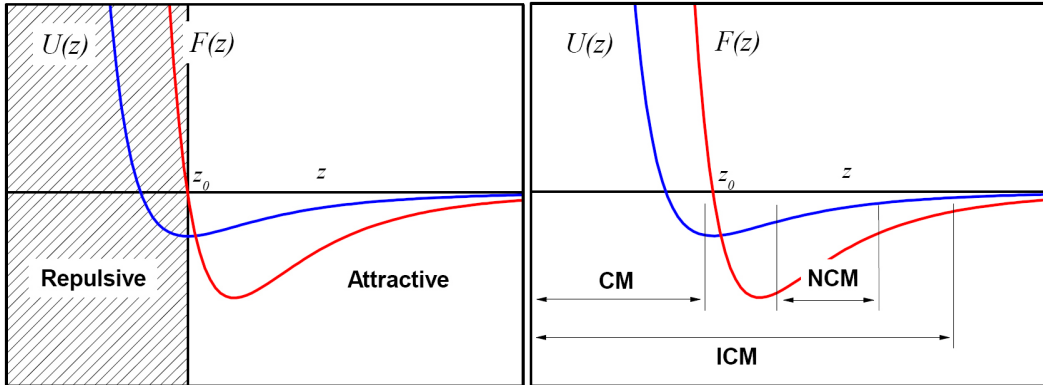
Figure 4.6: Left: Lennard-Jones potential $U(z)$ (blue) and the related force $F(z)$ (red); right: Distance dependence of Lennard-Jones potential and force vs. tip-surface separation. The tip-surface separation ranges in the contact mode (CM), non-contact mode (NCM), intermittent contact mode (ICM) are highlighted [Michele Giocondo 2012].

regimes, the attractive forces will be considerably weaker than the repulsive ones, as shown in Fig. 4.6. The details on contact and non-contact AFM modes can be found elsewhere (e.g. [Michele Giocondo 2012]).

In our work AFM measurements were performed in so-called tapping mode, thus the further description is dedicated to this one.

The main characteristic of the mode is the vibrating cantilever 1÷10 nm above the sample with a larger amplitude so that the tip hits the sample at the lowest point of each oscillation cycle. Furthermore, in this operating mode, the cantilever is excited at a frequency slightly lower than the mechanical resonance, and the topographical features are extracted using the amplitude modulation because of the forces generated by the intermittent interaction between the AFM tip and the sample. Tapping mode is possible at ambient temperature; however, the non-contact and intermittent modes of operation are easier in vacuum where the damping of cantilever oscillations is negligible, allowing for a much sharper resonance peak of the cantilever and hence higher sensitivity while measuring the shift in resonance frequency. Tapping mode is not disruptive for fragile samples since it eliminates completely friction forces between the tip and the sample that are dominant in contact mode. At the same time its resolution is better than in the no contact mode, in which the tip is in average more distant from the sample. Further description of the details related to the dynamics of an oscillating tip in proximity of a surface can be found in [Michele Giocondo 2012].

4.2.2.4 Transmission Electron Microscopy

Transmission Electron microscopy is a technique in which the image formation of ultra-thin specimen (the thickness of the order of 0.1 μm) is based on the interaction of electron beam with the specimen compound with subsequent magnification by magnet lenses (objective) and registration on fluorescent screen or CCD-camera. Theoretically maximum level of resolution of TEM with respect to the optical microscopes is caused by the small de Broglie wavelength of electrons. This gives rise to extremely high levels of resolution permitting to examine even a single column of atoms. The absorption of electrons in the material supplies an image contrast in TEM due to the thickness and composition of the material.

At smaller levels of magnification TEM image contrast is due to absorption of electrons in the material. Alternate modes of use allow to observe modulations in chemical identity, crystal orientation, electronic structure and sample induced electron phase shift as well as the regular absorption based imaging. The wavelength of electrons is related to their kinetic energy via the de Broglie equation. And in case of electron's velocity approaching the speed of light [Scott 2007], the additional correction must be made to take into account the relativistic effects see Equation 4.8:

$$\lambda_e \approx \frac{h}{\sqrt{2m_0E\left(1 + \frac{E}{2m_0c^2}\right)}} \tag{4.8}$$

where, h is Planck's constant, m_0 is the rest mass of an electron and E is the energy of the accelerated electron. The electron beam is formed on the base of a process known as thermionic emission from a filament, usually tungsten, or alternatively by field electron emission [Hubbard 1995]. The electrons are then accelerated by an electric potential and focused by electrostatic and electromagnetic lenses onto the sample. The transmitted beam contains information about electron density, phase and periodicity; this beam is used to form an image also.

4.2.2.5 UV-Visible spectrometry

The difficulty of the direct absorption measurement is the reason why a typical implementation of UV-Vis spectroscopy consists in measuring dependance of the power transmitted through the sample.

The most general optical processes for molecules illuminated by an incident beam are absorption (which can or can not lead to fluorescence) and scattering (elastic or inelastic). Photons involved in these processes 'disappear' from the incident beam and their energy is either transformed into heat in the sample or is re-emitted as photons in a different direction. The last reduces the power of the beam meanwhile it travels through the sample and results in a transmitted power P_{Tra}, smaller than the incident power P_{Inc}. The difference is called the extinguished power P_{Ext}. If, as mostly, only optical absorption (absorbed power is P_{Abs}) and scattering (scattered power is P_{Sca}) contribute to this *extinction*, the energy conservation will be:

$$P_{Ext} = P_{Abs} + P_{Sca}. \tag{4.9}$$

An *extinction cross − section*, σ_{Ext}, can therefore be defined, and we have:

$$\sigma_{Ext} = \sigma_{Abs} + \sigma_{Sca}. \tag{4.10}$$

From a measurement of the transmitted power, the amount extinguished is deducible, being simply the sum of the absorbed and scattered power.

For molecules, scattering is negligible compared to absorption, and extinction is then equal to absorption, i.e. $\sigma_{Ext} \approx \sigma_{Abs}$. This is why UV/Vis spectroscopy is often referred to an absorption spectroscopy, even if it should (strictly speaking) be called *extinction spectroscopy*. But, this is no longer true for larger objects, and in particular for nanoparticles, where the extinction spectrum (and not the absorption spectrum) is measured by UV-Vis spectroscopy. This is a particularly important distinction for metallic colloids, which constitute an important class of SERS substrates used in applications.

The Beer-Lambert law

For an incident power density S_{Inc} [W m^2], the power extinguished by a single molecule is by definition of the extinction cross-section $P_{Ext} = \sigma_{Ext} S_{Inc}$. This single molecule expression should be related to the case of an ensemble of molecules. If we will consider as the solution concentration of these molecules c_m [M] and an elementary volume of length dL [m] along the beam and surface area A [m^2] across. Thus, the power entering this box is therefore $P = S_{Inc} A$ [W]. Using Avogadro's number N_A [mol^{-1}], the volume contains $dN = N_A c_m A dL$ molecules, each of which contributes to extinction with a cross-section σ_{Ext} resulting in an extinguished power $dP_{Ext} = N_A \sigma_{Ext} S_{Inc} c_m A dL$. The power of the incident beam exiting the box is therefore $P + dP$ with $dP < 0$ and $dP = -dP_{Ext}$, i.e. we obtain the differential equation:

$$\frac{dP}{P} = -N_A \sigma_{Ext} c_m dL \tag{4.11}$$

$N_A \sigma_{Ext} c_m$ [m^{-1}] therefore represents the proportion of the extinguished power per unit length, called also extinction (or absorption) coefficient of the solution.

The power P_{Tra} transmitted though the solution over a path length L [m] (which is commonly 1 cm in typical experimental implementations) is then related to the incident power by integration of the previous differential equation, i.e.

$$P_{Tra} = P_{Inc} \exp(-N_A \sigma_{Ext} c_m L). \tag{4.12}$$

The *transmittance*, T, which is usually defined as the ratio of transmitted over incident power, is then could be written as $T = \exp(N_A \sigma_{Ext} c_m L)$. Usually, the most relevant quantity, and what is given as output in many UV-Vis spectrometers is the *absorbance* defined as [Valeur 2012]:

$$A = -\log_{10}(T) = \log_{10} \frac{P_{Inc}}{P_{Tra}} = \frac{N_A \sigma_{Ext} c_m L}{\ln(10)} \tag{4.13}$$

The *decadic molar extinction coefficient*, $\bar{e}$ [m^2 mol^{-1} in SI., usually expressed in cm^{-1} M^{-1}] of the molecule is defined as [1]:

$$\bar{e} = \frac{N_A \sigma_{Ext}}{\ln(10)}. \tag{4.14}$$

In analogy with the extinction cross-section, it depends on the excitation wavelength. It is essentially an alternative measure of the extinction cross-section of a molecule, but from an ensemble point of view rather than the single molecule approach. The absorbance then takes form:

$$A = -\log_{10}(T) = c_m \bar{e} L \tag{4.15}$$

The absorbance is therefore proportional to both the concentration and the molar extinction coefficient (or extinction cross-section). For molecules, since extinction and absorption are almost equal, the molar extinction coefficient is also sometimes called the *molar absorption coefficient* or *molar absorptivity*.

UV-Vis spectroscopy consists in measuring the wavelength dependence of the absorbance. For a solution of a known concentration, it is then possible to derive the decadic molar extinction coefficient and therefore the extinction cross-section (equal to the absorption cross-section for molecules). With this respect a useful expression could be easily derived from Equation 4.14, is:

---

[1] $\bar{e}$ is sometimes quoted in units of M^{-1}. It is implicitly that the length scale is 1 cm and should be understood as cm^{-1} M^1. It is also sometimes referred to as the *molar extinction coefficient*.

$$\sigma_{Ext}[cm^2] = 3.82 \times 10^{-21}(\bar{e}[cm^{-1}M^{-1}]), \tag{4.16}$$

which gives σ in cm^2 for $\bar{e}$ in cm^{-1} M^{-1}. As an alternative, UV-Vis spectroscopy can be used to determine the concentration of a solution of molecules (or nano-particles) of known molar extinction coefficient.

4.2.3   Experimental details of characterization techniques

Following every step of experimental procedure the systematic characterization of samples had been performed by means of aforementioned techniques, namely: Dynamic Light Scattering (DLS), Small-Angle X-ray Spectroscopy (SAXS), Atomic Force Microscopy (AFM), Transmission Electron Microscopy (TEM), UV-vis spectrophotometry and SERS. In this section the experimental details will be provided.

4.2.3.1   DLS measurements

DLS measurements I have done using a home-made instrument composed by a Photocor compact goniometer, an SMD 6000 Laser Quantum 50 mW light source operating at 532 nm, a photomultiplier (PMT-120-OP/B) and correlator (Flex02-01D). All the measurements were performed at $(25.00 \pm 0.05)°$C with the temperature controlled through the use of a thermostat bath.

4.2.3.2   Small-Angle X-Ray Spectroscopy (SAXS)

SAXS data of the solution were collected using an evacuated high performance SAXS instrument "SAXSess" (Anton Paar KG, Graz, Austria), which is a modification [Bergmann 2000] of the so-called "Kratky compact camera" [Kratky 1984]. Data collection has been performed in the slit collimation configuration with SAXSess camera attached to a conventional X-Ray source (CuKα, wavelength $\alpha = 1.5418$). The scattered radiation was recorded on a BAS-MS imaging plate (Fujifilm) and is processed with a digital imaging reader (Perkin Elmer Cyclone Plus Phosphor Imager) at a resolution in the small angle region of ≈ 60 nm ($= 2\theta/q_{min}$, with q_{min} the minimum accessible value of scattering vector permitted by our collimation setup, equal to 0.1 nm^{-1} and $q = 4\pi\sin\theta/\lambda$, 2θ being the scattering angle). After subtraction for the dark current, the empty sample holder and a constant background due to the thermal density fluctuations, the slit smeared data in the SAXS region (for $q < 4$ nm^{-1}) were deconvolved with the primary beam intensity distribution using SAXSquant 2.0 software to obtain the corresponding pinhole scattering (desmeared) intensity distribution.

4.2.3.3   AFM and SERS measurements

The topography of the micelle thin film as well as SERS measurements were carried out on the combined AFM/Raman commercial set-up Witec *alpha*300 (with 3D piezo-scanner spatial up to 3 nm). The topography images have been elaborated via the software WSxM 5.0 (Nanotec Electronica SL) [Horcas 2007]. SERS characterization I have performed in back scattering configuration using a microscope objective with magnification 60X (N.A. 0.8) in confocal mode (pinhole was provided by the core of the delivery optical fiber with D=50μm) and wd = 300μm, and a deep-depletion, back-illuminated Andor CCD camera (DV401A-BV-352) (1024$\times$400 pixels) operating at -60°C. SERS spectra and spectral images were acquired with an excitation source at 532 nm, provided by a frequency doubled Nd:YAG laser. All the spectra were acquired over the spectral range from 400 to 1800 cm^{-1}, with a spectral resolution ranging from 1 to 3.5 cm^{-1}, as estimated by the FWHM

of the 1001 cm^{-1} polysterene band. To avoid sample photodamage, the power impinging on the samples was limited to 60 μW. Integration time for single spectra acquisition was 10 seconds.

4.2.3.4 TEM measurements

Transmission electron microscopy images were obtained in bright field mode using a Philips EM 208S TEM with an accelerating voltage of 100 kV. For TEM characterization, the thin films were backed with a carbon film, floated off on water with the aid of a poly(acrylic acid) backing, and mounted on copper grids.

4.2.3.5 UV-Vis measurements

Extinction spectra I have repeatedly acquired to check the correspondence between UV/Vis measurements and SERS performances as indicator test, (Perkin Elmer UV-Vis-spectrometer Lambda 35) before and after polymer removal. The experimental characteristics of the instrument are: working range - 190-1100 nm, double beam operation, variable bandwidth 0.5-4 nm, absorbance range 3.2 A.

4.3   SERS-substrates characterization. Experimental results.

The central aim of the section is to provide the sequence of the experimental results that are closely inter-related to each other and support an idea of exceptional quality of the synthesized SERS substrates regarding their application both in case of red blood cell and PAH (pyrene).

4.3.1   Dynamic light scattering

Before the DLS measurements I have diluted the neat micelles solution down to the concentration of 1 mg/ml. As the model parameters of viscosity and refractive index the ones of toluene had been used, as the last is the major component of the initial solution. The measurements revealed the narrow diameter distribution of micelles (see Figure 4.7) around an average value of hydrodynamic radius R$_h$ = 18.6±0.5 nm (D 37.2±0.5 nm). Thus, the technique has shown the first experimental evidence of the quality of the micelles synthesized both in terms of their narrow size distribution and the size of nanometric scale itself.

While the first factor can already be considered as an essential prerequisite to the quality of the spatial distribution of the micelles upon film-coating, the second, taking also into account the experimental procedure of SERS-substrates synthesis (namely the position of the silver nanoclusters in the core of the micelle), gave us a preliminary idea of how the nanoclusters can be spatially distributed. As it will be shown, all the complex of measurements presented further just confirms these preliminary ideas.

4.3.2   Small angle X-ray spectroscopy

The quality of the micelles sphericity has been proved on the basis of SAXS measurements of the silver charged micelle solution (see Figure 4.8). These measurements revealed the quasi-ideal spherical composition so far as gyration radius is R$_g$=13.7 nm and its ratio to hydrodynamic one (R$_g$/R$_h$) results in a spherical parameter 0.74 (whereas for ideal sphere this parameter is equal to 0.75). Due to the fact that for spheres of radius R and uniform
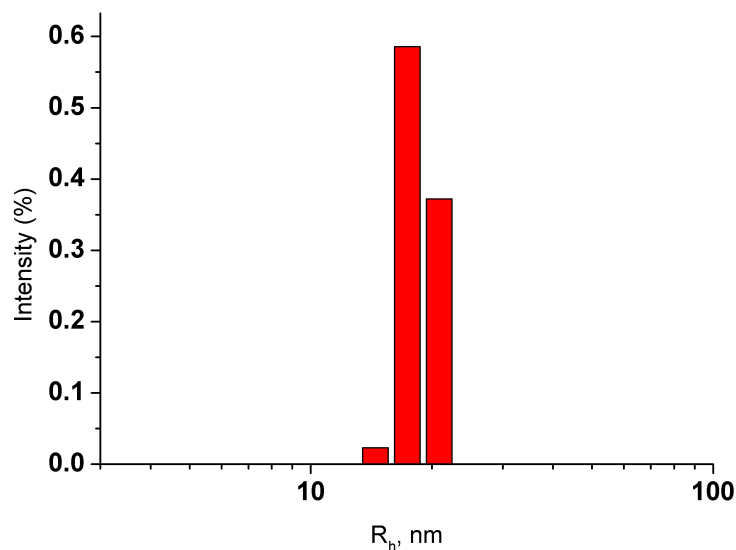
Figure 4.7: Hydrodynamic radius R$_h$ distribution.

electron density the relationship $<$R$_g^2>$=3/5R^2 may be used [Kratky 1984], giving R=17.7 nm is obtained in good agreement with the radius of micelle established (see Figure 4.8 A).
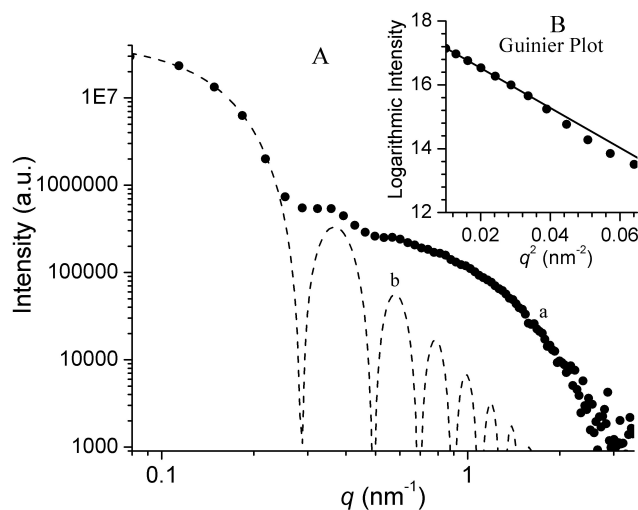
Figure 4.8: A: (a) SAXS desmeared curve of 0.25 wt% polystyrene-b-poly (4-vinyl pyridine) (PS-P4VP) block copolymer in 60/40 w/w toluene/tetrahydrofuran silver NPs charged solution obtained in situ by reduction of AgNO$_3$ with NaBH$_4$. Calculated scattering data from independently scattering spheres with radius equal to 15.7 nm (b) approximating the primary micellar aggregates present in solution. B: Guinier plot of experimental SAXS data (dots) in the low q region. The linear fit corresponding to root mean square gyration radius R$_g$ = 13.7 nm is indicated.

Therefore, as it can be seen, the information, obtained by this kind of characterization, gives us another clarification in terms of the quality of the micelles. Thus, being considered together with the DLS data and the technological step in substrate synthesis (namely, centrifugation and phase separation) responsible for the solution densification, the outcome obtained in the next section seems to be rather predictable than unexpected.

4.3.3 Atomic force microscopy

In fact, the morphology measurements of the micelles film spin-coated on silicon (see Figure 4.9, left panel), obtained by means of AFM in tapping mode and further data processing, revealed the morphology, representing high degree regular hexagonal arrays of PS-b-P4VP micelles. The theoretical details related to the microphase separation in diblock-copolymer melts, in particular ordering of micelles can be found elsewhere (e.g. [Semenov 1989]). As it could be seen (Figure 4.9, left and right panel) the single micelle diameter defined by this technique D_m(AFM) 35±2 nm are almost equal to the previously determined ones: D_m(DLS)=37.2±0.5, D_m(SAXS)=35.4±0.5. Thus, an additional confirmation of the qualitative and quantitative composition (quasi ideal spheres with narrow diameter distribution) of the solution has been achieved. The only discrepancy of the sizes, which is along Z-axis (Figure 4.9, right panel) can be explained by the incomplete collapsing of the micelles on the surfaces during film formation, accompanied by partial fusion of the coronal blocks of adjacent micelles with forming of "bumps" [Krishnamoorthy 2006].
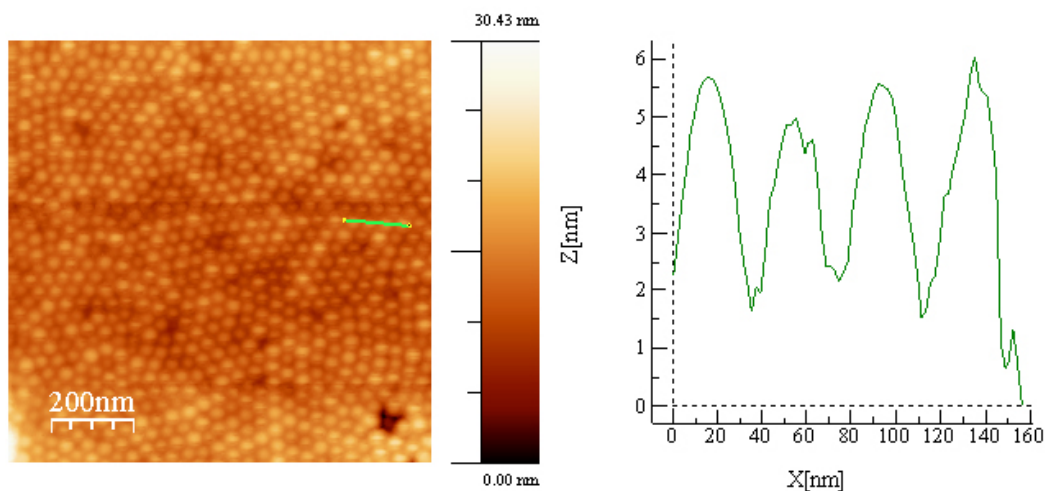
Figure 4.9: Left: Example of AFM morphological characterization of the micelle film on the silicon substrate with the profile line with marked profile; Right: profile section of the marked (green) one.

Thus, all the substrates' characterizations performed up to now, represent closely interrelated outcomes, and each of them stands as an independent indicator of the substrates' quality. In analogy to the previous conclusion, the results obtained by means of TEM can be considered as foreseeable also.

4.3.4 Transmission electron microscope

The diameter and gap (spatial) distribution of the Ag-nanoislands were determined by means of transmission electron microscopy (TEM). As shown in Figure 4.10, each silver cluster contained several tiny (2-6 nm) NPs. The average size D of each nanocluster of Ag NPs was estimated to be around D 26±2 nm. The gap between the cores was varied from 20 nm to 1-5 nm by increasing the spin-coating speed and micelles' concentration, with the best SERS performances for the smallest gap. The preserved hexagonal order of silver nanoclusters is predisposed by the hexagonally organized crew-cut micelles containing reduced silver in the core.
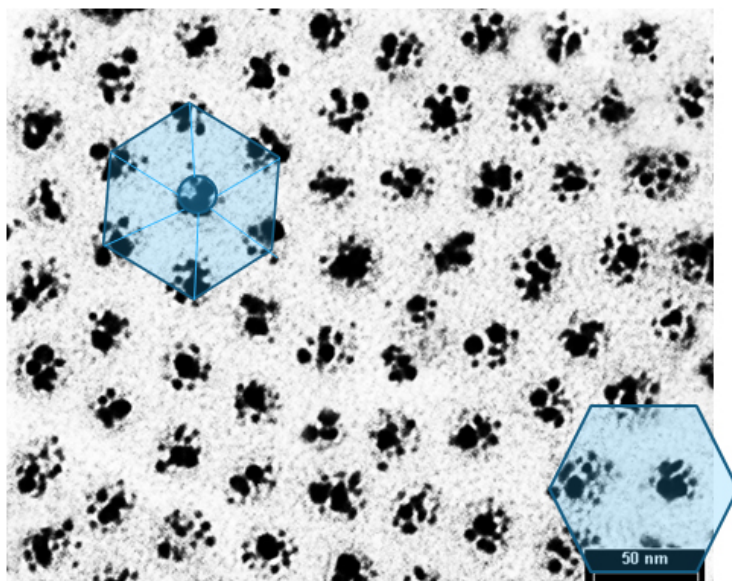
Figure 4.10: TEM micrograph of the plasmonic hexagonal lattice coated on glass and transferred on TEM carbon grid.

The major results obtained in this part of characterization, namely uniform hexagonally ordered identical silver nanoclusters, are of primary importance in terms of Raman hyperspectral imaging. Cause only in this case of uniform covering of the macro-scaled areas (with respect to the object under investigation) by silver nano-clusters one can be sure that the image acquired during the scanning is adequate and reflects the real chemical information. The further measurements will provide the additional confirmations to this concept.

4.3.5 UV-Vis spectrometry

SERS-substrates synthesis recipe, developed and adopted in the work enabled restoring of Ag-loaded micelles close packing geometry and uniformity. As shown on the Figure 4.11, the extinction curves that I have peaked around 430-440 nm and 470-500 nm, respectively were revealed, with tails up to 650 nm. This red-shift of the plasmonic peak is explained by the difference in dielectric constants of the media surrounding metallic NPs, i.e. higher dielectric medium causing the red-shift of plasmon resonance peak [Schultz 2003].

The determination of the LSPR peak position had been used as an auxiliary mechanism for optimization of the initial receipt for the SERS-substrate synthesis. Being used
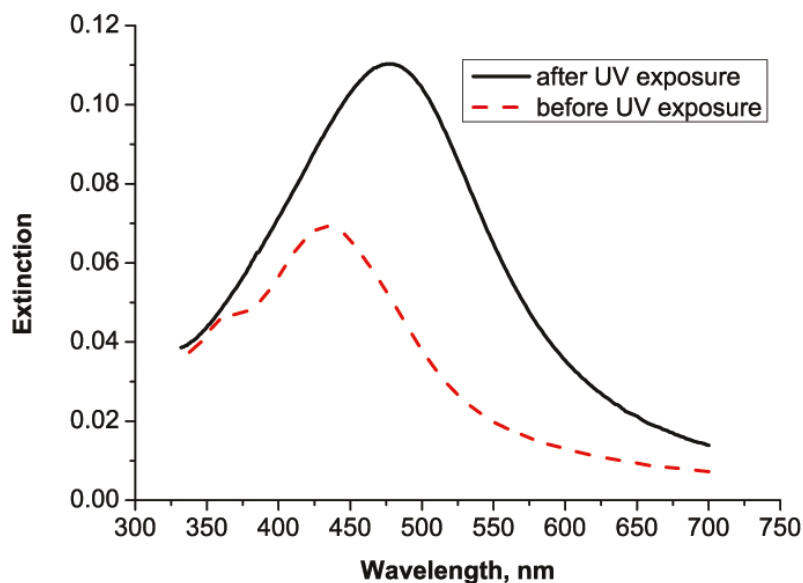
Figure 4.11: UV-Vis extinction of the plasmonic hexagonal lattice coated on glass after UV irradiation: before and after UV-exposure.

as an indicator of the substrates quality, the method permitted us to gain the condition when the laser excitation line matched the peak position of LSPR band [Tan 2013]. The condition gained is a indicator of how effectively the Raman signal will be amplified, cause the closer LSPR band to the excitation laser wavelength, the higher the level of amplified electromagnetic field "seen" by the molecule.

4.3.6 SERS characterization

Prior to the SERS characterization of the substrates, there where several inter-related auxiliary procedures performed, namely:

- Knife-edge like measurements sounding in the beam parameters determination, used further in the Enhancement factor evaluation;

- Preliminary SERS characterization and crystal violet deposition, used after in the micro and macro SERS characterization;

- Enhancement factor evaluation, procedure involved also in the section of the micro and macro SERS characterization.

4.3.6.1 Knife-edge-like measurements

The probed scattering area on the sample, A_{scat}, constrained by confocal detection in backscattering collection, and scattering volume were accurately measured independently by me with a knife-edge-like technique on a silicon wafer with sharp edge by using the Raman intensity of the 520 cm^{-1} silicon band as probe. Three-dimensional (3D) nano-positioning of the sample thanks to a piezo-scanner with an in plane resolution of 3 nm and

axial resolution pf 0.2 nm allowed the 3D characterization of the scattering volume. The best fit of Gaussian beam waist profiling resulted in a collection area equal to A_{scat}=0.44 μm^2. By analogy with Rayleigh length estimation for the depth of field of Gaussian beams, a 'Raman' depth, or effective thickness, was estimated given by $h_{eff} = 2.6 \pm 0.2 \mu m$ following [Cai 1998], and in good agreement with the fitted 'Raman' depth estimated of $1.4 \pm 0.2 \mu m$ via knife-edge scan tomography.

4.3.6.2 Preliminary SERS characterization and CV deposition

Crystal violet was diluted into a milli-Q water solution to different concentrations, namely 0.3, 3.1, 34.6, 43.8, 150, 380, 4200, 54000 nM. Then the particular employed solution was infiltrated into a cell constituted by two parallel substrates (24×24 mm^2) distanced by silica beads spacers of variable diameter depending on the desired thickness of the cell, from 4.8 μm ($\pm 4\%$) to 15 μm ($\pm 4\%$). For larger thickness, PET spacers were employed.

The planar cell was previously sealed at two of the external borders with UV glue. With this approach, the liquid is infiltrated into a precisely controlled volume. The entrance and flow windows retain the liquid to evaporate by the surface tension of water. Under this condition, the water goes out towards the center of the cell (see Figure 4.12). No inhomogeneity effect (coffee-ring) is visible at an optical microscopy inspection when high concentrated solutions are infiltrated ($\approx$ 5mM). In other words, the conditions provided cause a nearly perfect uniform layer of molecules. Molecular diffusion takes place at the borders of the evaporating water surface, which is represented by the water meniscus along vertical sections of the planar cell. The water meniscus then move towards the center of the cell as the liquid evaporates and leaves adsorbed molecules on the top and bottom surfaces. The lateral surface of the parallelepiped is negligible because of the small thickness ($\approx$100-200 μm) of the cell with respect to the width ($\approx$24 mm). Being top and bottom substrates identical, an equal deposition of the molecules is foreseen on the two surfaces. Thus, the spatial density of molecules on each substrate can be straightforwardly estimated. As it will be shown later, the uniformity of the molecular distribution of SERS enhancement factor as actually experimentally found for lower concentrated solution.

In a second phase, even more radical and simplified method of deposition was developed relying on the water surface tension properties that led to same outcomes. The exploiting of the surface tension of the water sustaining the top substrate if the cell permitted avoiding the use of spacer and border sealing. In other word, a 100-μl volume was left in the center and covered gently by the other glass that spread uniformly the liquid till the glass borders. The thickness of the volume embedded within the two silver-coated coverslips changed along water evaporation zone, always keeping a constant area of adsorption.

Preliminary the G_{av} I have calculated assuming a number of CV molecules estimated as described below. A volume of 100 μl of 380 nM solution of CV distributed over an area 24×24 mm^2=576 mm^2, doubled because of two adsorbing surfaces, produced a number of molecules $N_{surf} = 8683$ within the scattering area of 0.44 μm^2. Given the effective diameter D_{CV} 1nm of the CV molecule covering an approximate area of 0.785 nm^2, and the number of molecules N_{surf} estimated in the scattering area, the molecular filling fraction of the probed area is only 1.5 % (less than one monolayer). Given D=26 nm and an average g=3 nm, that corresponded to a number of molecules per cluster $N_c = 13$. For the reproducibility test a concentration of 4.2 μM was deposited with the same approach producing a number of molecules in 0.44 μm^2 of 95990, with N_c=145.
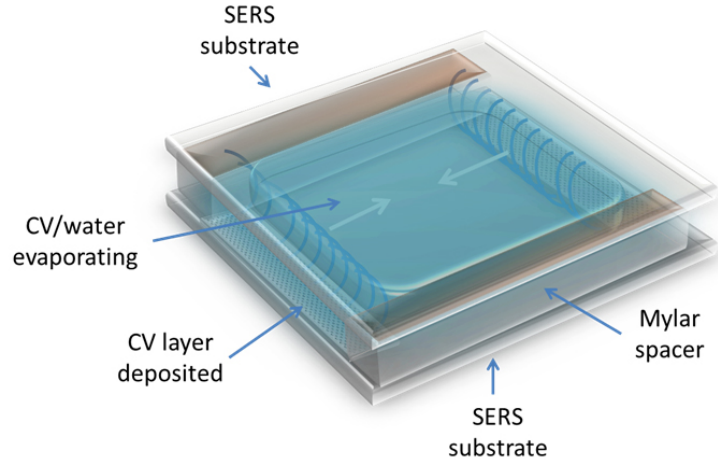
Figure 4.12: Schematic view of the single cell with illustration of the CV-solution evaporation.

4.3.6.3 Enhancement factor evaluation

The enhancement factor of the substrates was estimated under the condition of molecular deposition described above, namely N_{surf}. Raman enhancements were evaluated using the definition of the *SERS substrate enhancement factor* of [Ru 2009], namely as

$$\mathbf{G} = \frac{I_s/N_{surf}}{I_R/N_{vol}}, \tag{4.17}$$

where I_s and I_R are the enhanced and standard amplitudes of one Raman peak, respectively, and N_{surf} and N_{vol} are the numbers of molecules estimated in the scattering area and volume respectively (see Figure 4.13), contributing effectively to the signal I_s and I_R.
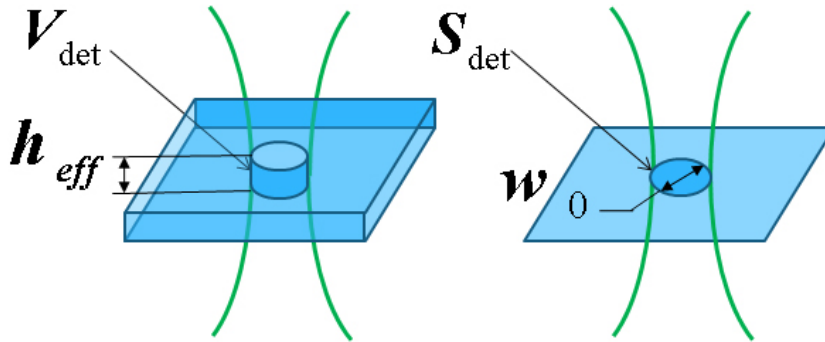
Figure 4.13: Schematic representation of scattering volume and scattering area.

Integrating the radial intensity within h_{eff}, the scattering volume resulted is 2.01 μm^3. Hence, for the G evaluation, the Raman reference signal I_R of CV was normalized to the number N_{vol} following the procedure described in [Cho 2012] by measuring the average scattering from the bulk CV powder. Unfortunately, the approach aforementioned led to a value of G overestimated of 2 orders of magnitude. Mainly because the strong absorption of

CV molecules at 532 nm [Korppi-Tommola 1981] and having a molar extinction coefficient approximately of $0.5 \cdot 10^5$ cm^{-1} M^{-1}, causing the small amount of molecules from a volume with an effective thickness of 30 nm, that could actually contribute to the Raman signal detected (a fraction of 3% of our scattering volume).

The last was confirmed by measurements carried out in diluted water solution of 1.1. mM and 5.3 mM CV which demonstrated an adequate and reliable normalization I_R/N_{vol}. Finally, the reference was acquired also for a solid layer, 30-nm thick, obtained by CV deposition from a solution with concentration 100 μM. The instability of the reference signal I$_R$ caused all these precautions. In fact, as it was found experimentally, the detected signal varied linearly with power and integration time only for power (impinging on the sample) <200 μW and integration time below a few seconds. Above this threshold of power, I$_R$ started to decrease significantly for increasing power till reaching a kind of saturation regime in the milli-Watts range. Comparing intensity signals upon normalization to the incident power and integration time, often much larger in standard Raman (even orders of magnitude) than SERS, would have led to irreproducible comparison attempts between different experiments, as well as to underestimated values of IR. The experimental values were then I$_S$=830 counts measured with an incident power P$_i$ = 12 μW and integration time Δt= 1 s, from N$_{surf}$=8.683. The reference was instead I$_R$= 216 counts with 69 μW of power for 10 s and from an estimated number of molecules N$_{vol}$=4.07$\times 10^7$, that is given by a fraction of 3% of the bulk powder within the scattering volume. Thereby, I have estimated a value G = 1.04$\times$106$\pm$3.6% (error given as the mean value of spatial reproducibility of standard deviation over the set of 25, 2.500-μm^2 areas). This value was in a good agreement with what was found by the other determinations of the Raman reference.

4.3.6.4 Macro- and micro-scaled SERS characterization

SERS characterization had been implemented aiming the experimental confirmation of the reasonable enhancement factor (allowing the detection of the minute quantities of the analyte) and the signal's reproducibility throughout the large area. The last fact, due to the peculiarity of the application, has to essentially transcend the linear sizes of the red blood cell and this condition is absolutely necessary in terms of performances equivalence of all the areas that would be potentially involved in the SERS measurement of single red blood cell. In other words, this examination is a checking test for the SERS-substrates' constitution regarding the uniform matrix of silver nanoclusters with equal efficiency.

Experimentally SERS characterization has been performed in a couple of scales: micro- and macroscale. While the task of the first one was the determining of SERS productivity at the scales comparable to the single RBC, the second one was organized at the macroscale level with respect to the RBC size. In both cases mentioned, the measurements were performed using the crystal violet as the analyte molecule (see CV's SERS spectra in Figure 4.14) and revealed an effective amplification of the Raman signal also on glass, despite of essential decrease of the Enhancement Factor (EF) due to the minor dielectric constant of common borosilicate glass (ε=4) with respect to the silicon wafer (ε=12) [Etchegoin 2010].

Enhancement factor uniformity has been estimated by measuring the SERS spectra of probe Crystal Violet (see Figure 4.14) that was almost uniformly dispersed on the substrate see Figure 4.15, 4.12. Enhancement factor estimated is to be in the range of 10^6 on glass. As shown in Figure 4.15 a very large uniformity was experimentally demonstrated with the standard deviation σ<10% over a large area of 6400 μm^2, and a value of σ 3% over an area of 16 μm^2.

The second 'macro'-characterization of the SERS intensity response of our substrates had been organized in a following way: there were 25 raster scans performed spaced by 2
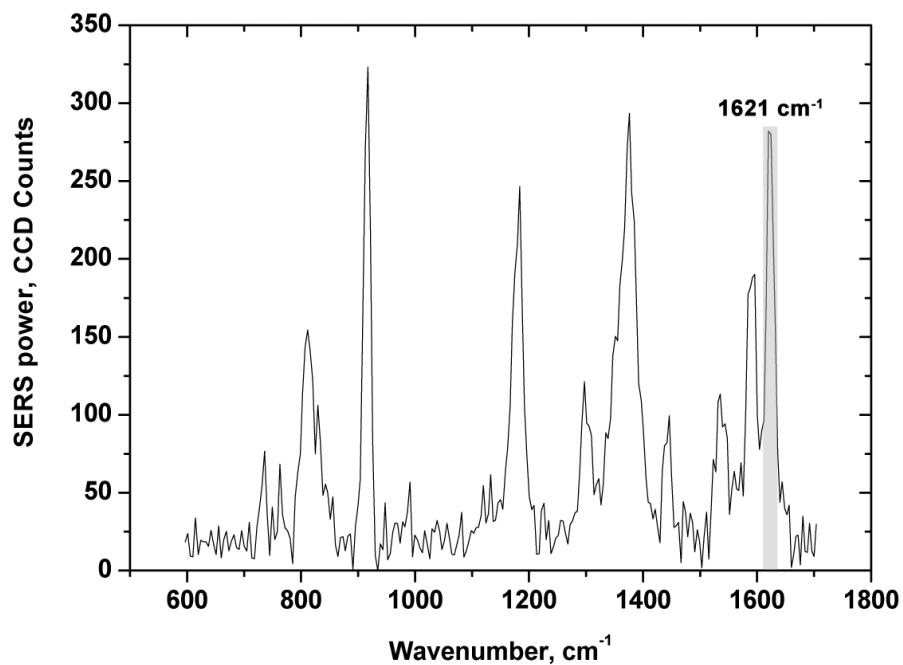
Figure 4.14: Crystal violet SERS spectra with 1620 cm^{-1} characteristic peak marked.
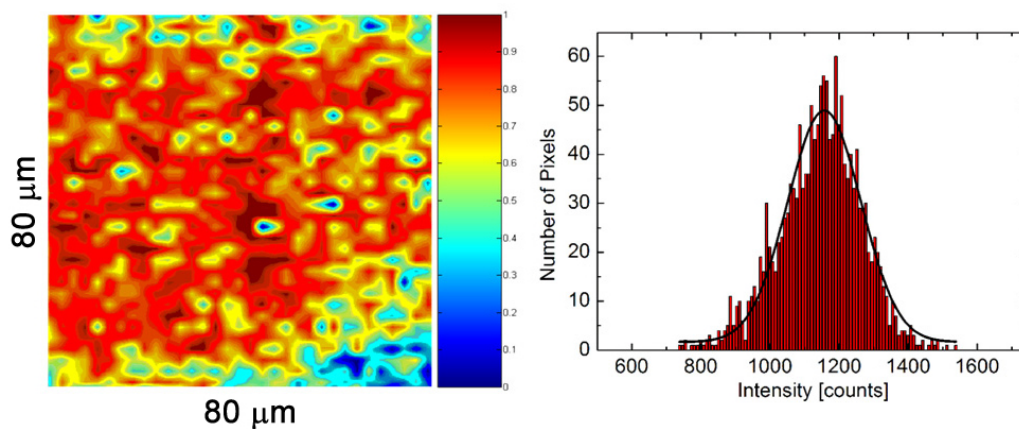
Figure 4.15: Left panel: surface distribution of the 1620 cm^{-1} peak over 80×80 μm^2 (1600 sampling points (pixels); right panel: Gaussian fit of the 1620 cm^{-1} peak intensities distribution.
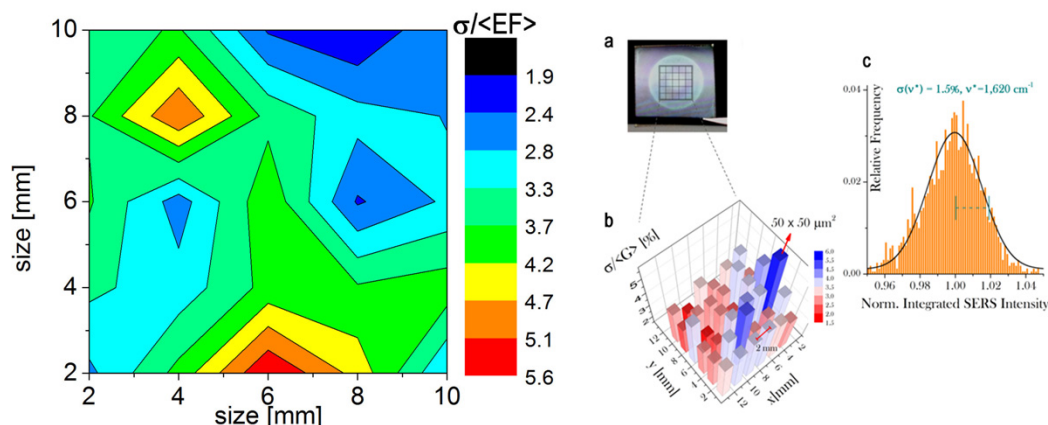
Figure 4.16: Left - Relative standard deviation ($\sigma/<\text{EF}>$) distribution diagram; right - a) - plasmonic substrate photo, appearing with a reflective green glow at ambient light; b) hyperspectral representation that were selected from a regular grid (also depicted in a) of 1 cm^2; c) the demonstration of an excellent reproducibility of the biosensor detection area: is characterized by a normal distribution of the SERS intensity, collected by spatial sampling multiple local regions of the nanotexture plane.

mm over the area of 1 cm^2 of 50$\times$50 μm^2 for each scan area sampled with 1-μm spacing (See Figure 4.16). The resulted standard deviation σ is in the range of 0.9-5.6% over the all area. The local spatial fluctuation of the SERS signal is notably below any reported data. The full area (1 cm^2) standard deviation is $<$30% despite of the huge scale of characterization. It is worth to note, that this characterization-dependent value, $G_{AV}\approx10^6$ is only a 'perceived enhancement', i.e. an operational estimate, and does not represent a limit to the achievable enhancement. The experiments can undergo dramatic differences in the measured enhancement and sensitivity capability in relation to different plasmonic surrounding conditions, basically because of the high localization of the electromagnetic field in the cluster-based substrate and change of molecular adsorption affinity.

The most significant result provided by these series of measurements is the uniform SERS response of the plasmonic nanocoated glass. The last, being finely tailored for biological applications, permits also an integral cell sensing without the spatial injurious convolution of the SERS signal with typical position-dependent amplification. Thus, the fact of eventual variations of the signal during the measurements can be ascribed exclusively to the molecular dynamics and random spatial fluctuations of the cell membrane thanks to the deep examining by the complex of SERS substrates characterization techniques. And of course, as it will be shown in the next Chapter, this fact is of paramount importance. Additionally, the standard deviation around the average SERS signal ($<$30%) over the colossal scale of 1 cm^2 allows acquiring thorough statistic information required for significant biological assays on many cells on the same substrate and with extensive reliability and integrity.

4.4   Conclusion

Thus, as I have demonstrated, the SERS substrates obtained represent an optimal combination of features imposed to the high-performance ones, namely: high enhancement factor and perfect SERS-signal reproducibility over an exhaustive area (with respect to the linear

sizes of the objects under investigation). The features outlined are of crucial importance in terms of reliability of the SERS measurements. In particular, spectra oscillations that unavoidably take place during the experiment can be surely attributed exclusively to the local composition of biological macromolecules that are directly interacting (or at immediate vicinity) with the SERS substrate nanoclusters. This fact, of course, is fundamental, cause only in this way the chemical composition revealed is authentic and reliable in both cases: RBC and pyrene.

SERS substrates application. Results and discussion

5.1 Red blood cell membrane hyperspectral imaging

In the numerous studies on cells, tissues, and micro-organisms, two major parameters determining the meaning and usefulness of the vibrational information were defined:

1. the lateral resolution and, hence, the size, number, amount, and heterogeneity of biological object(s) the information is obtained from;

2. the detection sensitivity, which is of consequence to the duration of the measurements and therefore to sample integrity, time resolution, and in-vivo applicability.

Taking into account the outcomes of substrates characterization obtained previously, one can deduce, that our substrates are in a strong coherence to the requirements posed to vibrational information presented above. Thereby, the results on substrates characterization presented in the previous chapter form a solid basis for the substrates to be used when investigating red blood cell membrane (RBC membrane) and pyrene.

RBC is usually considered as an ideal system for single cell analysis since it is devoid of nucleus and other organelles and consists of a lipid bilayer membrane with embedded integral and peripheral proteins, and carbohydrates. The non-nucleated erythrocyte is unique among human cells in that the plasma membrane, its only structural component, responsible for all of its diverse antigenic, transport, and mechanical characteristics and thanks to its high deformability, plays a crucial role in oxygen transfer from blood to tissues in microcirculation. It is worth to note also that while much progress has indeed been made in the understanding of the structural organization of the various lipid and protein components of the normal red cell membrane, the current models are far from comprehensive and continue to evolve. A study using state-of-the-art proteomic approaches [Pasini 2006] has generated a comprehensive catalog of red cell proteins and has identified more than 300 proteins including 150 integral membrane proteins. The current membrane models account for fewer that 15 % of these molecules! [Mohandas 2008].

Therefore, when we are talking about the red blood cell membrane, every new approach needs to be tested, and welcomed if the reliable and authentic information is obtainable. The last prerequisite is undoubtedly satisfied condition in our case.

Considering ordinary Raman-spectroscopy, the spectra are dominated by hemoglobin (Hb) (principal content of the cell) and therefore it is quite difficult to isolate the contribution of the membrane. Meanwhile, SERS substrates with high spatial reproducibility are therefore ideal to detect the amplified Raman response originated from the interaction of the membrane with the plasmon excited in our self-assembled Ag-NPs. Below the experimental details related to the red blood cell membrane characterization are given.

The raster scans on large area (up to 100×100 μm^2) I have acquired to inspect the substrate before systematically investigation of multiple-area SERS enhancement. This

last covered the full area of 100 mm^2 in the centre of the 576-mm^2 plasmonic coating. The erythrocytes were collected from the blood stream and injected into normal saline solution (0.90% w/v of NaCl,   300 mOsm/L) in ratio 50: 1,000 v/v, then infiltrated into a sealed planar cell of thickness 20 μm formed by a top coverslip and a bottom SERS substrate. After 30-60 min, the erythrocytes floating in Brownian motion were found in contact with the bottom plasmonic surface. SERS chemical maps were acquired on several erythrocytes per substrate, with a power incident on the sample in the range 1 - 42 μW, that is a laser intensity comprised between a value as low as 2.3$\times$10^2 W/cm^2 and a maximum of 1 $\times$ 10^4 W/cm^2. The integration time Δt was varied depending on the experiment from 0.02s for statistical fluctuation acquisition $\mu(\tau)$ up to 4.0s for time-averaged spatial signal S(x, y). Important, that the experiments last typically less than 2h, taken together with the moderate laser power and short integration times are considered as protective measures for the prevention of the object degradation.

In the Figure 5.1 the main principle of our measurements is schematically represented.
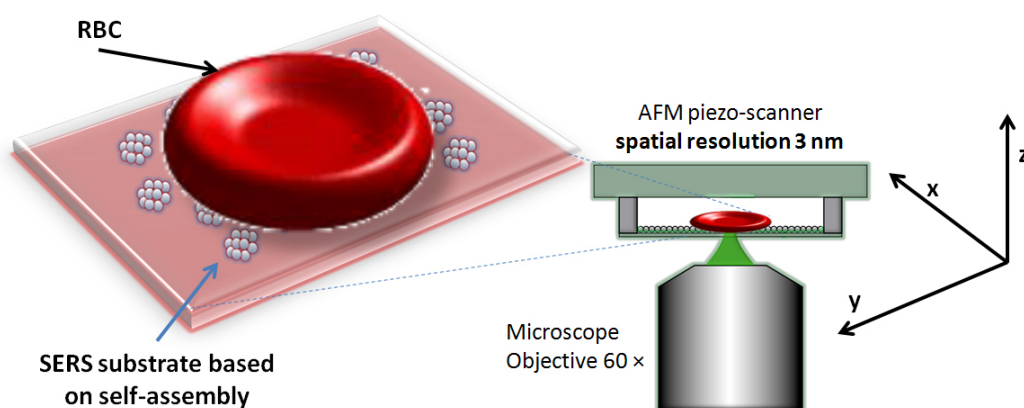
Figure 5.1: The principle of the single red blood cell SERS-imaging.

On the left side an RBC brought in a close contact with SERS-substrate is schematically depicted (without the scales compliance). On the right hand the SERS-substrate (with an analyte) and microscope objective together with the 3-D axes are represented. Note, that the spatial resolution is defined by confocal configuration and also by hot-spot/absorption efficiency.

In the Figure 5.2 is the scheme of the experimental measurement of red blood cells is represented both for Raman and SERS. The method based on the sequential scanning along the Z axis from the Z= 0 position (the position of maximum signal) into the body of RBC and in opposite direction (marked as in negative). As it has been found, in the case of Raman all the spectra obtained are characteristic for hemoglobin. Moving along Z axis only the intensity of the peaks changes, but the principle spectra is preserved. Thereby, it can be derived that in Raman measurements the volume contribution of the main inner RBC component is observed only.

On the contrary, in case of SERS measurements the maximum of signal is observed when the impinging laser is focused on the RBC-SERS substrate contact interface (Z= 0 position), thus giving rise to the signals substantially different from the hemoglobin ones. Whereas moving out from this point provokes an essential decaying of the signal, thus giving a clear idea about the surface nature of the enhancement.
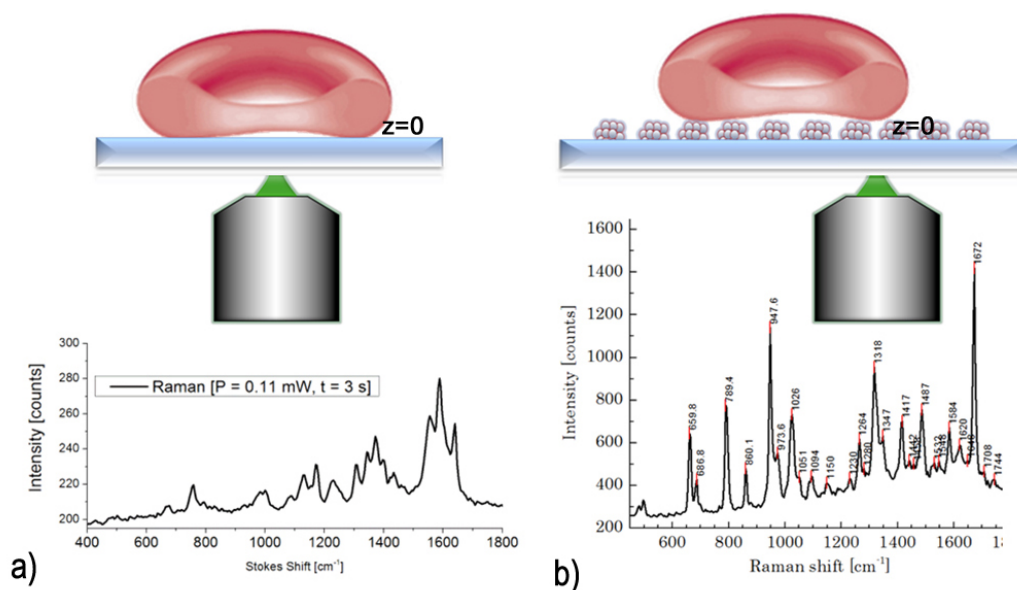
Figure 5.2: a) The schematic representation of the experiment on the determination of the Raman axial characterization curve (top); characteristic hemoglobin spectra revealed in this mode (bottom); b)The schematic representation of the experiment on the determination of the SERS axial characterization curve (top); characteristic example SERS spectra revealed in this mode (bottom).

Thus, as the intermediate conclusion it can be stated that the SERS measurements of the RBC membrane provide its components detection only and free from any contribution of the cell's inner part. The last, of course, is crucial in terms of the of investigations of the RBC's membrane.

Further, the scanning along preselected line on the surface of RBC membrane has been performed (see Figure 5.3).

As it can be seen form the illustration the spectra changes from point to point. The reason of such behavior, according to the previously performed tough characterization of samples, can be explained by the molecular dynamics of the RBC constituents that are currently in a direct contact with an illuminated part of silver nanoclusters only. Moreover, this experiment provides an additional insight into the potentiality of these substrates to be used in molecular dynamics measurements.

Both the complexity of the object (see Figure 5.4) and the high sensitivity of the SERS-substrates cause the richness of the spectra acquired (see Figure 5.5) to a large extent.

Meanwhile, in SERS spectra, despite of the general complexity of the spectra acquired, the presence of different cellular components can be directly demonstrated (for instance, see Figure 5.6). In the same time pure Raman spectra can provide the evidence of hemoglobin presence only (see Figure 5.7).

Hyperspectral SERS imaging obtained by projecting of particular spectral bands over the scansion area revealed high correlation with the optical image acquired via microscopy on the same cell. In Figure 5.8, example of the surface-enhanced spectral image obtained from the typical band of protein group Amide I and the corresponding optical image of the same cell are shown. Characteristic lipid bands have also been significantly associated with
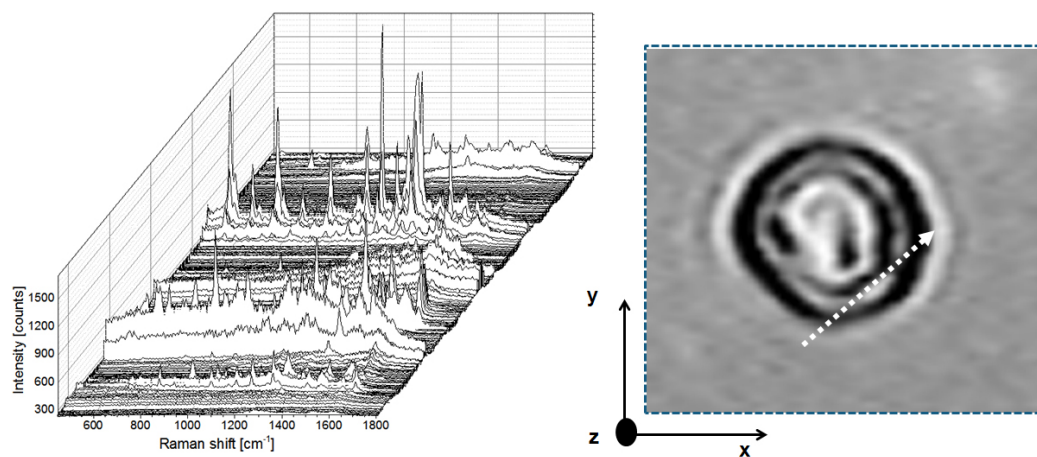
Figure 5.3: Example of the SERS spectra evolution during the scanning in XY-plane.
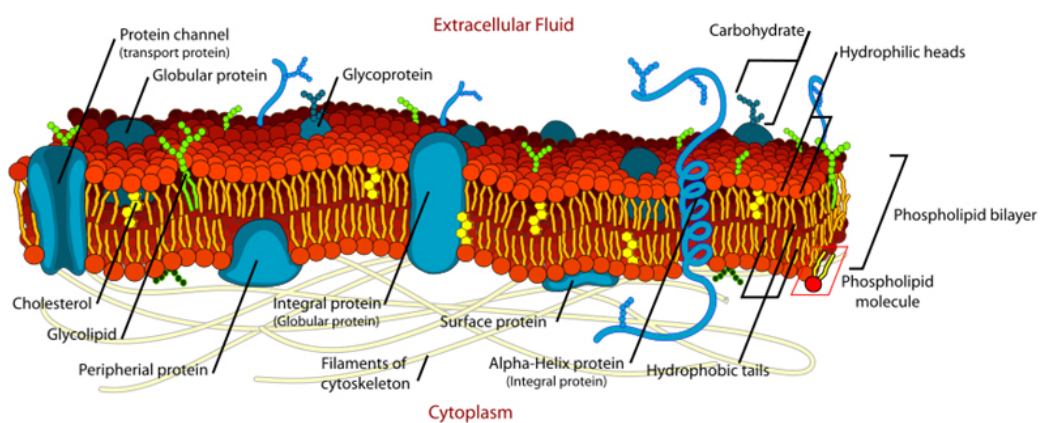
Figure 5.4: Schematic illustration of RBC-membrane.
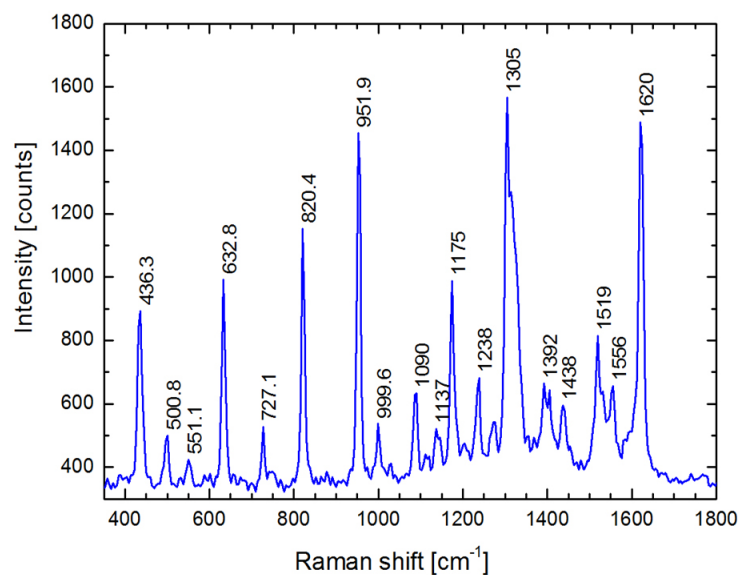
Figure 5.5: The example of the SERS spectra acquired while performing the scanning in X-Y plane.
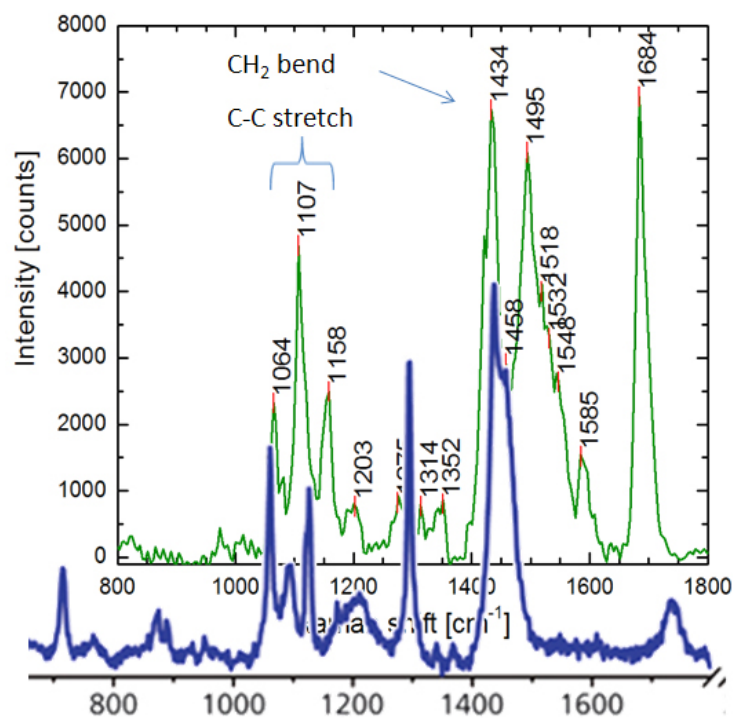
Figure 5.6: Confrontation between phospholipid bilayer measured using our SERS substrates (green one) and the one taken from the literature [Ahmed 2011] (blue one).
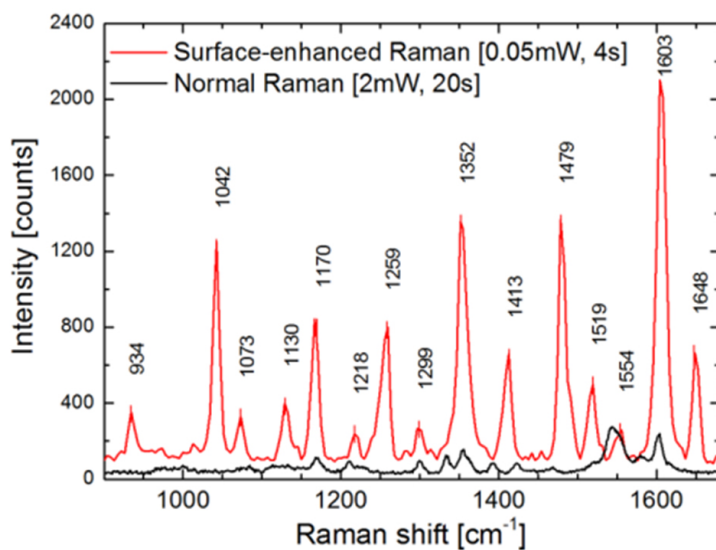
Figure 5.7: The confrontation of the experimental results provided using different techniques: Raman and SERS.

the borders of the RBC where the interaction with the substrate is stronger because of the biconcave shape of the RBC. According to our conclusion, such correlation is another clear evidence of the membrane origin of measured SERS signal.
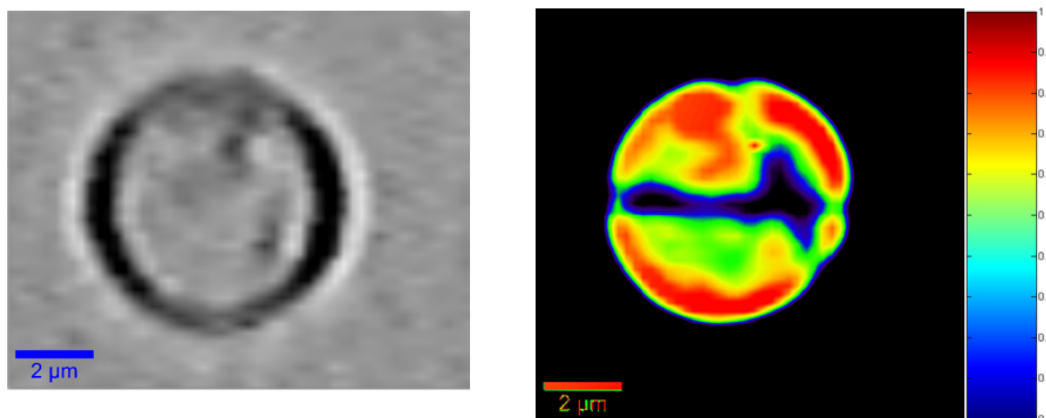
Figure 5.8: Confrontation between optical image (left) and SERS image (right).

In addition, as it can be seen also from the Figure 5.9, even if the only contributor to the Raman spectra is hemoglobin, the 3D reconstruction of this component distribution intensities correlates with the SERS-image given before.

Thus, on the base of the results supplied, I can definitely state again, that the origin of the signal used in SERS-imaging of red blood cell belongs only to its membrane components. Consequently, the first general aim of the work - to demonstrate the applicability of the surface-enhanced Raman spectroscopy in revealing of the chemical content of the red blood cell membrane - is achieved.
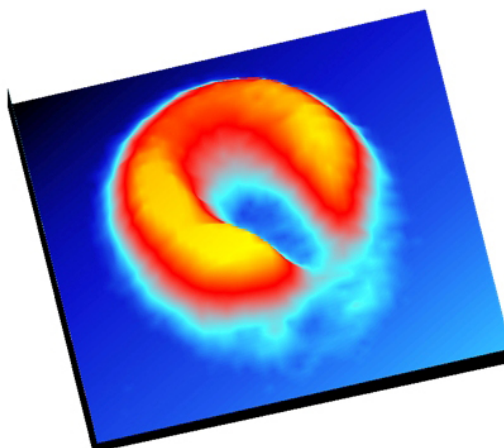
Figure 5.9: 3D reconstruction of the Raman imaging of the RBC based on the intensities of hemoglobin.

5.2   Tentative peaks assignment

A comparison of the typical spectra detected along the membrane scan with the Raman spectrum of ghost erythrocyte membranes reported by Mikkelsen [Mikkelsen 1978] pointed out an excellent agreement with the membrane average chemical signature. By analysing the coincidence of recurrent peaks and correlation with the Raman bands reported for molecular membrane constituents, i.e. glycoproteins and glycolipids [Morrison 1971, Gahmberg 1973, Fukuda 1979, Gordon-Smith 2013], we were able to identify significant features into the SERS spectra. At a deeper level, not only there was a strong evidence of glucose [Cael 1974] and N-acetyl-glucosamine [She 1974] skeletal vibrational fingerprint but also a perfect matching of the peaks in all the spectral range up to 1500 cm^{-1}. Of particular relevance were considered the vibrations corresponding to 515, 533, 1008-1015, 1020-1026, 1036-1038, 1046-1050, 1089-1094, 1111-1113, 1150, 1263, 1334, 1432 cm^{-1} belonging to investigated monosaccharides also constituting the units of the erythrocyte carbohydrate coat (please refer to [Cael 1974] for details). A comparative analysis with the Raman spectrum of galactose [Gahmberg 1973] also gave a good agreement into several spectral regions. Concomitantly, given the highly structured nature of the detected spectra in the frequency region <900 cm^{-1} due to carbohydrates and C-S/S-S modes of peptides and the intermittent presence of peaks in the spectral region 1600 â 1700 cm^{-1} denoting the presence and conformation of the protein along with the amide III correlated signature, it resulted very difficult to discriminate between the peptides [Podstawka 2004, Kurouski 2012, Blum 2012] and carbohydrates contribution to the SERS spectra. In fact, several evidences comprising the S-S bridge (500-550 cm^{-1}) and C-S (600-670 cm^{-1}) normal mode (cysteine) [Van Wart 1986, Qian 1992, Kurouski 2012] together with the population of the amide I [Podstawka 2004] and amide III [Lippert 1975] ascribable to glycine, leucine, methionine, phenylalanine, proline, valine and tryptophan (886 cm^{-1}) led to the conclusion of detecting the SERS of both carbohydrates and proteins. Besides, extremely intense and well defined peaks showing very large signal to

noise ratio were also matched with the phospholipid content (described earlier, see Figure 5.6) (C-C stretch in the region 1060-1130 cm^{-1}, PO$_4^-$- stretch and CH$_2$ twist and bend) [Lippert 1975, Wallach 1975, Gaber 1978, De Gelder 2007].

Remarkably, spectra acquired at low excitation power ($<$10 μW) were characterized occasionally by the presence of a very simple structure of peaks (even consisting of only two very intense peaks on a blank continuum). I believe that this could be due to the particular sensitivity curve of the substrate that allowed detection only molecules in close proximity to the SERS hot spots (therefore belonging to the carbohydrate coat on the plasma membrane expressing integral and peripheral glycosylated proteins and glycolipid rafts) and occasionally with a Raman gain so large to enable a true single-molecule detection with very few frequencies of larger intensity.

In addition, although possessing the reproducible population of vibrational frequencies, the main character of the experimental SERS detections was essentially represented by the change in the relative intensities of the Raman modes along a raster scan. Thus, inferring the conclusion of positional sensitivity to the local molecular population convoluted with the Brownian fluctuations and molecular dynamics within the living erythrocyte membrane. By collecting the SERS signal at the same positions in sequential mapping (also with different spatial resolution) in selected region of the cell, I have found the spectra to be reproducible and characterized by the same relative intensities despite the considerable time delay of tens of seconds between subsequent acquisitions.

5.3 Polycyclic aromatic hydrocarbon (pyrene) detection

First, let's briefly describe the nature of polycyclic aromatic hydrocarbons (PAH). PAH are a group of different chemical compounds with a condensed multibenzene structure. As it has been outlined, PAHs are important environmental pollutants formed during the incomplete burning of coal, oil, and gas or other organic substances such as tobacco or carboiled meat [Leyton 2004]. They can be found as a mixture of different related molecular compounds in air, soil, and water due to both natural process and human activity. Because many of them have been reported to be strong carcinogens [Guo 2004] it is important to find an effective and selective method to detect them.

The main challenge in detection of the PAH by means of SERS is their electronic structure. Although coupling of π-electrons of PAH with the metal substrate should occur, this class of compounds does not present a specific functional group that could act as a strong anchor to the surface of the substrate that would intensify the SERS effect via a significant chemical mechanism. Moreover, in the presence of the substrates traditionally used in SERS analysis, the PAHs were observed to decompose [Costa 2006]. Despite of these natural constraints the approach used here is supposed to be based on three fundamental factors: physisorption, high enhancement factor, short signal exposition (integration) time and moderate laser power.

The main reason for the application of the SERS technique for the detection as well as the quantitative determination of PAH is the enormous enhancement of the intensity of the Raman scattered radiation is due to the adsorption of the molecules of PAH on the metal. Moreover, due to the enhanced sensitivity of the detection, measurements provided in this section enabled the pyrene minute concentration (of the level of μM) detection (see Figure 5.10).

As it can be seen from the Figure 5.10, the intensity of the SERS signal, even with the 2,333-fold lower laser power, is much more pronounced with respect to the Raman one. So, this example on the substrates application represent an obvious advantage when used
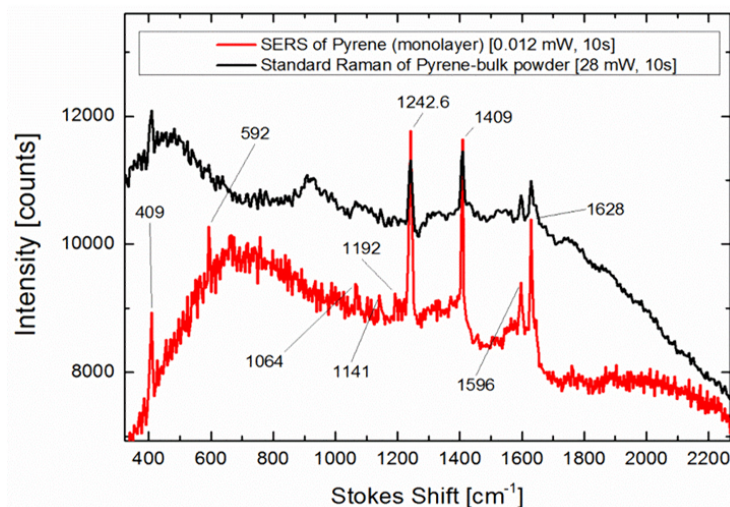
Figure 5.10: Confrontation between Raman and SERS spectrum of pyrene.

with this particular compound, despite the all precautions caused by its specific structural composition.

Thus, in this part of the work the applicability of our SERS-substrates in the detection of the minute concentrations of pyrene has been experimentally demonstrated. Due to the exceptional combination of the fundamental properties of substrates enhancement and reproducibility the detection of pyrene became possible. Therefore, the second general aim has also been successfully achieved by demonstrating of the results given here.

5.4   Conclusion

Thus, on the base of the results obtained and presented in this chapter, the conclusion on the successful applicability of our SERS-substrate to the investigation of the chemical content of the RBC-membrane and pyrene can be straightforwardly deduced. The richness of the spectral information provided by SERS-technique is caused exclusively by the molecular dynamics of the chemical content of RBC membrane. Therefore, on the base of accurate peaks assignments with reference to the data available currently in the literature, the method proposed possess all necessary in order to become a simple routine protocol for the RBC membrane and pyrene investigation.

5.5   Future perspectives

Thus, on the base of fundamental demonstration of the applicative capacities and general performance of our SERS substrates the following proposals for the future perspectives are proposed: Regarding the RBC investigation:

- to perform the comparative analysis based on the confrontation of SERS spectra and mechanical characteristics of RBC obtained by using optical tweezers system. Thus, the possible correlation can be observed, based on the mechanical properties and chemical structure;

- to see at the molecular level the distribution of the chemical compounds of RBC membrane in comparison with the healthy and ill donors.

Relating to pyrene detection future work will be concentrated on the further sensitivity enhancement, thus enabling the detection of the trace concentrations of the pyrene.
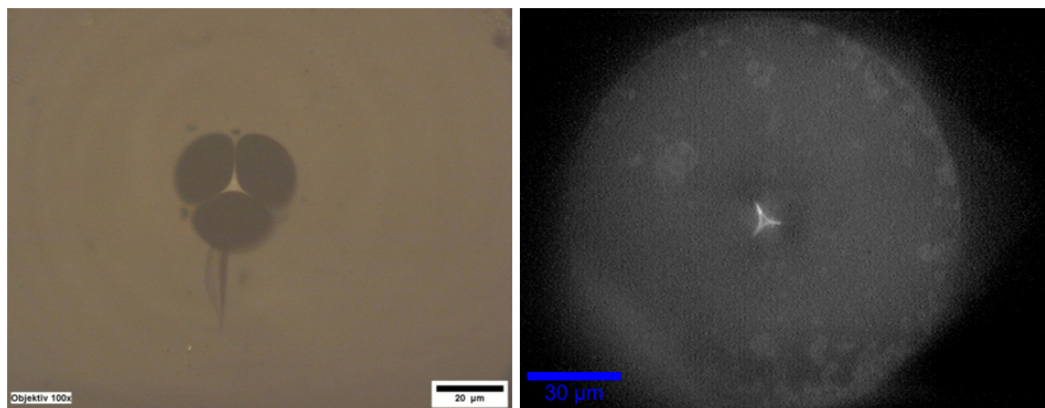
Figure 5.11: Left: detail of the microstructured cladding of the Mercedes fiber. Right: image of the microstructured fiber core with visible Raman back-scattering (through notch filter).

The work is supposed to be based on the involvement of the fiber-based SERS sensors (see Figure 5.11). The working surface will be created by infiltration of our SERS solution within the air capillaries of a 3-hole suspended (non-commercial) core fiber, thus permitting us to test the possibility of "signals' accumulation along propagation" in order of further signal enhancement. The preliminary works performed include:

- the on-going characterization of these novel fiber sensors;

- the optimization of the polymers' removal through the thermal annealing;

- the effects of signal degradation because of the propagation losses;

- the functionalization of the active coating for improving the molecular affinity of the target molecules.

Conclusion

On the base of the results obtained throughout the work the following states are need to be underlined:

1. the SERS substrates, based on block-copolymer self-assembly, representing a compromise between top-down and bottom-up techniques and involving the advantages of both has been successfully synthesized;

2. on the base of the sequence of different and closely interrelated characterization techniques high enhancement factor ($\approx 10^6$), excellent spatial reproducibility of the SERS signal (with standard deviation around $< 30\%$ over a colossal scale (10×10 mm^2)), and ordered morphology in the aspect of ultra-high density array of silver nanoclusters of uniform size and gap distance has been revealed.

3. the applicability of the ones has been successfully demonstrated on the example of red blood cell membrane and pyrene;

4. due to the positive results obtained in the previous clause the future perspectives have been sharply outlined.

Below the most significant details of the aforementioned items are presented.

The preliminary work related to the overview of the existing methods for SERS substrates synthesis revealed the dilemma including the combinations of advantages and drawbacks of two main synthesis families top-down and bottom-up. Basing on the detailed analysis of the recipes finally it has been found, that the block-copolymer self-assembly based approach represent a flexible method for the SERS substrate synthesis unifying the advantages of both previously noted techniques, namely: simple synthesis, high enhancement factor, high uniformity on small scale.

Further experimental testing of the substrates, synthesized under the experimentally modified approach, has confirmed their excellent performance characteristics, satisfying both aspects of "SERS uncertainty principle", namely: high enhancement factor and signal reproducibility. Also, in correspondence with the complex of the characteristics revealed, the conclusion on the signal's origin has been deduced - the amplified Raman response originates *only* from the interaction of the object analyzed with the plasmon excited in silver nanoparticles of the substrate. Thus, the chemical content of the species is exclusively revealed.

The quality of the outcomes listed above permits the further development of the measurement principle. Providing the combined examination of both chemical content and mechanical properties of RBC's, the technique is also supposed to be able to discern the spectral content of the healthy and ill donors.

As to the further development of the approach in respect the pyrene detection, the method is planned to be combined with the fiber-based SERS-sensors technique.

Finally, the work represents the successful attempt of synthesis and application of the ordered ultrahigh-density templates of nano-textured silver particles for the surface-enhanced

Raman spectroscopy of red blood cell membranes and pyrene. Thanks to its unique combination of the features, namely high-enhancement factor and signal reproducibility, the spectral information revealed by the application of substrates is strictly authentic and reliable. Therefore, eventual variations of the signal can be then ascribed to the molecular dynamics and random spatial fluctuations of the cell membrane. Thus, the substrates do possess an optimal combination of characteristics to provide such a delicate, label-free, sensitive and chemically specific measurements and an integral cell sensing with no spatial injurious convolution of the SERS signal with typical position-dependent amplification. As a consequence, the application of such SERS-active templates can find large employment for biochemical and environmental sensing.

Bibliography

[Abid 2002] J. P. Abid, A. W. Wark, P. F. Brevet and H. H. Girault. *Preparation of silver nanoparticles in solution from a silver salt by laser irradiation.* Chem. Commun., pages 792–793, 2002. 29

[Abu Hatab 2008] Nahla A. Abu Hatab, Jenny M. Oran and Michael J. Sepaniak. *Surface-Enhanced Raman Spectroscopy Substrates Created via Electron Beam Lithography and Nanotransfer Printing.* ACS Nano, vol. 2, no. 2, pages 377–385, 2008. 45

[Aeschlimann 2009] Martin Aeschlimann, Michael Bauer, Daniela Bayer, Tobias Brixner, Stefan Cunovic, Frank Dimler, Alexander Fischer, Walter Pfeiffer, Martin Rohmer, Christian Schneider, Felix Steeb, Christian Strüber and DmitriV. Voronine. *Simultaneous Spatial and Temporal Control of Nanooptical Fields.* In Paul Corkum, Sandro Silvestri, Keith A. Nelson, Eberhard Riedle and Robert W. Schoenlein, editeurs, Ultrafast Phenomena XVI, volume 92 of *Springer Series in Chemical Physics*, pages 705–707. Springer Berlin Heidelberg, 2009. 30, 31

[Ahmed 2011] Selver Ahmed, Stephanie L Wunder and Zhorro S Nickolov. *Raman Spectroscopy of Supported Lipid Bilayer Nanoparticles.* 2011. v, 75

[Albrecht 1977] M. Grant Albrecht and J. Alan Creighton. *Anomalously intense Raman spectra of pyridine at a silver electrode.* Journal of the American Chemical Society, vol. 99, no. 15, pages 5215–5217, 1977. 17

[Amendola 2006] Vincenzo Amendola, Stefano Polizzi and Moreno Meneghetti. *Laser Ablation Synthesis of Gold Nanoparticles in Organic Solvents.* The Journal of Physical Chemistry B, vol. 110, no. 14, pages 7232–7237, 2006. 42

[Aroca 2007] Ricardo Aroca. Chemical effects and the sers spectrum, pages 107–132. John Wiley Sons, Ltd, 2007. 24

[Arunkumar 1983] K. A. Arunkumar and E. B. Bradley. *Theory of surface enhanced Raman scattering.* The Journal of Chemical Physics, vol. 78, no. 6, 1983. 22

[Arya 1984] Karamjeet Arya and Roland Zeyher. *Theory of surface-enhanced Raman scattering.* In Manuel Cardona and Gernot Guntherodt, editeurs, Light Scattering in Solids IV, volume 54 of *Topics in Applied Physics*, pages 419–462. Springer Berlin Heidelberg, 1984. 22

[Asher 1985] Sanford A. Asher and Craig R. Johnson. *UV resonance Raman excitation profile through the 1B2u state of benzene.* The Journal of Physical Chemistry, vol. 89, no. 8, pages 1375–1379, 1985. 12

[Baltá-Calleja 1989] F.J. Baltá-Calleja and C.G. Vonk. X-ray scattering of synthetic polymers. Numeéro v. 8 de Polymer science library. Elsevier, 1989. 54

[Banholzer 2008] Matthew J. Banholzer, Jill E. Millstone, Lidong Qin and Chad A. Mirkin. *Rationally designed nanostructures for surface-enhanced Raman spectroscopy.* Chem. Soc. Rev., vol. 37, pages 885–897, 2008. 2

[Barcikowski 2007] Stephan Barcikowski, Ana Menéndez-Manjón, Boris Chichkov, Marijus Brikas and Gediminas Račiukaitis. *Generation of nanoparticle colloids by picosecond and femtosecond laser ablations in liquid flow.* Applied Physics Letters, vol. 91, no. 8, pages −, 2007. 42

[Barry 1992] B. W. Barry, H. G. M. Edwards and A. C. Williams. *Fourier transform Raman and infrared vibrational study of human skin: Assignment of spectral bands.* Journal of Raman Spectroscopy, vol. 23, no. 11, pages 641–645, 1992. 16

[Bates 1990] Frank S. Bates and Glenn H. Fredrickson. *Block Copolymer Thermodynamics: Theory and Experiment.* Annual Review of Physical Chemistry, vol. 41, no. 1, pages 525–557, 1990. PMID: 20462355. 44

[Bates 1994] Frank S. Bates and Glenn H. Fredrickson. *Conformational Asymmetry and Polymer-Polymer Thermodynamics.* Macromolecules, vol. 27, no. 4, pages 1065–1067, 1994. 44

[Bäumer 1999] Marcus Bäumer and Hans-Joachim Freund. *Metal deposits on well-ordered oxide films.* Progress in Surface Science, vol. 61, no. 7-8, pages 127 − 198, 1999. 39

[Benten 2005] W. Benten, N. Nilius, N. Ernst and H.-J. Freund. *Photon Emission Spectroscopy of Single Oxide-Supported Ag-Au Alloy Clusters.* Phys. Rev. B, vol. 72, page 045403, Jul 2005. 40

[Berger 1991] S. D. Berger, J. M. Gibson, R. M. Camarda, R. C. Farrow, H. A. Huggins, J. S. Kraus and J. A. Liddle. *Projection electronâbeam lithography: A new approach.* Journal of Vacuum Science Technology B, vol. 9, no. 6, pages 2996–2999, 1991. 31

[Bergmann 2000] Alexander Bergmann, Doris Orthaber, Günther Scherf and Otto Glatter. *Improvement of SAXS measurements on Kratky slit systems by Göbel mirrors and imaging-plate detectors.* Journal of Applied Crystallography, vol. 33, no. 3 Part 2, pages 869–875, Jun 2000. 58

[Berndt 2009] Michael Berndt, Martin Rohmer, Brian Ashall, Christian Schneider, Martin Aeschlimann and Dominic Zerulla. *Polarization selective near-field focusing on mesoscopic surface patterns with threefold symmetry measured with PEEM.* Opt. Lett., vol. 34, no. 7, pages 959–961, Apr 2009. iii, 30, 31, 32

[Binns 2001] C. Binns. *Nanoclusters deposited on surfaces.* Surface Science Reports, vol. 44, no. 1â2, pages 1 − 49, 2001. 38

[Blum 2012] Carolin Blum, Thomas Schmid, Lothar Opilik, Norman Metanis, Simon Weidmann and Renato Zenobi. *Missing Amide I Mode in Gap-Mode Tip-Enhanced Raman Spectra of Proteins.* The Journal of Physical Chemistry C, vol. 116, no. 43, pages 23061–23066, 2012. 77

[Bohren 1983] Craig F. Bohren and D.R. Huffman. Absorption and scattering of light by small particles. Wiley science paperback series. Wiley, 1983. 19

[Bosbach 1999] J. Bosbach, D. Martin, F. Stietz, T. Wenzel and F. Träger. *Laser-based method for fabricating monodisperse metallic nanoparticles.* Applied Physics Letters, vol. 74, no. 18, pages 2605–2607, 1999. 40

[Botiz 2010] Ioan Botiz and Seth B. Darling. *Optoelectronics using block copolymers.* Materials Today, vol. 13, no. 5, pages 42 − 51, 2010. 43

[Bromann 1997] Karsten Bromann, Harald Brune, Christian Félix, Wolfgang Harbich, René Monot, Jean Buttet and Klaus Kern. *Hard and soft landing of mass selected Ag clusters on Pt(111)*. Surface Science, vol. 377â379, no. 0, pages 1051 − 1055, 1997. European Conference on Surface Science. 38

[Broyer 1987] M. Broyer, B. Cabaud, A. Hoareau, P. Melinon, D. Rayane and B. Tribollet. *Velocity slip measurements of bismuth clusters produced by the inert gas condensation technique*. Molecular Physics, vol. 62, no. 3, pages 559–572, 1987. 38

[Burmeister 1997] Frank Burmeister, Claudia Schäfle, Thomas Matthes, Matthias Böhmisch, Johannes Boneberg and Paul Leiderer. *Colloid Monolayers as Versatile Lithographic Masks*. Langmuir, vol. 13, no. 11, pages 2983–2987, 1997. 34

[Cael 1974] John J. Cael, Jack L. Koenig and John Blackwell. *Infrared and raman spectroscopy of carbohydrates : Part IV. Identification of configuration- and conformation-sensitive modes for D-glucose by normal coordinate analysis*. Carbohydrate Research, vol. 32, no. 1, pages 79 − 91, 1974. 77

[Cai 1998] W.B. Cai, B. Ren, X.Q. Li, C.X. She, F.M. Liu, X.W. Cai and Z.Q. Tian. *Investigation of surface-enhanced Raman scattering from platinum electrodes using a confocal Raman microscope: dependence of surface roughening pretreatment*. Surface Science, vol. 406, no. 1â3, pages 9 − 22, 1998. 64

[Campbell 1997] Charles T. Campbell. *Ultrathin metal films and particles on oxide surfaces: structural, electronic and chemisorptive properties*. Surface Science Reports, vol. 27, no. 1â3, pages 1 − 111, 1997. 39

[Campion 1998] Alan Campion and Patanjali Kambhampati. *Surface-enhanced Raman scattering*. Chem. Soc. Rev., vol. 27, pages 241–250, 1998. 19, 23

[Cao 2002] Rongchao Mirkin Chad A Cao YunWei Charles Jin. *Nanoparticles with Raman spectroscopic fingerprints for DNA and RNA detection*. Science, vol. 297, pages 1536–1540, 2002. 2

[Cason 2000] Joanna P. Cason, Kedar Khambaswadkar and Christopher B. Roberts. *Supercritical Fluid and Compressed Solvent Effects on Metallic Nanoparticle Synthesis in Reverse Micelles*. Industrial Engineering Chemistry Research, vol. 39, no. 12, pages 4749–4755, 2000. 28

[Chang 1975] T. H. P. Chang. *Proximity effect in electron-beam lithography*. Journal of Vacuum Science Technology, vol. 12, no. 6, pages 1271–1275, 1975. 31

[Chang 1987] RK Chang. *Surface enhanced Raman-scattering at electrodes - a status report*. Berichte der bunsen-Gesellschaft-Physical Chemistry Physics, vol. 91, no. 4, pages 296–305, APR 1987. 24

[Chen 2002a] Dong-Hwang Chen and Yan-Wen Huang. *Spontaneous Formation of Ag Nanoparticles in Dimethylacetamide Solution of Poly(ethylene glycol)*. Journal of Colloid and Interface Science, vol. 255, no. 2, pages 299 − 302, 2002. 28

[Chen 2002b] Sihai Chen and David L. Carroll. *Synthesis and Characterization of Truncated Triangular Silver Nanoplates*. Nano Letters, vol. 2, no. 9, pages 1003–1007, 2002. 28

[Cheng 1994] Hai-Ping Cheng and Uzi Landman. *Controlled Deposition and Classification of Copper Nanoclusters.* The Journal of Physical Chemistry, vol. 98, no. 13, pages 3527–3537, 1994. 38

[Cho 2012] Won Joon Cho, Youngsuk Kim and Jin Kon Kim. *Ultrahigh-Density Array of Silver Nanoclusters for SERS Substrate with High Sensitivity and Excellent Reproducibility.* ACS Nano, vol. 6, no. 1, pages 249–255, 2012. 34, 47, 65

[Costa 2006] J.C.S. Costa, A.C. Santana, P. Corio and M.L.A. Temperini. *Chemical analysis of polycyclic aromatic hydrocarbons by surface-enhanced Raman spectroscopy.* Talanta, vol. 70, no. 5, pages 1011 − 1016, 2006. Colloquium Spectroscopicum Internationale XXXIV, CSI XXXIV. 3, 78

[Creighton 1979] J. Alan Creighton, Christopher G. Blatchford and M. Grant Albrecht. *Plasma resonance enhancement of Raman scattering by pyridine adsorbed on silver or gold sol particles of size comparable to the excitation wavelength.* J. Chem. Soc., Faraday Trans. 2, vol. 75, pages 790–798, 1979. 27, 36

[Crooks 2001] Richard M. Crooks, Mingqi Zhao, Li Sun, Victor Chechik and Lee K. Yeung. *Dendrimer-Encapsulated Metal Nanoparticles: Synthesis, Characterization, and Applications to Catalysis.* Accounts of Chemical Research, vol. 34, no. 3, pages 181–190, 2001. PMID: 11263876. 28

[Cushing 2004] Brian L. Cushing, Vladimir L. Kolesnichenko and Charles J. O'Connor. *Recent Advances in the Liquid-Phase Syntheses of Inorganic Nanoparticles.* Chemical Reviews, vol. 104, no. 9, pages 3893–3946, 2004. PMID: 15352782. 28, 41

[De Gelder 2007] Joke De Gelder, Kris De Gussem, Peter Vandenabeele and Luc Moens. *Reference database of Raman spectra of biological molecules.* Journal of Raman Spectroscopy, vol. 38, no. 9, pages 1133–1147, 2007. 78

[Dick 2002] Lisa A. Dick, Adam D. McFarland, Christy L. Haynes and Richard P. Van Duyne. *Metal Film over Nanosphere (MFON) Electrodes for Surface-Enhanced Raman Spectroscopy (SERS): Improvements in Surface Nanostructure Stability and Suppression of Irreversible Loss.* The Journal of Physical Chemistry B, vol. 106, no. 4, pages 853–860, 2002. 45

[Dimitrov 1996] Antony S. Dimitrov and Kuniaki Nagayama. *Continuous Convective Assembling of Fine Particles into Two-Dimensional Arrays on Solid Surfaces.* Langmuir, vol. 12, no. 5, pages 1303–1311, 1996. iii, 33, 34, 35

[Drachev 2004] Vladimir P. Drachev, Mark D. Thoreson, Eldar N. Khaliullin, V. Jo Davisson and Vladimir M. Shalaev. *Surface-Enhanced Raman Difference between Human Insulin and Insulin Lispro Detected with Adaptive Nanostructures.* The Journal of Physical Chemistry B, vol. 108, no. 46, pages 18046–18052, 2004. 40

[Duff 1987a] D. G. Duff, A. C. Curtis, Peter P. Edwards, D. A. Jefferson, Brian F. G. Johnson, A. I. Kirkland and D. E. Logan. *The Morphology and Microstructure of Colloidal Silver and Gold.* Angewandte Chemie International Edition in English, vol. 26, no. 7, pages 676–678, 1987. 28

[Duff 1987b] D. G. Duff, A. C. Curtis, Peter P. Edwards, D. A. Jefferson, Brian F. G. Johnson and D. E. Logan. *Morphologie und Nanostruktur von kolloidalem Gold und Silber.* Angewandte Chemie, vol. 99, no. 7, pages 688–691, 1987. 28

[Edwards 1995] H.G.M Edwards, A.C Williams and B.W Barry. *Potential applications of FT-Raman spectroscopy for dermatological diagnostics.* Journal of Molecular Structure, vol. 347, no. 0, pages 379 − 387, 1995. Molecular Spectroscopy and Molecular Structure 1994. iii, 16

[Elias 1983] P M Elias. *Epidermal lipids, barrier function, and desquamation.* The Journal Of Investigative Dermatology, vol. 80 Suppl, pages 44s − 49s, 1983. 17

[Erin B. Dickerson 2008] Xiaohua Huang Ivan H. El-Sayed Hunghao Chu Sujatha Pushpanketh John F. McDonald Mostafa A. El-Sayed Erin B. Dickerson Erik C. Dreaden. *Gold nanorod assisted near-infrared plasmonic photothermal therapy (PPTT) of squamous cell carcinoma in mice.* Cancer letters, vol. 269, no. 1, pages 57–66, 2008. 42

[Esumi 2000] Kunio Esumi, Akihiro Suzuki, Atsushi Yamahira and Kanjiro Torigoe. *Role of Poly(amidoamine) Dendrimers for Preparing Nanoparticles of Gold, Platinum, and Silver.* Langmuir, vol. 16, no. 6, pages 2604–2608, 2000. 28

[Esumi 2005] Kunio Esumi, Takashi Matsumoto, Yuusuke Seto and Tomokazu Yoshimura. *Preparation of gold-, gold/silver-dendrimer nanocomposites in the presence of benzoin in ethanol by {UV} irradiation.* Journal of Colloid and Interface Science, vol. 284, no. 1, pages 199 − 203, 2005. 41

[Etchegoin 2010] Pablo G. Etchegoin and Eric C. Le Ru. Basic electromagnetic theory of sers, pages 1–37. Wiley-VCH Verlag GmbH Co. KGaA, 2010. 66

[Evanoff 2005] David D. Evanoff and George Chumanov. *Synthesis and Optical Properties of Silver Nanoparticles and Arrays.* ChemPhysChem, vol. 6, no. 7, pages 1221–1231, 2005. 27

[Fayaz 2010] Amanulla Mohammed Fayaz, Kulandaivelu Balaji, Morukattu Girilal, Ruchi Yadav, Pudupalayam Thangavelu Kalaichelvan and Ramasamy Venketesan. *Biogenic synthesis of silver nanoparticles and their synergistic effect with antibiotics: a study against gram-positive and gram-negative bacteria.* Nanomedicine: Nanotechnology, Biology and Medicine, vol. 6, no. 1, pages 103 − 109, 2010. 29

[Félidj 2004] N. Félidj, S. Lau Truong, J. Aubard, G. Lévi, J. R. Krenn, A. Hohenau, A. Leitner and F. R. Aussenegg. *Gold particle interaction in regular arrays probed by surface enhanced Raman scattering.* The Journal of Chemical Physics, vol. 120, no. 15, pages 7141–7146, 2004. 36

[Fischer 1981] U. Ch. Fischer and H. P. Zingsheim. *Submicroscopic pattern replication with visible light.* Journal of Vacuum Science Technology, vol. 19, no. 4, pages 881–885, 1981. 33

[Fleischmann 1974] M. Fleischmann, P.J. Hendra and A.J. McQuillan. *Raman spectra of pyridine adsorbed at a silver electrode.* Chemical Physics Letters, vol. 26, no. 2, pages 163 − 166, 1974. 17

[Fredrickson 1989] Glenn H. Fredrickson and Kurt Binder. *Kinetics of metastable states in block copolymer melts.* The Journal of Chemical Physics, vol. 91, no. 11, 1989. 44

[Fukuda 1979] M Fukuda, M N Fukuda and S Hakomori. *Developmental change and genetic defect in the carbohydrate structure of band 3 glycoprotein of human erythrocyte membrane.* Journal of Biological Chemistry, vol. 254, no. 10, pages 3700–3703, 1979. 77

[Gaber 1978] B.P. Gaber, P. Yager and W.L. Peticolas. *Deuterated phospholipids as non-perturbing components for Raman studies of biomembranes.* Biophysical Journal, vol. 22, no. 2, pages 191 – 207, 1978. 78

[Gahmberg 1973] Carl Gustav Gahmberg and Sen-itiroh Hakomori. *External Labeling of Cell Surface Galactose and Galactosamine in Glycolipid and Glycoprotein of Human Erythrocytes.* Journal of Biological Chemistry, vol. 248, no. 12, pages 4311–4317, 1973. 77

[Glass 2003] R. Glass, M. Arnold, J. Blümmel, A. Küller, M. Möller and J.P. Spatz. *Micro-Nanostructured Interfaces Fabricated by the Use of Inorganic Block Copolymer Micellar Monolayers as Negative Resist for Electron-Beam Lithography.* Advanced Functional Materials, vol. 13, no. 7, pages 569–575, 2003. 45

[Gonzalo 2003] J Gonzalo, R Serna, J Solís, D Babonneau and C N Afonso. *Morphological and interaction effects on the surface plasmon resonance of metal nanoparticles.* Journal of Physics: Condensed Matter, vol. 15, no. 42, page S3001, 2003. 39

[Gonzalo 2005] J. Gonzalo, A. Perea, D. Babonneau, C. N. Afonso, N. Beer, J.-P. Barnes, A. K. Petford-Long, D. E. Hole and P. D. Townsend. *Competing processes during the production of metal nanoparticles by pulsed laser deposition.* Phys. Rev. B, vol. 71, page 125420, Mar 2005. 40

[Gordon-Smith 2013] Ted Gordon-Smith. *Structure and function of red and white blood cells.* Medicine, vol. 41, no. 4, pages 193 – 199, 2013. Haematology: Part 1 of 2. 77

[Gracia-Pinilla 2009] MiguelAngel Gracia-Pinilla, Domingo Ferrer, Sergio Mejia-Rosales and Eduardo Perez-Tijerina. *Size-Selected Ag Nanoparticles with Five-Fold Symmetry.* Nanoscale Research Letters, vol. 4, no. 8, pages 896–902, 2009. 38

[Gremlich 2000] H.U. Gremlich and B. Yan. Infrared and raman spectroscopy of biological materials. Practical Spectroscopy. Taylor & Francis, 2000. 15, 17

[Guinier 2013] A. Guinier. X-ray diffraction: In crystals, imperfect crystals, and amorphous bodies. Dover Books on Physics. Dover Publications, 2013. 54

[Guo 2003] Q. Guo, P. Fallon, J. Yin, R.E. Palmer, N. Bampos and J.K.M. Sanders. *Growth of Densely Packed Gold Nanoparticles on Graphite Using Molecular Templates.* Advanced Materials, vol. 15, no. 13, pages 1084–1087, 2003. 40

[Guo 2004] H Guo, S.C Lee, L.Y Chan and W.M Li. *Risk assessment of exposure to volatile organic compounds in different indoor environments.* Environmental Research, vol. 94, no. 1, pages 57 – 66, 2004. 3, 78

[Guo 2011] Shaojun Guo and Erkang Wang. *Noble metal nanomaterials: Controllable synthesis and application in fuel cells and analytical sensors.* Nano Today, vol. 6, no. 3, pages 240 – 264, 2011. 43

[Hada 1976] Hiroshi Hada, Yoshiro Yonezawa, Yoshida Akio and Atsuhiro Kurakake. *Photoreduction of silver ion in aqueous and alcoholic solutions.* The Journal of Physical Chemistry, vol. 80, no. 25, pages 2728–2731, 1976. 41

[Haes 2002] Amanda J. Haes and Richard P. Van Duyne. *A Nanoscale Optical Biosensor: Sensitivity and Selectivity of an Approach Based on the Localized Surface Plasmon Resonance Spectroscopy of Triangular Silver Nanoparticles.* Journal of the American Chemical Society, vol. 124, no. 35, pages 10596–10604, 2002. PMID: 12197762. 36

[Haes 2004] Amanda J. Haes, Shengli Zou, George C. Schatz and Richard P. Van Duyne. *A Nanoscale Optical Biosensor: The Long Range Distance Dependence of the Localized Surface Plasmon Resonance of Noble Metal Nanoparticles.* The Journal of Physical Chemistry B, vol. 108, no. 1, pages 109–116, 2004. 36

[Hagena 1981] Otto F. Hagena. *Nucleation and growth of clusters in expanding nozzle flows.* Surface Science, vol. 106, no. 1-3, pages 101 − 116, 1981. 37

[Hamley 1998] I. W. Hamley. The physics of block copolymers. Oxford University Press: New York, 1998. 43

[Hamley 2003] I W Hamley. *Nanostructure fabrication using block copolymers.* Nanotechnology, vol. 14, no. 10, page R39, 2003. 43

[Harrison 2004] Christopher Harrison, John A. Dagata and Douglas H. Adamson. Lithography with self-assembled block copolymer microdomains, pages 295–323. John Wiley Sons, Ltd, 2004. 44

[Haynes 2002] Christy L. Haynes, Adam D. McFarland, Matthew T. Smith, John C. Hulteen and Richard P. Van Duyne. *Angle-Resolved Nanosphere Lithography: Manipulation of Nanoparticle Size, Shape, and Interparticle Spacing.* The Journal of Physical Chemistry B, vol. 106, no. 8, pages 1898–1902, 2002. 36

[Haynes 2003a] Christy L. Haynes and Richard P. Van Duyne. *Dichroic Optical Properties of Extended Nanostructures Fabricated Using Angle-Resolved Nanosphere Lithography.* Nano Letters, vol. 3, no. 7, pages 939–943, 2003. 36

[Haynes 2003b] Christy L. Haynes and Richard P. Van Duyne. *Plasmon-Sampled Surface-Enhanced Raman Excitation Spectroscopy.* The Journal of Physical Chemistry B, vol. 107, no. 30, pages 7426–7433, 2003. 36

[He 2001] Shengtai He, Jiannian Yao, Peng Jiang, Dongxia Shi, Haoxu Zhang, Sishen Xie, Shijin Pang and Hongjun Gao. *Formation of Silver Nanoparticles and Self-Assembled Two-Dimensional Ordered Superlattice.* Langmuir, vol. 17, no. 5, pages 1571–1575, 2001. 28

[Helfand 1975a] Eugene Helfand. *Block Copolymer Theory. III. Statistical Mechanics of the Microdomain Structure.* Macromolecules, vol. 8, no. 4, pages 552–556, 1975. 44

[Helfand 1975b] Eugene Helfand and Anne Marie Sapse. *Theory of unsymmetric polymer̂polymer interfaces.* The Journal of Chemical Physics, vol. 62, no. 4, 1975. 44

[Henry 1998] Claude R. Henry. *Surface studies of supported model catalysts.* Surface Science Reports, vol. 31, no. 7-8, pages 231 − 325, 1998. 39

[Hilger 2001] A. Hilger, M. Tenfelde and U. Kreibig. *Silver nanoparticles deposited on dielectric surfaces.* Applied Physics B, vol. 73, no. 4, pages 361–372, 2001. 37

[Horcas 2007] I. Horcas, R. Fern, J. M. G-Rodr, J. Colchero, J. G-Herrero and A. M. Baro. *WSXM: A software for scanning probe microscopy and a tool for nanotechnology.* Review of Scientific Instruments, vol. 78, no. 1, pages –, 2007. 58

[Huang 1996] H. H. Huang, X. P. Ni, G. L. Loy, C. H. Chew, K. L. Tan, F. C. Loh, J. F. Deng and G. Q. Xu. *Photochemical Formation of Silver Nanoparticles in Poly(N-vinylpyrrolidone).* Langmuir, vol. 12, no. 4, pages 909–912, 1996. 29, 41

[Hubbard 1995] A.T. Hubbard. The handbook of surface imaging and visualization. Taylor & Francis, 1995. 56

[Hubenthal 2009a] F. Hubenthal, R. Morarescu, L. Englert, L. Haag, T. Baumert and F. Träger. *Parallel generation of nanochannels in fused silica with a single femtosecond laser pulse: Exploiting the optical near fields of triangular nanoparticles.* Applied Physics Letters, vol. 95, no. 6, pages –, 2009. 34

[Hubenthal 2009b] Frank Hubenthal. *Nanoparticles and their tailoring with laser light.* European Journal of Physics, vol. 30, no. 4, page S49, 2009. 36, 39, 41

[Hubenthal 2011] F. Hubenthal. *1.13 - Noble Metal Nanoparticles: Synthesis and Optical Properties.* In David L. Andrews, Gregory D. Scholes and Gary P. Wiederrecht, editeurs, Comprehensive Nanoscience and Technology, pages 375 – 435. Academic Press, Amsterdam, 2011. 27, 34

[Hulteen 1995] John C. Hulteen and Richard P. Van Duyne. *Nanosphere lithography: A materials general fabrication process for periodic particle array surfaces.* Journal of Vacuum Science Technology A, vol. 13, no. 3, pages 1553–1558, 1995. 34

[Jarvis 2008] Roger M. Jarvis, Helen E. Johnson, Emma Olembe, Arunkumar Panneerselvam, Mohammad A. Malik, Mohammad Afzaal, Paul O'Brien and Royston Goodacre. *Towards quantitatively reproducible substrates for SERS.* Analyst, vol. 133, pages 1449–1452, 2008. 29

[Jeanmaire 1977] David L. Jeanmaire and Richard P. Van Duyne. *Surface raman spectroelectrochemistry: Part I. Heterocyclic, aromatic, and aliphatic amines adsorbed on the anodized silver electrode.* Journal of Electroanalytical Chemistry and Interfacial Electrochemistry, vol. 84, no. 1, pages 1 – 20, 1977. 17

[Jensen 2000] Traci R. Jensen, Michelle Duval Malinsky, Christy L. Haynes and Richard P. Van Duyne. *Nanosphere Lithography: Tunable Localized Surface Plasmon Resonance Spectra of Silver Nanoparticles.* The Journal of Physical Chemistry B, vol. 104, no. 45, pages 10549–10556, 2000. 29

[Kapoor 2003] Sudhir Kapoor and Tulsi Mukherjee. *Photochemical formation of copper nanoparticles in poly(N-vinylpyrrolidone).* Chemical Physics Letters, vol. 370, no. 1â2, pages 83 – 87, 2003. 41

[Kappes 1982] Manfred M. Kappes, Roland W. Kunz and Ernst Schumacher. *Production of large sodium clusters by seeded beam expansions.* Chemical Physics Letters, vol. 91, no. 6, pages 413 – 418, 1982. 37

[Keskinen 2007] H. Keskinen, J.M. Mäkelä, M. Aromaa, J. Ristimäki, T. Kanerva, E. Levänen, T. Mäntylä and J. Keskinen. *Effect of silver addition on the formation and deposition of titania nanoparticles produced by liquid flame spray.* Journal of Nanoparticle Research, vol. 9, no. 4, pages 569–588, 2007. 42

[Kimoto 1953] Kazuo Kimoto. *Study on the Intensity Anomaly of Electron Diffraction Powder Patterns from Minute Silver Crystallites.* Journal of the Physical Society of Japan, vol. 8, no. 6, pages 762–768, 1953. 37

[Kneipp 1998] Katrin Kneipp, Harald Kneipp, V. Bhaskaran Kartha, Ramasamy Manoharan, Geurt Deinum, Irving Itzkan, Ramachandra R. Dasari and Michael S. Feld. *Detection and identification of a single DNA base molecule using surface-enhanced Raman scattering (SERS).* Phys. Rev. E, vol. 57, pages R6281–R6284, Jun 1998. 2

[Kneipp 2006] K. Kneipp, M. Moskovits and H. Kneipp. Surface-enhanced raman scattering: Physics and applications. Topics in Applied Physics. Physica-Verlag, 2006. 1

[Kontio 2009] Juha M. Kontio, Hannu Husu, Janne Simonen, Mikko J. Huttunen, Juha Tommila, Markus Pessa and Martti Kauranen. *Nanoimprint fabrication of gold nanocones with 10 nm tips for enhanced optical interactions.* Opt. Lett., vol. 34, no. 13, pages 1979–1981, Jul 2009. 30

[Korppi-Tommola 1981] J. Korppi-Tommola and R. W. Yip. *Solvent effects on the visible absorption spectrum of crystal violet.* Canadian Journal of Chemistry, vol. 59, no. 2, pages 191–194, 1981. 66

[Kotov 1993] Nicholas A. Kotov, M. Elisabete Darbello Zaniquelli, Fiona C. Meldrum and Janos H. Fendler. *Two-dimensional silver electrocrystallization under monolayers spread on aqueous silver nitrate.* Langmuir, vol. 9, no. 12, pages 3710–3716, 1993. 29

[Kralchevsky 1994] P A Kralchevsky, N D Denkov, V N Paunov, O D Velev, I B Ivanov, H Yoshimura and K Nagayama. *Formation of two-dimensional colloid crystals in liquid films under the action of capillary forces.* Journal of Physics: Condensed Matter, vol. 6, no. 23A, page A395, 1994. 34

[Kratky 1984] O. Kratky and H. Stabinger. *X-ray small angle camera with block-collimation system an instrument of colloid research.* Colloid and Polymer Science, vol. 262, no. 5, pages 345–360, 1984. 58, 60

[Kratschmer 1981] E. Kratschmer. *Verification of a proximity effect correction program in electron‑beam lithography.* Journal of Vacuum Science Technology, vol. 19, no. 4, pages 1264–1268, 1981. 31

[Kreibig 1995] U. Kreibig and M. Vollmer. Optical properties of metal clusters. Numeéro v. 25 de Springer series in materials science. Springer, 1995. 21

[Krishnamoorthy 2006] S. Krishnamoorthy, R. Pugin, J. Brugger, H. Heinzelmann and C. Hinderling. *Tuning the Dimensions and Periodicities of Nanostructures Starting from the Same Polystyrene-block-poly(2-vinylpyridine) Diblock Copolymer.* Advanced Functional Materials, vol. 16, no. 11, pages 1469–1475, 2006. 61

[Kurouski 2012] Dmitry Kurouski, Tanja Deckert-Gaudig, Volker Deckert and Igor K. Lednev. *Structure and Composition of Insulin Fibril Surfaces Probed by TERS.* Journal of the American Chemical Society, vol. 134, no. 32, pages 13323–13329, 2012. 77

[Lamprecht 1999] B. Lamprecht, A. Leitner and F.R. Aussenegg. *SHG studies of plasmon dephasing in nanoparticles.* Applied Physics B, vol. 68, no. 3, pages 419–423, 1999. 30, 31

[Lee 1982] P. C. Lee and D. Meisel. *Adsorption and surface-enhanced Raman of dyes on silver and gold sols.* The Journal of Physical Chemistry, vol. 86, no. 17, pages 3391–3395, 1982. 27, 36

[Lee 2011] Wonjoo Lee, Seung Yong Lee, Robert M. Briber and Oded Rabin. *Self-Assembled SERS Substrates with Tunable Surface Plasmon Resonances.* Advanced Functional Materials, vol. 21, no. 18, pages 3424–3429, 2011. 45

[Leopold 2003] Nicolae Leopold and Bernhard Lendl. *A New Method for Fast Preparation of Highly Surface-Enhanced Raman Scattering (SERS) Active Silver Colloids at Room Temperature by Reduction of Silver Nitrate with Hydroxylamine Hydrochloride.* The Journal of Physical Chemistry B, vol. 107, no. 24, pages 5723–5727, 2003. 36

[Leyton 2004] P. Leyton, S. Sanchez-Cortes, J. V. Garcia-Ramos, C. Domingo, M. Campos-Vallette, C. Saitz and R. E. Clavijo. *Selective Molecular Recognition of Polycyclic Aromatic Hydrocarbons (PAHs) on Calix[4]arene-Functionalized Ag Nanoparticles by Surface-Enhanced Raman Scattering.* The Journal of Physical Chemistry B, vol. 108, no. 45, pages 17484–17490, 2004. 3, 78

[Li 1998] Shoutian Li and M.Samy El-Shall. *Synthesis of nanoparticles by reactive laser vaporization: silicon nanocrystals in polymers and properties of gallium and tungsten oxides.* Applied Surface Science, vol. 127â129, no. 0, pages 330 − 338, 1998. iv, 37

[Li 2003] Xiaoling Li, Junhu Zhang, Weiqing Xu, Huiying Jia, Xu Wang, Bai Yang, Bing Zhao, Bofu Li and Yukihiro Ozaki. *Mercaptoacetic Acid-Capped Silver Nanoparticles Colloid: Formation, Morphology, and SERS Activity.* Langmuir, vol. 19, no. 10, pages 4285–4290, 2003. 28

[Lippert 1975] J.L. Lippert, L.E. Gorczyca and G. Meiklejohn. *A laser Raman spectroscopic investigation of phospholipid and protein configurations in hemoglobin-free erythrocyte ghosts.* Biochimica et Biophysica Acta (BBA) - Biomembranes, vol. 382, no. 1, pages 51 − 57, 1975. 77, 78

[Lombardi 2012] John R. Lombardi and Ronald L. Birke. *The theory of surface-enhanced Raman scattering.* The Journal of Chemical Physics, vol. 136, no. 14, pages –, 2012. 23

[Lu 2006] Jennifer Lu, Danielle Chamberlin, David A Rider, Maozi Liu, Ian Manners and Thomas P Russell. *Using a ferrocenylsilane-based block copolymer as a template to produce nanotextured Ag surfaces: uniformly enhanced surface enhanced Raman scattering active substrates.* Nanotechnology, vol. 17, no. 23, page 5792, 2006. 43

[Mafuné 2000] Fumitaka Mafuné, Jun-ya Kohno, Yoshihiro Takeda, Tamotsu Kondow and Hisahiro Sawabe. *Structure and Stability of Silver Nanoparticles in Aqueous Solution Produced by Laser Ablation.* The Journal of Physical Chemistry B, vol. 104, no. 35, pages 8333–8337, 2000. 29

[Magnera 1990] Thomas F. Magnera, Donald E. David and Josef Michl. *Metastable, collision-induced and laser-induced decomposition of ArN(m= 0, 1) cluster ions in the gas phase.* J. Chem. Soc., Faraday Trans., vol. 86, pages 2427–2440, 1990. 38

[Maier 2007] S.A. Maier. Plasmonics: Fundamentals and applications: Fundamentals and applications. Springer, 2007. 21

[Maillard 2003] Mathieu Maillard, Suzanne Giorgio and Marie-Paule Pileni. *Tuning the Size of Silver Nanodisks with Similar Aspect Ratios: Synthesis and Optical Properties.* The Journal of Physical Chemistry B, vol. 107, no. 11, pages 2466–2470, 2003. 28

[Malynych 2003] Serhiy Z. Malynych and George Chumanov. *Vacuum deposition of silver island films on chemically modified surfaces.* Journal of Vacuum Science Technology A, vol. 21, no. 3, 2003. 29

[Matsushita 1997] Sachiko Matsushita, Tetsuya Miwa and Akira Fujishima. *Distribution of Components in Composite Two-Dimensional Arrays of Latex Particles and Evaluation in Terms of the Fractal Dimension.* Langmuir, vol. 13, no. 9, pages 2582–2584, 1997. 33

[Mäkelä 2004] J.M. Mäkelä, H. Keskinen, T. Forsblom and J. Keskinen. *Generation of metal and metal oxide nanoparticles by liquid flame spray process.* Journal of Materials Science, vol. 39, no. 8, pages 2783–2788, 2004. 42

[Meiners 1995] J.C. Meiners, A. Ritzi, M.H. Rafailovich, J. Sokolov, J. Mlynek and G. Krausch. *Two-dimensional micelle formation of polystyrene-poly(vinylpyridine) diblock copolymers on mice surfaces.* Applied Physics A, vol. 61, no. 5, pages 519–524, 1995. 54

[Michele Giocondo 2012] Emanuela Bruno Maria P. De Santo Luca De Stefano Emmanuelle Lacaze Sara Longobardi Michele Giocondo Said Houmadi and Paola Giardina. *Atomic Force Spectroscopies: A Toolbox for Probing the Biological Matter.* In Christopher Frewin, editeur, Atomic Force Microscopy Investigations into Biology - From Cell to Protein. InTech, 2012. iv, 55

[Micheletto 1995] R. Micheletto, H. Fukuda and M. Ohtsu. *A Simple Method for the Production of a Two-Dimensional, Ordered Array of Small Latex Particles.* Langmuir, vol. 11, no. 9, pages 3333–3336, 1995. 34

[Mikkelsen 1978] S. P. Wallach D. F. Mikkelsen R. B. Verma. *Effect of transmembrane ion gradients on Raman spectra of sealed, hemoglobin-free erythrocyte membrane vesicles.* Proceedings of the National Academy of Sciences of the United States of America, vol. 75, no. 11, pages 5478–82, 1978. 77

[Mohandas 2008] Narla Mohandas and Patrick G. Gallagher. *Red cell membrane: past, present, and future.* Blood, vol. 112, no. 10, pages 3939–3948, 2008. 3, 71

[Morarescu 2009] Rodica Morarescu, David Blázquez Sánchez, Nils Borg, Tigran A. Vartanyan, Frank Träger and Frank Hubenthal. *Shape tailoring of hexagonally ordered triangular gold nanoparticles with nanosecond-pulsed laser light.* Applied Surface Science, vol. 255, no. 24, pages 9822 − 9825, 2009. Proceedings of the Sixth International Conference onPhoto-Excited Processes and Applications(6-ICPEPA). 33, 34

[Morkved 1996] T. L. Morkved, M. Lu, A. M. Urbas, E. E. Ehrichs, H. M. Jaeger, P. Mansky and T. P. Russell. *Local Control of Microdomain Orientation in Diblock Copolymer Thin Films with Electric Fields.* Science, vol. 273, no. 5277, pages 931–933, 1996. 45

[Morrison 1971] Martin Morrison and David Richard Phillips. *Exposed protein on the intact human erythrocyte.* Biochemistry, vol. 10, no. 10, pages 1766–1771, 1971. 77

[Moskovits 1978] M. Moskovits. *Surface roughness and the enhanced intensity of Raman scattering by molecules adsorbed on metals.* The Journal of Chemical Physics, vol. 69, no. 9, 1978. 17

[Moskovits 1985] Martin Moskovits. *Surface-enhanced spectroscopy.* Rev. Mod. Phys., vol. 57, pages 783–826, Jul 1985. 19

[Nagayama 1993] Kuniaki Nagayama. *Fabrication of two-dimensional colloidal arrays.* Phase Transitions, vol. 45, no. 2-3, pages 185–203, 1993. 34

[Nanda 2009] Anima Nanda and M. Saravanan. *Biosynthesis of silver nanoparticles from Staphylococcus aureus and its antimicrobial activity against {MRSA} and {MRSE}.* Nanomedicine: Nanotechnology, Biology and Medicine, vol. 5, no. 4, pages 452 – 456, 2009. 29

[Natan 2006] Michael J. Natan. *Concluding Remarks Surface enhanced Raman scattering.* Faraday Discuss., vol. 132, pages 321–328, 2006. 29, 45

[Nilius 2001a] N Nilius, N Ernst and H.-J Freund. *On energy transfer processes at cluster‚oxide interfaces: silver on titania.* Chemical Physics Letters, vol. 349, no. 5‚6, pages 351 – 357, 2001. 39

[Nilius 2001b] N Nilius, N Ernst and H.-J Freund. *Photon emission from individual supported gold clusters: thin film versus bulk oxide.* Surface Science, vol. 478, no. 1‚2, pages L327 – L332, 2001. 40

[Otto 1992] A Otto, I Mrozek, H Grabhorn and W Akemann. *Surface-enhanced Raman scattering.* Journal of Physics: Condensed Matter, vol. 4, no. 5, page 1143, 1992. 19, 24

[Otto 2005] Andreas Otto. *The chemical (electronic) contribution to surface-enhanced Raman scattering.* Journal of Raman Spectroscopy, vol. 36, no. 6-7, pages 497–509, 2005. 24

[Ouacha 2005] H. Ouacha, C. Hendrich, F. Hubenthal and F. Träger. *Laser-assisted growth of gold nanoparticles: Shaping and optical characterization.* Applied Physics B, vol. 81, no. 5, pages 663–668, 2005. 36, 39, 40, 41

[Palomba 2008] S. Palomba, L. Novotny and R.E. Palmer. *Blue-shifted plasmon resonance of individual size-selected gold nanoparticles.* Optics Communications, vol. 281, no. 3, pages 480 – 483, 2008. 38

[Park 1997] Miri Park, Christopher Harrison, Paul M. Chaikin, Richard A. Register and Douglas H. Adamson. *Block Copolymer Lithography: Periodic Arrays of 1011 Holes in 1 Square Centimeter.* Science, vol. 276, no. 5317, pages 1401–1404, 1997. 45

[Park 2008a] S. Park, B. Kim, J.-Y. Wang and T.P. Russell. *Fabrication of Highly Ordered Silicon Oxide Dots and Stripes from Block Copolymer Thin Films.* Advanced Materials, vol. 20, no. 4, pages 681–685, 2008. 43

[Park 2008b] Soojin Park, Jia-Yu Wang, Bokyung Kim and Thomas P. Russell. *From Nanorings to Nanodots by Patterning with Block Copolymers.* Nano Letters, vol. 8, no. 6, pages 1667–1672, 2008. PMID: 18444690. 43

[Pasini 2006] M. Mortensen P. Lutz H. U. Thomas A. W. Mann M. Pasini E. M. Kirkegaard. *In-depth analysis of the membrane and cytosolic proteome of red blood cells.* Blood, vol. 108, no. 3, pages 791–801, 2006. 71

[Pedersen 2007] David B. Pedersen and Shiliang Wang. *Iodination of Gas-Phase-Generated Ag Nanoparticles: Behavior of the Two Spin Orbit Components of the AgI Exciton in Ag and AgI Core-Shell Nanoparticles.* The Journal of Physical Chemistry C, vol. 111, no. 3, pages 1261–1267, 2007. 37

[Plyuto 1999] Yuri Plyuto, Jean-Marc Berquier, Catherine Jacquiod and Christian Ricolleau. *Ag nanoparticles synthesised in template-structured mesoporous silica films on a glass substrate*. Chem. Commun., pages 1653–1654, 1999. 29

[Podstawka 2004] Edyta Podstawka, Yukihiro Ozaki and Leonard M. Proniewicz. *Part I: Surface-Enhanced Raman Spectroscopy Investigation of Amino Acids and Their Homodipeptides Adsorbed on Colloidal Silver*. Appl. Spectrosc., vol. 58, no. 5, pages 570–580, May 2004. 77

[Qian 1992] Weili Qian and Samuel Krimm. *Vibrational studies of the disulfide group in proteins. VI. General correlations of SS and CS stretch frequencies with disulfide bridge geometry*. Biopolymers, vol. 32, no. 8, pages 1025–1033, 1992. 77

[Resta 2006] V. Resta, J. Siegel, J. Bonse, J. Gonzalo, C. N. Afonso, E. Piscopiello and G. Van Tenedeloo. *Sharpening the shape distribution of gold nanoparticles by laser irradiation*. Journal of Applied Physics, vol. 100, no. 8, pages –, 2006. 40

[Rockford 1999] L. Rockford, Y. Liu, P. Mansky, T. P. Russell, M. Yoon and S. G. J. Mochrie. *Polymers on Nanoperiodic, Heterogeneous Surfaces*. Phys. Rev. Lett., vol. 82, pages 2602–2605, Mar 1999. 45

[Rojas 1993] Roberto Rojas and F. Claro. *Theory of surface enhanced Raman scattering in colloids*. The Journal of Chemical Physics, vol. 98, no. 2, 1993. 22

[Ru 2008] E.L. Ru and P. Etchegoin. Principles of surface-enhanced raman spectroscopy: and related plasmonic effects. Elsevier Science, 2008. iii, 8

[Ru 2009] Eric C. Le Ru and Pablo G. Etchegoin. *Chapter 4 - {SERS} enhancement factors and related topics*. In Eric C. Le Ru and Pablo G. Etchegoin, editeurs, Principles of Surface-Enhanced Raman Spectroscopy, pages 185 – 264. Elsevier, Amsterdam, 2009. 65

[Safonov 1998] V. P. Safonov, V. M. Shalaev, V. A. Markel, Yu. E. Danilova, N. N. Lepeshkin, W. Kim, S. G. Rautian and R. L. Armstrong. *Spectral Dependence of Selective Photomodification in Fractal Aggregates of Colloidal Particles*. Phys. Rev. Lett., vol. 80, pages 1102–1105, Feb 1998. 40

[Sánchez-Iglesias 2010] Ana Sánchez-Iglesias, Paula Aldeanueva-Potel, Weihai Ni, Jorge Pérez-Juste, Isabel Pastoriza-Santos, Ramón A. Alvarez-Puebla, Beri N. Mbenkum and Luis M. Liz-Marzán. *Chemical seeded growth of Ag nanoparticle arrays and their application as reproducible {SERS} substrates*. Nano Today, vol. 5, no. 1, pages 21 – 27, 2010. 30

[Scaiano 2006] J. C. Scaiano, Carolina Aliaga, Steven Maguire and Dashan Wang. *Magnetic Field Control of Photoinduced Silver Nanoparticle Formation*. The Journal of Physical Chemistry B, vol. 110, no. 26, pages 12856–12859, 2006. 41

[Schrötter 1979] H. W. Schrötter and A. Weber H. W. Klöckner. *Raman Spectroscopy of Gases and Liquids, Topics in Current Physics*. Electrochimica Acta, vol. II, 1979. 11, 12

[Schultz 2003] David A Schultz. *Plasmon resonant particles for biological detection*. Current Opinion in Biotechnology, vol. 14, no. 1, pages 13 – 22, 2003. 62

[Scott 2007] R.A. Scott and C.M. Lukehart. *Applications of physical methods to inorganic and bioinorganic chemistry*. EIC Books. Wiley, 2007. 56

[Seal 2003] Katyayani Seal, Mark A. Nelson, Z. Charles Ying, Dentcho A. Genov, Andrey K. Sarychev and Vladimir M. Shalaev. *Growth, morphology, and optical and electrical properties of semicontinuous metallic films*. Phys. Rev. B, vol. 67, page 035318, Jan 2003. 40

[Segalman 2005] Rachel A. Segalman. *Patterning with block copolymer thin films*. Materials Science and Engineering: R: Reports, vol. 48, no. 6, pages 191 − 226, 2005. 43, 44

[Segalman 2009] Rachel A. Segalman, Bryan McCulloch, Saar Kirmayer and Jeffrey J. Urban. *Block Copolymers for Organic Optoelectronics*. Macromolecules, vol. 42, no. 23, pages 9205–9216, 2009. 43

[Semenov 1989] A. N. Semenov. *Microphase separation in diblock-copolymer melts: ordering of micelles*. Macromolecules, vol. 22, no. 6, pages 2849–2851, 1989. 61

[She 1974] C.Y. She, N.D. Dinh and Anthony T. Tu. *Laser raman scattering of glucosamine N-acetylglucosamine, and glucuronic acid*. Biochimica et Biophysica Acta (BBA) - General Subjects, vol. 372, no. 2, pages 345 − 357, 1974. 77

[Shirtcliffe 1999] Neil Shirtcliffe, Ulrich Nickel and Siegfried Schneider. *Reproducible Preparation of Silver Sols with Small Particle Size Using Borohydride Reduction: For Use as Nuclei for Preparation of Larger Particles*. Journal of Colloid and Interface Science, vol. 211, no. 1, pages 122 − 129, 1999. 28

[Si 2009] M.Z. Si, Y.P. Kang and Z.G. Zhang. *Surface-enhanced Raman scattering (SERS) spectra of Methyl Orange in Ag colloids prepared by electrolysis method*. Applied Surface Science, vol. 255, no. 11, pages 6007 − 6010, 2009. 28

[Siebert 2008] Friedrich Siebert and Peter Hildebrandt. Introduction, pages 1–10. Wiley-VCH Verlag GmbH Co. KGaA, 2008. 1

[Smith 2005] Ewen Smith and Geoffrey Dent. Surface-enhanced raman scattering and surface-enhanced resonance raman scattering, pages 113–133. John Wiley Sons, Ltd, 2005. 23

[Sondi 2003] Ivan Sondi, Dan V Goia and Egon Matijević. *Preparation of highly concentrated stable dispersions of uniform silver nanoparticles*. Journal of Colloid and Interface Science, vol. 260, no. 1, pages 75 − 81, 2003. 28

[Spatz 1996] Joachim P. Spatz, Sergei Sheiko and Martin Möller. *Ion-Stabilized Block Copolymer Micelles: Film Formation and Intermicellar Interaction*. Macromolecules, vol. 29, no. 9, pages 3220–3226, 1996. 45

[Spatz 2002] J.P. Spatz, V.Z.-H. Chan, S. Mößmer, F.-M. Kamm, A. Plettl, P. Ziemann and M. Möller. *A Combined Top - Down/Bottom - Up Approach to the Microscopic Localization of Metallic Nanodots*. Advanced Materials, vol. 14, no. 24, pages 1827–1832, 2002. 45

[Stietz 2001] F. Stietz. *Laser manipulation of the size and shape of supported nanoparticles*. Applied Physics A, vol. 72, no. 4, pages 381–394, 2001. 40

[Sujith 2009] Athiyanathil Sujith, Tamitake Itoh, Hiroko Abe, Ken-ichi Yoshida, Manikan-tanS. Kiran, Vasudevanpillai Biju and Misturu Ishikawa. *Imaging the cell wall of living single yeast cells using surface-enhanced Raman spectroscopy*. Analytical and Bioanalytical Chemistry, vol. 394, no. 7, pages 1803–1809, 2009. 2

[Sun 2005] F. Sun, W. Cai, Y. Li, G. Duan, W.T. Nichols, C. Liang, N. Koshizaki, Q. Fang and I.W. Boyd. *Laser morphological manipulation of gold nanoparticles periodically arranged on solid supports*. Applied Physics B, vol. 81, no. 6, pages 765–768, 2005. 36

[Svergun 2013] D.I. Svergun, M.H.J. Koch, P.A. Timmins and R.P. May. Small angle x-ray and neutron scattering from solutions of biological macromolecules. International Union of Crystallography Texts on Crystallography. OUP Oxford, 2013. 54

[Tan 2005] B. J. Y. Tan, C. H. Sow, T. S. Koh, K. C. Chin, A. T. S. Wee and C. K. Ong. *Fabrication of Size-Tunable Gold Nanoparticles Array with Nanosphere Lithography, Reactive Ion Etching, and Thermal Annealing*. The Journal of Physical Chemistry B, vol. 109, no. 22, pages 11100–11109, 2005. 36

[Tan 2013] Taixing Tan, Chungui Tian, Zhiyu Ren, Jun Yang, Yajie Chen, Li Sun, Zhong-tao Li, Aiping Wu, Jie Yin and Honggang Fu. *LSPR-dependent SERS performance of silver nanoplates with highly stable and broad tunable LSPRs prepared through an improved seed-mediated strategy*. Phys. Chem. Chem. Phys., vol. 15, pages 21034–21042, 2013. 63

[Tantra 2007] Ratna Tantra, Richard J. C. Brown and Martin J. T. Milton. *Strategy to improve the reproducibility of colloidal SERS*. Journal of Raman Spectroscopy, vol. 38, no. 11, pages 1469–1479, 2007. 29

[Tao 2008] Andrea R. Tao, Susan Habas and Peidong Yang. *Shape Control of Colloidal Metal Nanocrystals*. Small, vol. 4, no. 3, pages 310–325, 2008. 28, 29

[Tseng 2005] Ampere A. Tseng. *Recent Developments in Nanofabrication Using Focused Ion Beams*. Small, vol. 1, no. 10, pages 924–939, 2005. 45

[Turkevich 1951] John Turkevich, Peter Cooper Stevenson and James Hillier. *A study of the nucleation and growth processes in the synthesis of colloidal gold*. Discuss. Faraday Soc., vol. 11, pages 55–75, 1951. 28, 36

[Valeur 2012] Bernard Valeur and Mario Nuno Berberan-Santos. Absorption of ultraviolet, visible, and near-infrared radiation, pages 31–51. Wiley-VCH Verlag GmbH Co. KGaA, 2012. 57

[Van Wart 1986] H E Van Wart and H A Scheraga. *Agreement with the disulfide stretching frequency-conformation correlation of Sugeta, Go, and Miyazawa*. Proceedings of the National Academy of Sciences, vol. 83, no. 10, pages 3064–3067, 1986. 77

[Vartanyan 2001] T. Vartanyan, J. Bosbach, F. Stietz and F. Trager. *Theory of spectral hole burning for the study of ultrafast electron dynamics in metal nanoparticles*. Applied Physics B, vol. 73, no. 4, pages 391–399, 2001. 22

[Velev 2000] Orlin D. Velev and Abraham M. Lenhoff. *Colloidal crystals as templates for porous materials*. Current Opinion in Colloid Interface Science, vol. 5, no. 1â2, pages 56 − 63, 2000. 34

[Velikov 2003] Krassimir P. Velikov, Gabby E. Zegers and Alfons van Blaaderen. *Synthesis and Characterization of Large Colloidal Silver Particles*. Langmuir, vol. 19, no. 4, pages 1384–1389, 2003. 28

[Vlčková 1997] Blanka Vlčková, Kateřina Solecká-Čermáková, Pavel Matejka and Vladimír Baumruk. *{SERS} spectroscopy with Ag colloids*. Journal of Molecular Structure, vol. 408 - 409, no. 0, pages 149 − 154, 1997. Molecular Spectroscopy and Molecular Structure 1996. 28

[Wallach 1975] Donald F.H. Wallach and Surendra P. Verma. *Raman and resonance-Raman scattering by erythrocyte ghosts*. Biochimica et Biophysica Acta (BBA) - Biomembranes, vol. 382, no. 4, pages 542 − 551, 1975. 78

[Wang 2002] Tom C. Wang, Michael F. Rubner and Robert E. Cohen. *Polyelectrolyte Multilayer Nanoreactors for Preparing Silver Nanoparticle Composites: Controlling Metal Concentration and Nanoparticle Size*. Langmuir, vol. 18, no. 8, pages 3370–3375, 2002. 29

[Wang 2004] Xu Dong Wang, Elton Graugnard, Jeffrey S. King, Zhong Lin Wang and Christopher J. Summers. *Large-Scale Fabrication of Ordered Nanobowl Arrays*. Nano Letters, vol. 4, no. 11, pages 2223–2226, 2004. 34

[Wang 2009] Yong Wang, Michael Becker, Li Wang, Jinquan Liu, Roland Scholz, Juan Peng, Ulrich GoÌsele, Silke Christiansen, Dong Ha Kim and Martin Steinhart. *Nanostructured Gold Films for SERS by Block Copolymer-Templated Galvanic Displacement Reactions*. Nano Letters, vol. 9, no. 6, pages 2384–2389, 2009. PMID: 19459615. 43

[Wenzel 1999] T. Wenzel, J. Bosbach, F. Stietz and F. Träger. *In situ determination of the shape of supported silver clusters during growth*. Surface Science, vol. 432, no. 3, pages 257 − 264, 1999. 39

[Xie 2011] Wei Xie, Penghe Qiu and Chuanbin Mao. *Bio-imaging, detection and analysis by using nanostructures as SERS substrates*. J. Mater. Chem., vol. 21, pages 5190–5202, 2011. 2

[Xu 2013] Ping Xu, Kuan Chang, Young Il Park, Bin Zhang, Leilei Kang, Yunchen Du, Rashi S. Iyer and Hsing-Lin Wang. *Conjugated polymer mediated synthesis of nanoparticle clusters and core/shell nanoparticles*. Polymer, vol. 54, no. 2, pages 485 − 489, 2013. 29

[Yaffe 2008] Nicola R. Yaffe and Ewan W. Blanch. *Effects and anomalies that can occur in {SERS} spectra of biological molecules when using a wide range of aggregating agents for hydroxylamine-reduced and citrate-reduced silver colloids*. Vibrational Spectroscopy, vol. 48, no. 2, pages 196 − 201, 2008. A Collection of Papers Presented at the 4th International Conference on Advanced Vibrational Spectroscopy (ICAVS-4) Corfu, Greece, 10-15 June 2007 - Part II. 28

[Yan 2011] Bo Yan, Svetlana V. Boriskina and Björn M. Reinhard. *Design and Implementation of Noble Metal Nanoparticle Cluster Arrays for Plasmon Enhanced Biosensing*. The Journal of Physical Chemistry C, vol. 115, no. 50, pages 24437–24453, 2011. 43

[Young 2014] Wen-Shiue Young, Wei-Fan Kuan and Thomas H. Epps. *Block copolymer electrolytes for rechargeable lithium batteries*. Journal of Polymer Science Part B: Polymer Physics, vol. 52, no. 1, pages 1–16, 2014. 43

[Zeng 2012] Haibo Zeng, Xi-Wen Du, Subhash C. Singh, Sergei A. Kulinich, Shikuan Yang, Jianping He and Weiping Cai. *Nanomaterials via Laser Ablation/Irradiation in Liquid: A Review.* Advanced Functional Materials, vol. 22, no. 7, pages 1333–1353, 2012. 42

[Zhang 2006] J. Zhang, Y. Gao, R.A. Alvarez-Puebla, J.M. Buriak and H. Fenniri. *Synthesis and SERS Properties of Nanocrystalline Gold Octahedra Generated from Thermal Decomposition of HAuCl4 in Block Copolymers.* Advanced Materials, vol. 18, no. 24, pages 3233–3237, 2006. 43

[Zhang 2014] Chunling Zhang, Kaijun Wang, Dejun Han and Qing Pang. *Surface enhanced Raman scattering (SERS) spectra of trinitrotoluene in silver colloids prepared by microwave heating method.* Spectrochimica Acta Part A: Molecular and Biomolecular Spectroscopy, vol. 122, no. 0, pages 387 − 391, 2014. 29

[Zhao 2002] Y.-P. Zhao, D.-X. Ye, G.-C. Wang and T.-M. Lu. *Novel Nano-Column and Nano-Flower Arrays by Glancing Angle Deposition.* Nano Letters, vol. 2, no. 4, pages 351–354, 2002. 29

[Zhu 2000] Junjie Zhu, Suwen Liu, O. Palchik, Yuri Koltypin and A. Gedanken. *Shape-Controlled Synthesis of Silver Nanoparticles by Pulse Sonoelectrochemical Methods.* Langmuir, vol. 16, no. 16, pages 6396–6399, 2000. 29